A STUDY OF THE COMPOSITION OF ULTRA HIGH ENERGY COSMIC RAYS USING THE HIGH RESOLUTION FLY'S EYE

by

Gregory C. Archbold

A dissertation submitted to the faculty of
The University of Utah
in partial fulfillment of the requirements for the degree of

Doctor of Philosophy

Department of Physics

The University of Utah

August 2002

THE UNIVERSITY OF UTAH GRADUATE SCHOOL

SUPERVISORY COMMITTEE APPROVAL

of a dissertation submitted by

Gregory C. Archbold

This dissertation has been read by each member of the following supervisory committee and by majority vote has been found to be satisfactory.

	Chair: Pierre V. Sokolsky
	Gene Loh
	Carleton DeTar
	Clayton Williams
	Steve Kreuger

THE UNIVERSITY OF UTAH GRADUATE SCHOOL

FINAL READING APPROVAL

To the Graduate Council of The University of Utah:

I have read the dissertation of Gregory C. Archbold in its final form and have found that (1) its format, citations, and bibliographic style are consistent and acceptable; (2) its illustrative materials including figures, tables, and charts are in place; and (3) the final manuscript is satisfactory to the Supervisory Committee and is ready for submission to The Graduate School.

Date

Pierre V. Sokolsky
Chair, Supervisory Committee

Approved for the Major Department

Valy Vardeny
Chair

Approved for the Graduate Council

David S. Chapman
Dean of The Graduate School

ABSTRACT

The composition of Ultra High Energy Cosmic Rays (UHECR) was studied with the High Resolution Fly's Eye cosmic ray observatory (HiRes). HiRes is an air fluorescence detector comprised of two sites separated by 12.6 km on the U.S. Army's Dugway Proving Ground in the West Desert of Utah. Utilizing the atmosphere as a calorimeter, the longitudinal development of Extensive Air Showers (EAS) is measured and the energies, composition, flux, and anisotropy in arrival direction of the highest energy particles are determined.

The QGSJet01 and SIBYLL 2.1 hadronic interaction models were used in versions 6.005 and 6.010 of the CORSIKA event generator to determine which measurable EAS parameters were correlated with UHECR compositon and to study predicted elongation rates and X_{max} distribution widths in the UHECR regime. The CORSIKA-generated EAS were incorporated directly into a detailed atmospheric and detector Monte Carlo.

Data were collected in stereo between November 1999 and September 2001. The data were reconstructed using measurements of the atmosphere, well-determined geometry, a global profile fit, and a detailed Monte Carlo.

Monte Carlo resolution is 30 gm/cm^2 in X_{max} and 13% in Energy. The Elongation Rate between $10^{17.7}$ eV and 10^{20} eV is 55.2 $\pm$ 5.0 (stat) $\pm$ 3.6 (sys). X_{max} distribution widths are consistent with a slowly changing and predominantly light composition. A simple composition model containing only protons and iron nuclei was compared to QGSJet and SIBYLL. The best agreement between the model and the data is at 77% protons for QGSJet and 57% protons for SIBYLL.

For Dad

CONTENTS

LIST OF FIGURES

LIST OF TABLES

ACKNOWLEDGEMENTS

I wish to thank my advisor, Professor Pierre Sokolsky, for his guidance. He never did all the thinking for me, but he also never let me spin my wheels longer than needed for the lesson to be learned. I also thank Professor Gene Loh, who introduced me to the study of cosmic rays, the many others of the Fly's Eye group who laid decades of groundwork, and all the HiRes collaborators for their innumerable contributions to the experiment.

Special thanks go to Bruce Dawson, who first showed me HiRes, Ken Simpson, whose work helped guide mine, and Mike Roberts, who was never too busy to explain the physics.

I thank the Center for High Performance Computing, the US Army's Dugway Proving Ground, and the National Science Foundation for their support.

Kevin Reil has my deepest gratitude. His data analysis set the foundation for this work, his help with coding gave me the tools to undertake this work, and his friendship gave me the sanity to complete this work. *"Hey, Kevin, how do you . . . ?"*

Most especially I wish to thank my wife, Monique, and my children, Liesl, Rhiannon, Ralph, and Hans. Monique made immeasurable sacrifices in the name of my enjoying my job while the children made sacrifices they did not understand. I love you each dearly. I hope that in the years ahead you will reap the rewards of your sacrifices and you will come to appreciate that my motives were not completely selfish.

CHAPTER 1

COSMIC RAYS

1.1 A Brief History of Cosmic Ray Research

Before the advent of particle accelerators, the great discoveries of particle physics were made by observing cosmic radiation. Initially, the source of the radiation which was causing electroscopes to discharge was unknown. Suspecting that radiation from space was interacting with the charge on the electroscopes, Wilson tried taking an instrument into a railway tunnel expecting a decrease in the rate of discharge [1]. Unfortunately, naturally occurring radioactive elements in the earth led to an unmeasurable change in the discharge rate.

In 1910, Wulf took the next step by taking an electroscope up the Eiffel Tower. Had all of the radiation causing discharge been due to the earth's radioactivity, the discharge rate should have dropped much more than it did. The experiment suggested that there was in fact a cosmic source producing some of the ions in the atmosphere [2].

Then in 1912, Hess took an electroscope to an altitude of 5 km in a balloon [3]. At low altitudes—above the naturally occurring radioactive isotopes but beneath the bulk of the atmosphere—the discharge rate dropped. But as the balloon climbed to regions of less atmospheric overburden, the rate of discharge went up, confirming that the source of the radiation was extra-terrestrial. Hess' measurements were extended by Kolhorster [4], and in 1927 Clay showed that the particles, named

"cosmic rays" by Millikan in 1925 [2], were mostly positively charged particles by measuring an east-west anisotropy [5].

For the next four decades, balloon-borne cloud chamber and emulsion experiments brought the discovery of the positron (and with it confirmation of Dirac's prediction of the electron's antiparticle), muons, kaons, pions, lambda particles, omega particles, and sigma particles [2].

Perhaps equally importantly, Auger observed Extensive Air Showers (EAS)—cascades of copious numbers of particles initiated by single incident cosmic rays—in 1939. Auger et al. conducted systematic studies with separated Geiger-Muller counters [6, 7]. Coincidences significantly above the accidental rate were observed with the counters separated by as much as 300 m. Auger and his colleagues determined that they were seeing 10^6 particles, which they deduced were secondary and higher-order products of a single cosmic ray interaction at the top of the atmosphere. Seeing so many particles at ground level meant that the primary particles had energies on the order of PeV. Early in the 1950s, particle accelerators, with their controlled energy and geometry and their known interacting particles, shifted attention from the cosmic radiation, but it would be scores of years before the accelerators could reach PeV energies.

In 1967, a team led by Greisen at Cornell pioneered a new idea to exploit the EAS observed by Auger [8]. Realizing that the million-plus particles in the EAS would excite nitrogen molecules as they cascaded through the atmosphere, the Cornell team built a detector designed to observe the ultra-violet light emitted isotropically by the subsequent de-excitations. The air fluorescence technique was born (see Section 2.2.1), and was soon rewarded with successful observations by the University of Tokyo at the Dodaira Observatory in Japan [9].

Air fluorescence detectors typically have several photo-multiplier tubes (PMTs), each looking at a small segment of the sky. The signals are then combined to

give a composite view of the entire aperture, much like a compound eye. Such an arrangement has come to be known as a Fly's Eye detector. The Cornell experiment was not very successful. Air fluorescence detectors only achieve satisfactory signal-to-noise ratio on clear, moonless nights. Even under the best Ithaca skies, poor viewing conditions doomed the first generation of the Fly's Eye.

Another way to measure EAS is with an array of particle detectors on the ground. Instead of employing Geiger-Muller detectors as did Auger, modern ground arrays are typically combinations of scintillation and Čerenkov detectors. One such detector was built by Linsley [10] at Volcano Ranch in New Mexico, a remote area of the Western United States with little background light and many days a year with a dry, clear atmosphere. The University of Utah built an improved Air Fluorescence detector overlooking the existing Volcano Ranch ground array in 1976 [11]. They were able to clearly observe the ultra-violet fluorescence of EAS in coincidence with detections by the ground array.

The successful air fluorescence detector at Volcano Ranch was followed in 1981 by the University of Utah's Fly's Eye observatory at the U. S. Army's Dugway Proving Ground in the West Desert of Utah [12]. Each of the 67 spherical mirrors at the original site, known as Fly's Eye I, focused light onto 12 or 14 PMTs. With each PMT viewing a $5^\circ \times 5^\circ$ segment of the sky, Fly's Eye I provided 2π steradian coverage. In 1986, the 36-mirrors comprising Fly's Eye II came online 3.4 km away. Viewing only the half of the sky in the direction of Fly's Eye I, Fly's Eye II gave the Fly's Eye observatory stereo capability [13]. The observatory collected data until 1992, and in 1991 detected one of only two particles yet observed with an energy above 3 x 10^{20} eV [14, 15].

From 1993 to 1996, the High Resolution Fly's Eye Prototype was operated in conjunction with the Michigan Muon Array (MIA) at Dugway, Utah [16]. Hybrid measurements of cosmic rays were made with a high-resolution air fluorescence

detector at the Fly's Eye I site overlooking a ground array at the Fly's Eye II site (see Section 1.3.2).

The current High Resolution Fly's Eye Cosmic Ray Observatory (HiRes) will be described in detail in Chapter 3.

1.2 Models of Origin and Propagation

Amazingly, the spectrum of cosmic rays is quite smooth over twelve decades in energy (see Figure 1.1). The flux falls off as $E^{-\gamma}$ with $\gamma = 2.7$ from energies of a few x 10^9 eV to a few x 10^{20} eV. A couple of questions immediately arise:

1) What source or combination of sources can produce an $E^{-\gamma}$ spectrum over 12 decades?

2) What source can produce particles with nearly a Joule of energy?

3) How can such particles reach us?

1.2.1 Origin

The most straightforward mechanism for accelerating a charged particle is to place it in an electromagnetic field. The interaction of the particle with the magnetic field will confine the particle allowing the interaction with the electric field to boost the particle's energy. The gyroradius of the particle is dependent on its charge and energy, so at some point the particle will have enough energy to escape the acceleration region.

For electromagnetic acceleration in the vicinity of shocks, the maximum energy obtainable E_{max} is estimated by [17]

$$E_{max} = \beta \times Ze \times B \times L \tag{1.1}$$

where β is the velocity of the magnetic shock region and L is the size of the region. The close relationship among the spectrum, composition, and arrival direction

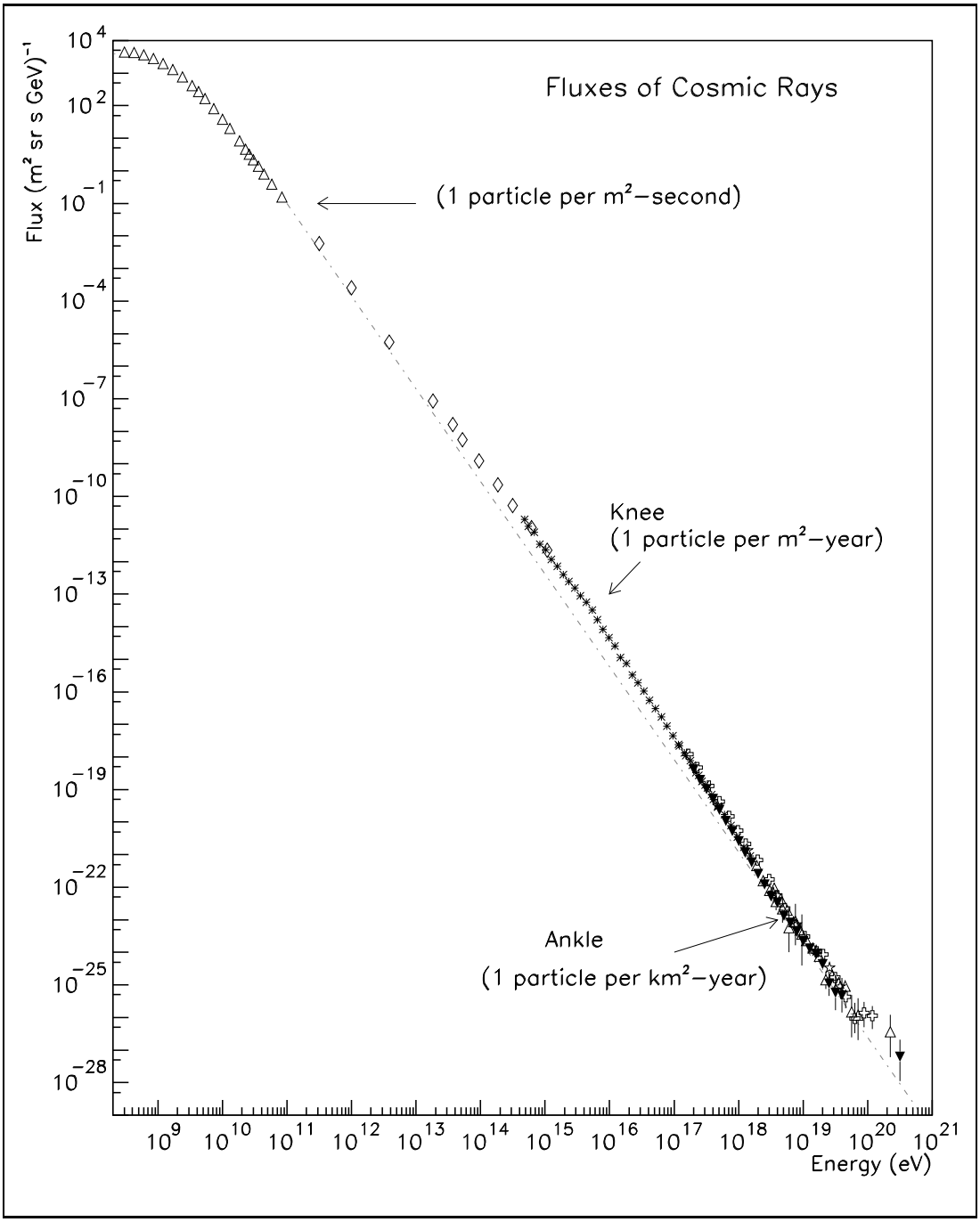

Figure 1.1. Cosmic ray spectrum. Adapted from [17].

begins to become clear. In this scheme, particles with more charge or in regions of more energetic shocks will reach higher energies. Observations of composition as a function of energy will speak to the validity of this model. The question must also be asked if the model can produce the $E^{-\gamma}$ spectrum, which it has difficulty doing [18].

The shock acceleration model has another problem, though. Figure 1.2 is known

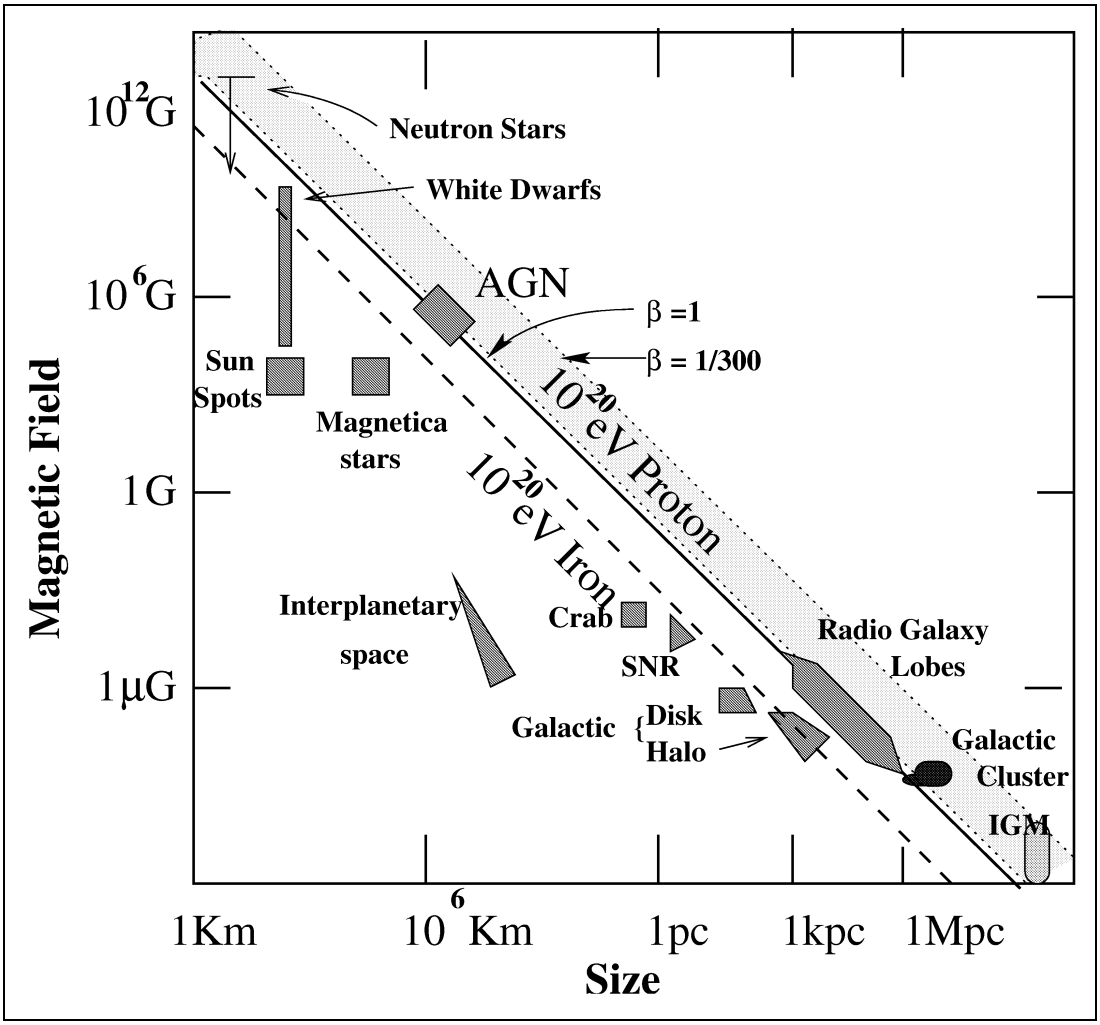

Figure 1.2. Hillas diagram. Sources below and to the left of the line are not capable of accelerating particles to the UHECR regime. The top of the shaded region represents $\beta = 1/300$. Adapted from [18].

as the Hillas diagram. Various astrophysical sources are plotted on axes of magnetic field vs. size. Only sources above the solid (dotted) line have the field strength and size to accelerate a proton (iron nucleus) to 10^{20} eV. Few candidates exist, and even in these regions it is expected that cosmic ray energy will be degraded by photopion production on the intense nearby radiation and by synchrotron losses in the associated magnetic fields [18].

Fermi suggested a statistical acceleration process where charged particles scatter off magnetized clouds in the interstellar medium [19]. Depending on the angle of entry into the cloud, the particle will gain or lose energy. Because several interactions via this mechanism result in a net gain in energy proportional to β^2 (for β = v/c, and v = typical cloud velocity), it is known as second order Fermi acceleration. Although second order Fermi acceleration gives a power-law spectrum, nothing in the theory predicts the correct spectral index. Additionally the random velocities of interstellar magnetic clouds have only $\beta^2 \approx 10^{-4}$. So with a mean free path of 1 pc, a cosmic ray will collide only about once a year, with the acceleration process competing with energy loss processes the entire time. The resulting energy gain from second order Fermi acceleration will be very slow and does not give much promise of explaining the highest energy cosmic rays [20].

Acceleration first order in β is possible when the particles are accelerated by astrophysical shocks (here v = the speed of the shock front). In first oder Fermi acceleration, the particle gains energy every time it crosses the shock front, regardless of direction (see [20, 21, 22] for a more complete discussion). For a supernova shock persisting 1000 yr, a particle with charge Ze would be accelerated to an energy of 10^4 eV $\times$ Ze. Particles in longer-lasting or stronger shock regions are still limited by Eq. (1.1) in the energy they can reach, for the particles will escape the acceleration region. Referring again to Figure 1.2, only radio galaxy lobes and active galactic

nuclei are promising potential source regions for cosmic rays with energies above 10^{20} eV [17].

It has been suggested that the highest energy cosmic rays are not accelerated to ultra-high energies (UHE), but rather created at UHE by the decay of topological defects, releasing supermassive "X" particles. Such schemes are called top down models. In grand unified theories, the symmetry breaking scale is $\approx 10^{25}$ eV. X particles of this mass decay to leptons and quarks, and the quarks then hadronize to mostly pions and some nucleons [23]. The nucleons could thus be born at UHE.

The topological defects could themselves be monopoles, which are easily accelerated by the galactic magnetic field, interacting with the atmosphere to initiate EAS and observed as UHECR. Unfortunately, the galactic magnetic field would produce a strong arrival direction anisotropy (which is not observed, see Section 1.3.3), and our best description of magnetic monopoles does not expect them to deposit enough energy to initiate EAS [24].

A third top down scheme involves neutrinos. In the first second of the universe, relic neutrinos decoupled from the thermal photon bath. As baryons clustered to form galaxies, the relic neutrinos were cooled by cosmic expansion to the point that they became gravitationally trapped as part of the hot dark matter halo. The interaction of UHE protons with the Cosmic Microwave Brackground Radiation (CMBR) produces pions and neutrons.[1] UHE neutrinos from neutron and pion decay could interact with the relic neutrino background by resonant Z production ($\nu\nu_{background} \longrightarrow Z^* \longrightarrow$ hadrons) [25]. Once again the interdependence of the spectrum and composition measurements is evident. This model cannot produce any nucleus heavier than a proton, so a heavy component in the composition at the highest energies introduces tight limits [26].

[1] This interaction will be discussed more completely in Section 1.2.2.

Although the most energetic cosmic rays could be monopoles or the products of X particle decay or the result of relic neutrino interactions, such a framework fails to explain the lower energy portion of the cosmic ray spectrum without other sources. Even with these problems, top down models are attractive because the highest energy cosmic rays can originate cosmologically locally and evade the GZK Cutoff, which will be discussed next.

1.2.2 Propagation and the GZK Cutoff

Immediately after the discovery of the CMBR by Penzias and Wilson [27], Greisen [28] and Zatsepin and Kuz'min [29] realized that protons above about 6 x10^{19} eV would have enough energy for photopion production on the CMBR photons by

$$p + \gamma_{CMBR} \longrightarrow \Delta^{+\star} \longrightarrow p + \pi^{\circ} \quad or \quad \longrightarrow n + \pi^{+} \tag{1.2}$$

With the CMBR pervasive and nearly homogenous [30], no proton above the GZK threshold can travel more than $\approx$ 50 Mpc. Heavier nuclei at the GZK energy will have a Lorentz factor lower than that of a proton at the same energy, so the heavier nucleus must be at a higher energy to interact on the CMBR analogous to Eq. (1.2). However, these heavier nuclei are susceptible to photo-disintegration through interactions with ambient radiation. The interaction lengths for photo-disintegration are also of order 10 Mpc [20]. The short radiation lengths associated with these loss mechanisms suggest that the highest energy cosmic rays observed on the earth are produced in a cosmologically nearby volume.

Additionally, the rms deflection of an $E_{20} \times 10^{20}$ eV proton traveling distance D_{Mpc} through randomly oriented patches of magnetic field with rms value B_{nG} and a characteristic length λ is [31]:

$$\delta\theta = 0.5^{\circ}\sqrt{D_{Mpc}\lambda_{Mpc}}(B_{nG}/E_{20}) \tag{1.3}$$

That is to say, deflections are expected to be on the order of a few degrees or less for extra-galactic magnetic field strengths order nG, which is consistent with measurements of the Faraday rotation of the polarization of photons from distant quasars and with measurements of synchrotron radiation. It follows that if the arrival direction of the most energetic cosmic rays is determined, it should point back to within a few degrees of the source. Referring again to Figure 1.2, recall that the choice of sources is limited. Additionally, the source must be nearby. The great GZK dilemma is that there are no known cosmologically nearby potential sources for the most energetic cosmic rays. Any model for the origin of cosmic rays must simultaneously explain the spectrum, the composition, and the anisotropy.

1.3 Current Understanding of Ultra High Energy Cosmic Rays (UHECR)

Cosmic ray observatories measure the energy and arrival direction of each incident particle, as well as other parameters which indicate the particle's chemical composition. From these measurements, the energy spectrum, trends in composition, and arrival direction anisotropies can be determined. As was illustrated in the discussion of models of the origin and propagation of cosmic rays, the three are tied quite tightly together. This work will primarily discuss the UHE regime, defined as $\geq 10^{17.7}$ eV, with some discussion of the full range of energies.

1.3.1 The Cosmic Ray Spectrum

Section 1.2 introduced Figure 1.1, the spectrum of cosmic rays. The salient characteristic of the UHECR spectrum is that it extends beyond 10^{20} eV. Not only is it amazing that particles can reach such energies, but also it is not expected that nuclei of such energies can survive the traversal of cosmologically vast distances (see Section 1.2).

Figure 1.1 shows a feature between 10^{15} and 10^{16} eV. This point where the spectral index γ changes from ≈ 2.7 to ≈ 3.0 is known as the "knee." One possible explanation for the knee is that this is the energy at which the dominant acceleration mechanism changes [33]. However, for the spectrum to remain smooth at the transition point, the lower energy source must "turn off" right when the higher energy source "turns on," and with a matched intensity [34]. Another interpretation of the data is that this is the energy above which the galactic magnetic field can no longer contain the charged particles [35]. This explanation is often called the "leaky box" model. In this construct, the cosmic rays with energies below the kneee diffuse freely through the bulk of the galaxy but are reflected by magnetic field lines at the boundaries of the galactic halo. Particles leak out because there is a non-zero probability that a cosmic ray will escape instead of being reflected at the boundary [20]. Fewer particles with energies above the knee are confined because fewer have Larmor radii smaller than the galactic disk, causing a steepening of the spectrum.

1.3.2 Composition

Clay showed that most cosmic rays are positively charged particles [5], but which charged particles? At low energies where the flux is high (see Fig. 1.1), the composition can be measured directly with balloon- or satellite-borne detectors such as JACEE [36] or RUNJOB [37, 38]. Many excellent discussions of the low energy cosmic ray composition exist (see, for example, [2]).

In the UHECR regime however, directly observing primary particles with fluxes of particles per km^2 per century would require a prohibitively large detector. Instead, EAS must be observed and the composition inferred from the air shower properties. Because the composition of UHECR is the subject of this thesis, a more complete discussion of EAS physics and composition measurements of UHECR will

be presented in Chapter 2. Here some recent UHECR composition measurements will be presented.

The Fly's Eye experiment measured the composition from 10^{17} to a little above 10^{19} eV [39]. The results are shown in Figure 1.3, which is an elongation rate plot (see Section 2.1.3). The open squares show the expected values for a purely protonic composition with a QCD pomeron hadronic model; the open circles for

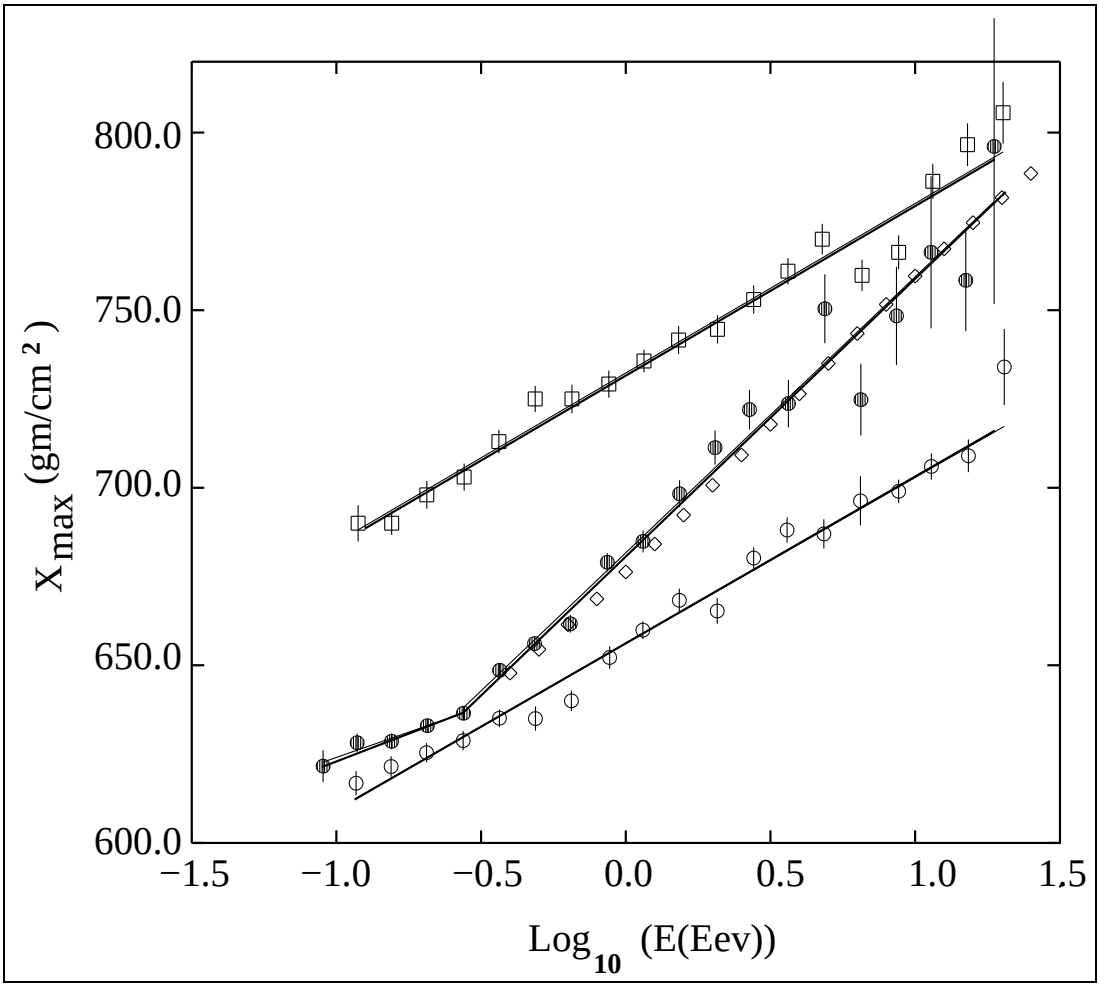

Figure 1.3. Fly's Eye composition result. The solid circles are the data. The diamonds show a simple, two component model changing from heavy to light. The upper and lower lines show the predictions for purely protonic and purely ferric compositions, respectively. Adapted from [39].

purely ferric. The solid dots are the data, and the diamonds (with line) show a simple two-component model wherein the composition is mostly iron at 10^{17} eV changing to mostly protons at 10^{19} eV. Although the two-component model was merely illustrative, the conclusion clearly supports a composition tending toward purely protonic at higher energies.

The High Resolution Fly's Eye Prototype detector, in conjunction with the MIA experiment, made a hybrid measurement of the cosmic ray spectrum and composition between 10^{17} and $10^{18.3}$ eV [40, 41]. The air fluorescence results were consistent with those of the original Fly's Eye, showing a lightening composition with increasing energy (see Figure 1.4). The ground array result, which used the $\rho_\mu(600)$ method (described in Section 2.1.4), was inconclusive (see Figure 1.5).

Another ground array measurement was made by the Akeno Giant Air Shower Array (AGASA). AGASA reported an unchanging composition between $10^{16.5}$ and 10^{19} eV [42], which contradicted the Fly's Eye result. But when the AGASA data was reanalyzed with the same hadronic interaction model used in the Fly's Eye analysis, the results of the two experiments were found to be consistent [43].

This work will extend the composition measurement to 10^{20} eV (see Chapter 6).

1.3.3 Anisotropy

At relatively low energies ($< 10^{17}$ eV), charged particles interact with the galactic magnetic field enough to wash out all directional information. Studies at these energies have shown no anisotropy. In the energy range of 10^{18} to $10^{18.3}$ eV, the AGASA group reported a 4.5σ excess about 10° from the galactic center [44]. They also measured a 3.9σ excess in the direction of the Cygnus region. Fly's Eye also saw a small enhancement in the direction galactic plane for the energy range of $10^{17.6}$ to 10^{18} eV [45],

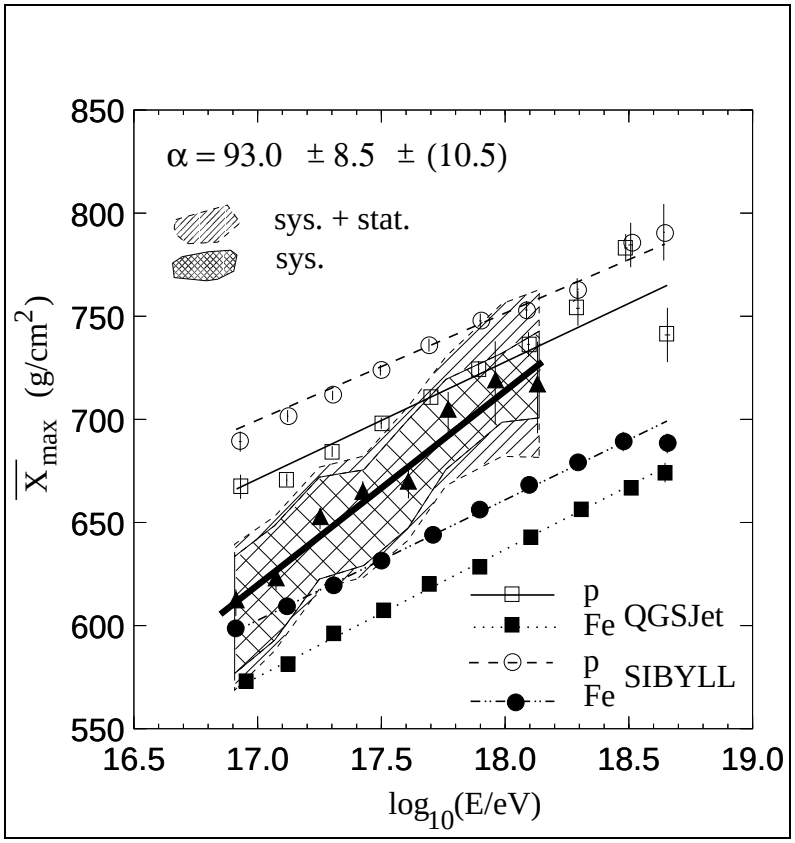

Figure 1.4. HiRes Prototype air fluorescence composition result. The triangles show the data, and the circles and squares show the expectation for purely heavy or light composition with two different hadronic interaction models. Adapted from [40].

The above results barely enter the UHECR regime, where the arrival direction of the cosmic ray does contain information about the point of origin (see Section 1.2.2). More recently, AGASA has reported evidence for clustering of the highest energy events [46], but no other group has reported corroborating evidence.

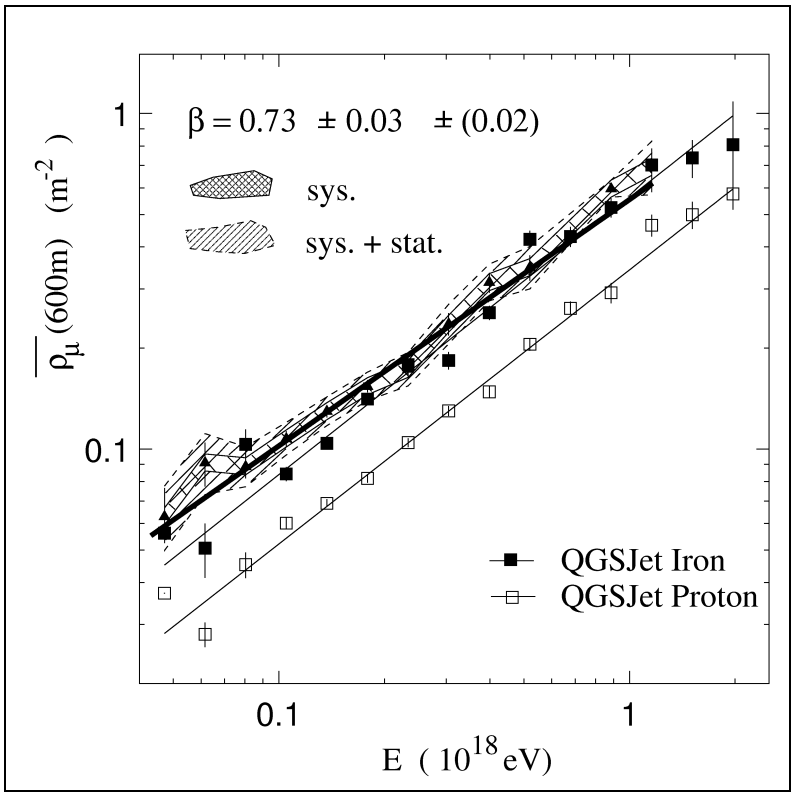

Figure 1.5. HiRes Prototype ground array composition result. The triangles show the data and the squares show the expectation from the QGSJet hadronic interaction model. Adapted from [40].

CHAPTER 2

EXTENSIVE AIR SHOWERS (EAS)

2.1 EAS Development

The most accurate way to determine the chemical composition of a cosmic ray is to trap the primary particle in a detector with an electromagnetic field. The charge, mass, and energy of the primary can then be measured directly. Such a detector must, of course, be balloon- or satellite-borne so the cosmic ray interacts with the detector before it interacts with the atmosphere. Referring to Figure 1.1, however, reminds us that the UHECR arrive at a rate of about 1 particle per square kilometer per century; a detector which hoped to actually trap a statistically significant number of UHECR would be too large for deployment on a satellite or balloon.

The study of UHECR, then, depends on the exploitation of EAS. This chapter describes EAS physics and detection as well as how the energy, composition, and anisotropy measurements are extracted from the EAS observables.

2.1.1 Shower Components

An EAS is initiated when the primary cosmic ray interacts with the atmosphere. The shower has three components: electromagnetic, hadronic, and muonic [47, 48]. Figure 2.1 illustrates the three portions of the shower [34]. The electromagnetic part of the shower is continually fed by photons from decay of neutral pions and

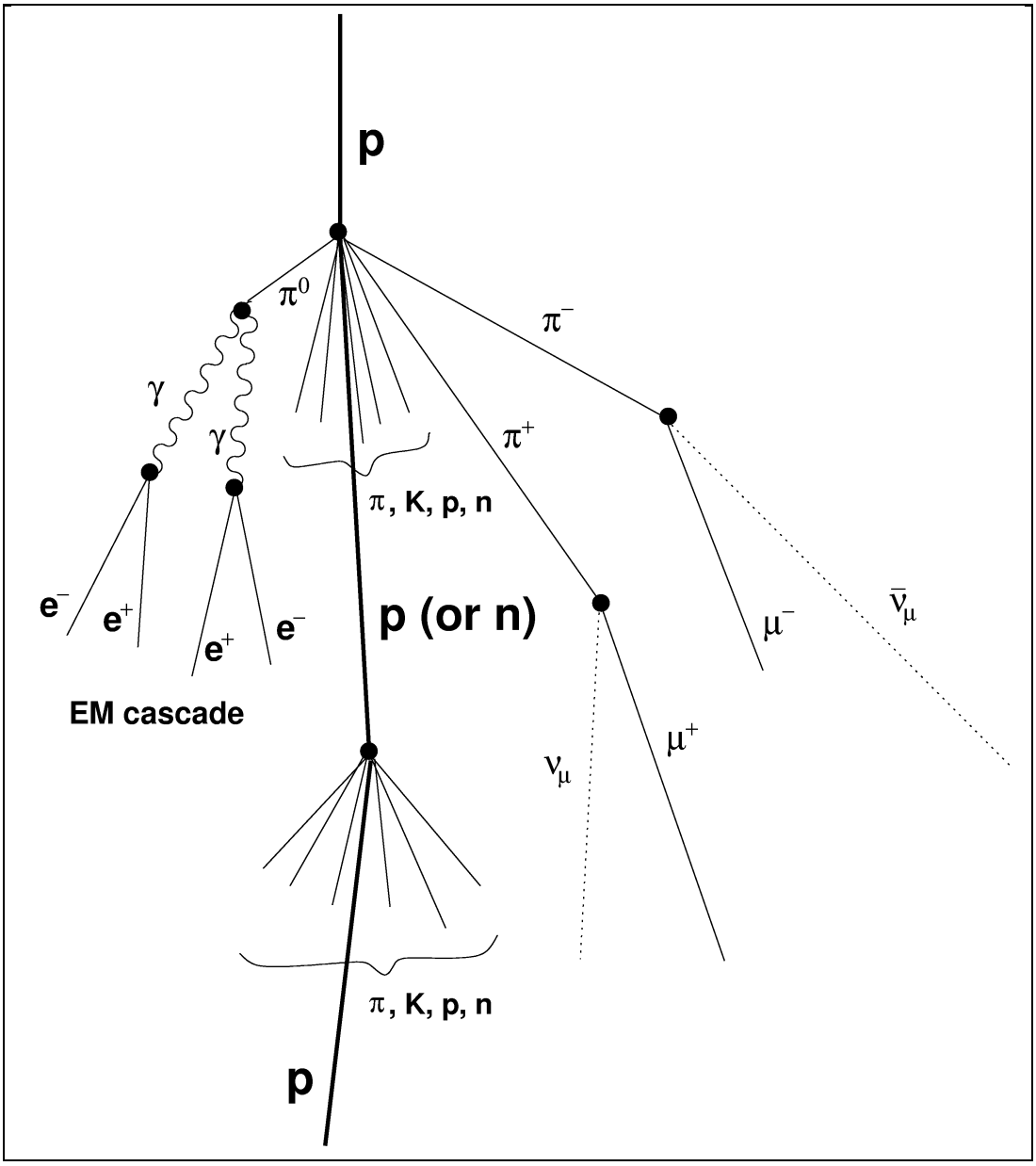

Figure 2.1. Components of an extensive air shower, exaggerated for clarity. Adapted from [34].

eta particles in the hadronic core [49]. An electromagnetic subshower is initiated by each of the high-energy photons: the photon pair produces, the electron and positron lose energy by bremsstrahlung and ionization, they annihilate to produce a new photon at a lower energy, and the process repeats until the new photon is not energetic enough to pair produce. More discussion about the competition between the production and energy loss of the $e^{\pm}$ and the resulting longitudinal shower development will follow in Section 2.1.3.

Nucleons and other high-energy hadrons in the core of the shower cascade in energy as they interact with nuclei in the atmosphere. About one third of the energy in each of these interactions transits into the electromagnetic component [49]. Most of the primary energy eventually ends up in the electromagnetic component because the hadrons tend to re-interact. The electrons and positrons are thus the most prolific constituents in the thin disk of particles showering toward the ground, and most of the energy is dissipated by their ionization losses. Hadronic interactions will be discussed in more detail in Section 4.1.

Muons are primarily produced in $\pi^{\pm}$ and $K^{\pm}$ decay. Traditionally, the muons are considered separately from the electromagnetic component because they do not interact the same way the electrons and positrons do and thus give different information. Using the atmosphere as a calorimeter to measure the $e^{\pm}$ ionization losses, by the arguments of the preceding paragraphs, gives a measure of the primary energy [49]. The muons' mean free path (mfp) for bremsstrahlung is roughly two orders of magnitude larger than the total integrated path from the top of the atmosphere to the ground, so the muons do not significantly contribute to the energy deposited in the atmosphere [50]. The μ pair production mfp behaves like the bremsstrahlung mfp at GeV energies, but shortens in the TeV region. Pair production becomes the dominant muon energy loss mechanism at high energies, but it still does not contribute significantly to the overall longitudinal shower profile

development. At sub-TeV energies, ionization accounts for most of the energy loss. The loss is relatively slow (2 MeV/gm/cm^2), though. Hence once the hadrons cascade below the pion production threshold, the number of muons plateaus. A more complete discussion of the production and measurement of EAS muons, as well as the information inferred from the measurements, will occur in Section 2.1.4.

2.1.2 Branching Model

A beautifully heuristic toy model of EAS is Heitler's branching model [49, 51]. In the branching process shown in Figure 2.2, interactions are separated by exactly one collision length λ. At each vertex, the energy is split in two. At depth X, the number of branchings, n, is

$$n = X/\lambda, \tag{2.1}$$

so the number of particles, N(X), is

$$N(X) = 2^{X/\lambda}, \tag{2.2}$$

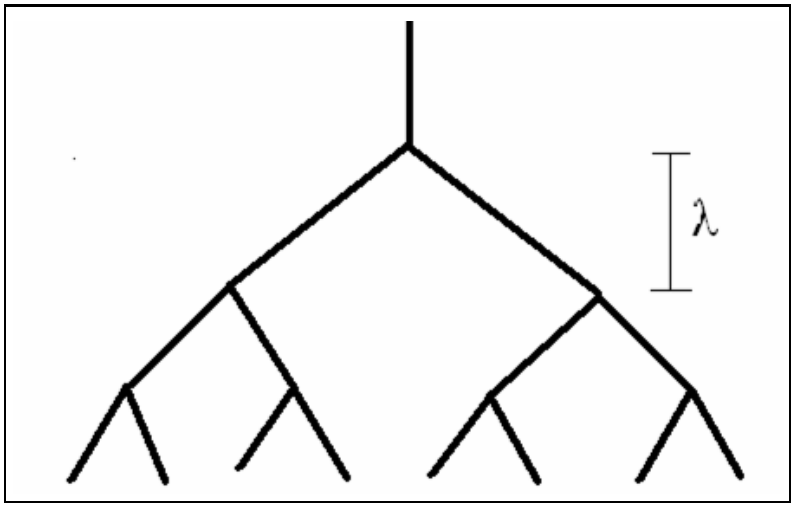

Figure 2.2. Heitler's branching model. Every characteristic length λ, the energy at each interaction point is split in two.

and the energy per particle at depth X, E(X), is

$$E(X) = E_\circ / N(X). \tag{2.3}$$

The branching will continue until the critical energy for the splitting mechanism, E_c, is reached. Above E_c, particle production and losses compete with production dominating, but below E_c particle production ceases and N(X) falls off. A typical shower profile is illustrated in Figure 2.3. The point at which E_c is reached is known as X_{max}. It follows that

$$N(X_{max}) = E_\circ / E_c, \tag{2.4}$$

and

$$X_{max} = \lambda \frac{\ln(E_\circ / E_c)}{\ln 2}. \tag{2.5}$$

Two very important features of this model are that

$$N_{max} \propto E_\circ \tag{2.6}$$

and

$$X_{max} \propto \ln(E_\circ). \tag{2.7}$$

Consider next if the primary particle is a nucleus. The branching model is extended by superposition: the shower is assumed to be a superposition of subshowers each initiated by one of the A independent nucleons. The primary energy must be divided among the A constituents, so now

$$X_{max} \propto \lambda \ln \left[\frac{E_\circ}{A E_c} \right] \tag{2.8}$$

This encouraging result suggests that by observing the longitudinal development of the EAS and measuring X_{max}, information about the composition of the primary nucleus can be obtained.

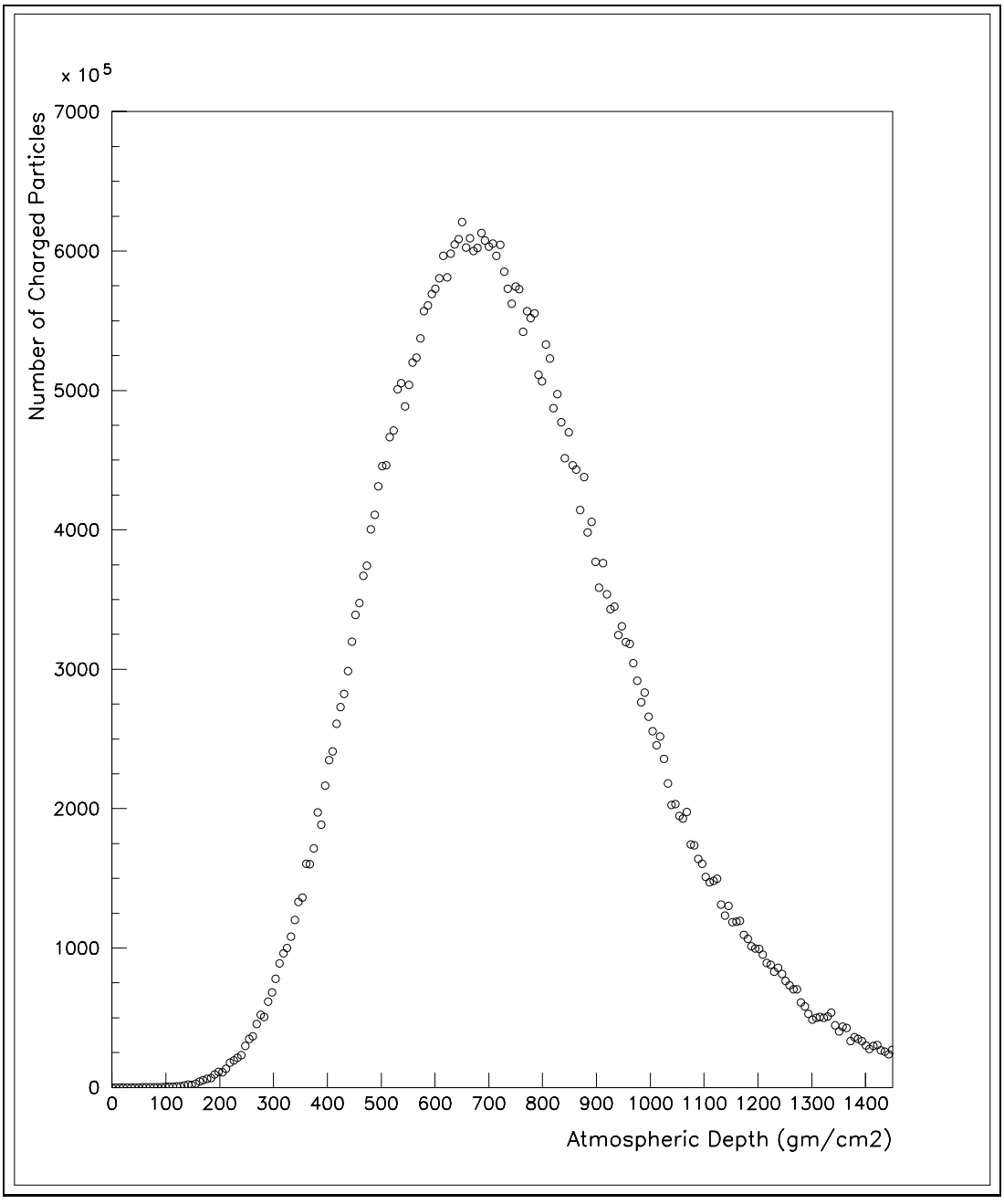

Figure 2.3. Typical shower profile generated by CORSIKA.

2.1.3 Elongation Rate

Reality is not as simple as Hietler's model. The interactions do not occur in intervals of exactly λ, and the energy is not exactly split at each vertex. All of these processes depend on the interaction cross-sections, which are functions of energy and scattering angle. In an EAS, the particles that transport energy to the atmosphere are the particles carrying away the most energy from the interaction.

These particles have small transverse momenta and thus have small scattering angles. At relevant energies, particle accelerator experiments cannot instrument the beam line, so they cannot acquire small-scattering-angle data for the first few generations of a particle cascade [104]. The interesting cross-sections cannot be measured. Models of hadronic interactions at ultra-high energies, which will be discussed in more detail in Section 4.1, must use cross-sections that are based on the cross-sections measured with accelerator data and then extrapolated over scattering angle as well as several orders of magnitude of energy.

As mentioned above, the best way to determine the composition of a cosmic ray would be to stop it in a detector, which cannot be done with UHECR. The next best way would be to measure the first interaction depth, X_1.[1] The primary particle is still intact at X_1, so the distribution of depths of first interaction gives information about the cross-section of and thus the composition of the UHECR. However, at X_1 the primary particle still has all the energy. The concern about lack of knowledge of cross-sections at high energy and in the first few generations of the cascade is amplified at the point of first interaction. Nonetheless, measuring one interaction at X_1 would be better than measuring the results of many cascading interactions, each with different species of particles, different energies, and different unknown cross-sections.

[1] In this work, X_1 will refer to the depth of the first interaction, and $X_\circ$ will refer to a fitting parameter in the Gaisser-Hillas function (see Sections 2.2.1 and 4.2.1).

Unfortunately, X_1 is not easily measured. As will be explained more fully in Section 2.2.1, fluorescence detectors depend on the scintillation light generated by the de-excitations of nitrogen in the atmosphere. In an EAS with millions of particles, copious fluorescence photons are produced as the cascading charged particles excite the atmospheric nitrogen. But at X_1, too little light is produced in the first interaction for any kind of measurement to be made, removing the second-best option for composition measurements.

With no opportunity to capture UHECR in detectors and so little light at X_1, the best observable for composition measurements by fluorescence detectors is X_{max}. However, X_{max} depends not only on the composition and energy of the primary particle, but also on the cross-sections which are simply probabilities of interaction. Measuring X_{max} for one EAS cannot give the composition of the primary that initiated that shower, but Eq. (2.8) hints that measuring how X_{max} changes with energy can indicate how the composition is changing. The rate of change of X_{max} with the log of the energy of the primary, $dX_{max}/d\log(E_\circ)$, is known as the Elongation Rate (ER), dentoed by α [52].

Admittedly, reality is not as simple as the branching model, but Eq. (2.8) is a good place to start exploring α. Re-writing Eq. (2.8) in terms of $\log_{10}$ instead of the natural log,

$$X_{max} = K\lambda \log\left[\frac{E_\circ}{AE_C}\right] = K\lambda[\log(E_\circ) - \log(A) - \log(E_c)] \tag{2.9}$$

K and E_c are constant, and λ is assumed constant within a $d\log(E_\circ)$ interval, so α is

$$\frac{dX_{max}}{d\log(E_\circ)} = K\lambda\left[1 - \frac{d\log(A)}{d\log(E_\circ)}\right] \tag{2.10}$$

or, more properly for the observables,

$$\alpha = \frac{d\langle X_{max}\rangle}{d\log(E_\circ)} = K\lambda\left[1 - \frac{d\log(\langle A\rangle)}{d\log(E_\circ)}\right] \tag{2.11}$$

If the composition as a function of energy is constant, α is a constant with a value determined by the collision length λ (which of course is a function of the interaction cross-section). In a given energy interval, a disparity between α and $K\lambda$, is evidence for a changing composition. It must be remembered that λ is also energy dependent [53], and that the various hadronic interaction models treat the energy dependence differently. This is accounted for this by finding α as a function of energy for two different hadronic interaction models. Section 4.1 will show that even though one of the largest problems remains separating the effects of particle physics and the effects of a changing composition, for most models considered, α is nearly constant and only slightly dependent on model assumptions [54].

A more complete discussion of α—one that starts with a model much more comprehensive than Heitler's—leads to Linsley's elongation rate theorem [54, 55], which is

$$\alpha = (1 - B)K\lambda \left[1 - \frac{dlog(\langle A \rangle)}{dlog(E_\circ)}\right] \tag{2.12}$$

where B expresses the dependence of α on the hadron-air nucleus interactions. It includes not only the energy dependence of the cross-sections (and hence λ), but also the energy dependence of the multiplicity, or how many particles of a given species are produced in a single interaction [53, 56]. How these energy dependences are handled by and evidenced in the different hadronic interaction models will be discussed in Section 4.1.

Other potential indicators of composition measurable with an air fluorescence detector exist [57] and will be discussed in Section 4.3. That discussion will show that, especially taking into account the UHECR event rates, the Elongation Rate is the best measure of changes in the UHECR composition.

2.1.4 ρ_μ(600)

Ground arrays do not see the longitudinal shower development and thus must infer X_{max} [34]. Additionally, they make measurements of the lateral distribution, which will be discussed here briefly.

Multiple Coulomb scattering of low-energy electrons introduces a lateral spread to the electromagnetic component. For an electron with energy E traversing a thickness δt, the mean square deflection is [49]

$$\langle \delta\theta^2 \rangle = \left(\frac{21Mev}{E}\right)^2 \delta t \tag{2.13}$$

Nishimura and Kamata [58] and Greisen [59] showed that an approximate description of the lateral distribution of the electrons is

$$\rho(N_e, r) = \frac{N_e}{{r_M}^2} f_{NKG}(r/r_M) \tag{2.14}$$

where the NKG function is given by

$$f_{NKG} = C(s)\left(\frac{r}{r_M}\right)^{s-2}\left(1+\frac{r}{r_M}\right)^{s-4.5} \tag{2.15}$$

for the shower age, s,

$$s = \frac{3X}{X+2X_{max}} \tag{2.16}$$

C(s) is an age-dependent normalization factor. The characteristic length scale for the spread of shower electrons, r_M, is the Moliere unit and is approximately 9.3 gm/cm^2 [49]. The lateral distribution of the muonic component has been experimentally determined to be related to the total number of charged particles N_{cp} by [48]

$$\rho(N_\mu, r) = 18\left(\frac{N_{cp}}{10^6}\right)^{3/4} r^{-3/4}\left(1+\frac{r}{320m}\right)^{-2.5} \tag{2.17}$$

Quark-gluon jets from hadronic interactions introduce a transverse component to the momentum of the hadrons in the EAS. The modeling of the transverse

momentum distribution is at the heart of the differences in the hadronic interaction models described in Section 4.1.

Hillas found that the fluctuation in charged particle density is less sensitive to fluctuations in the shower development far from the shower core than it is near the shower core [60, 61]. At large distances from the core, particle densities are more dependent on shower development at X_{max}, where the fluctuations are relatively small, whereas particle densities at the core depend largely on particles produced late in the shower development [57]. The density of all charged particles at 600-1000 meters from the shower core (600 has been a popular choice) can be used to measure the energy of the primary.

With the energy known, the muon density at 600 m from the shower core, $\rho_\mu(600)$, can be used to find information about the composition of the primary cosmic ray. The number of muons produced depends on the likelihood that a $\pi^\pm$ will decay rather than interact. At high altitudes, with corresponding low air density, the pions are more likely to decay into muons. The muons with enough energy to survive to reach ground are produced in the early stages of the shower and are thus related to the composition of the primary. Referring again to the branching model as an illustrative tool, the nucleus with A nucleons must divide its energy among the nucleons and will hence be less prolific than protons at producing high energy muons [49]. In this way, ground arrays use the change in muon density as a function of energy to measure changes in composition [40], but because the muons are produced from the decay of pions produced in hadronic interactions, these measurements are highly dependent on the hadronic interaction model used.

2.2 Detecting EAS

The basic picture of EAS development is now clear. The primary particle interacts with the atmosphere, creating a hadronic core. The decay of pions and

kaons in the core creates an electromagnetic component and a muonic component. The particles multiply until a critical energy, below which the loss mechanisms dominate and the shower size decreases. All three components spread out forming a thin disk of particles traveling through the atmosphere at nearly the speed of light. These relativistic particles can be detected directly or through the Čerenkov or scintillation light they produce.[2]

2.2.1 Air Fluorescence

As the charged particles pass through the atmosphere, they ionize the abundant nitrogen. The spectrum and the fluorescence yield have both been measured [8, 63]. The fluorescence yield is only about four photons per particle per meter, but UHECR-initiated EAS contain billions of particles. The photons, mostly in the 300-400 nm range in the ultraviolet (see Figure 2.4), propagate isotropically from the shore core, with the number of photons coming from a place in the shower proportional to the number of charged particles at that point.

Air Fluorescence detectors exploit this atmospheric scintillation effect. Typically, the detectors are comprised of several cameras. Each camera has a mirror that gathers the fluorescence photons and focuses them onto an array of PMTs. The PMTs amplify the signal, which is then processed by associated electronics. Each camera views a piece of the sky, and a composite view is recovered when the images from the constituent cameras are viewed together.

The advantage of air fluorescence detectors is that they view the longitudinal development of the EAS. As has been mentioned, the shower builds until X_{max}, where the energy of the primary is dispersed among so many daughter particles that none is above the threshold for new particle production. The shower size then

[2]Some detectors are designed specifically to measure the Čerenkov light, but they will not be addressed here. A good discussion can be found in [62].

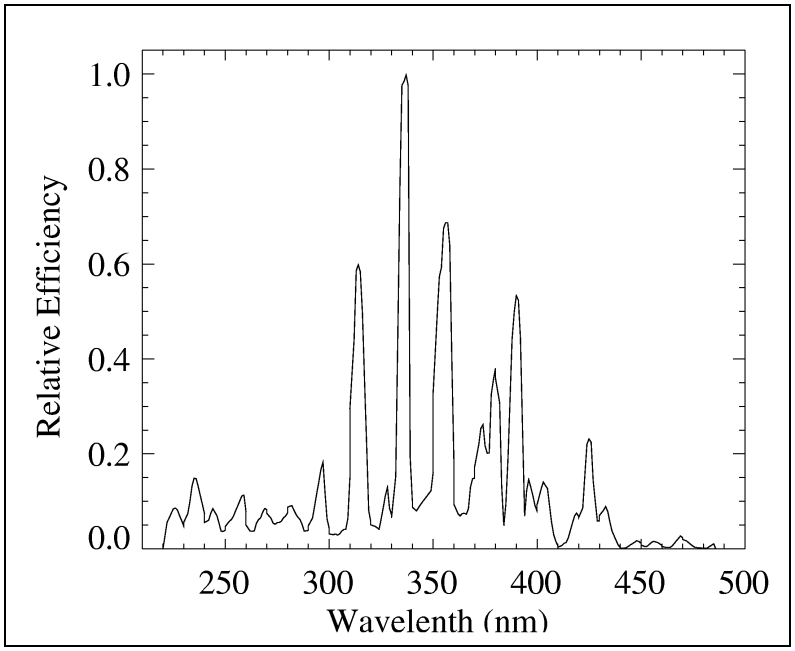

Figure 2.4. The fluorescence spectrum of nitrogen. Adapted from [8].

decreases. A parameterization of the shower profile based on experiment [2] and cascade theory [64] was conceived by Gaisser and Hillas [65]:

$$N(X) = N_{max}\left(\frac{X - X_\circ}{X_{max} - X_\circ}\right)^{(X_{max}-X_\circ)/\lambda} \exp\left[\frac{(X_{max} - X)}{\lambda}\right]. \qquad (2.18)$$

In Eq. (2.18), X is the atmospheric depth in gm/cm^2, N(X) is the number of particles—i.e., shower size—at X, X_{max} is the depth of shower maximum, $X_\circ$ is a fitting parameter, and λ is a characteristic length parameter which is also allowed to vary in the fit.[3] Figure 2.5 illustrates a typical shower fitted with the Gaisser-Hillas function.

Air fluorescence detectors do not always view the full length of the EAS. The portion that is viewed can be fit to Eq. (2.18), and then the energy of the primary

[3] $X_\circ$ and λ are sometimes mistakenly referred to as the first interaction point and the mean free path [34]. In this work, X_1 will refer to the depth of the first interaction, and $X_\circ$ and λ will be treated as fitting parameters in the Gaisser-Hillas function.

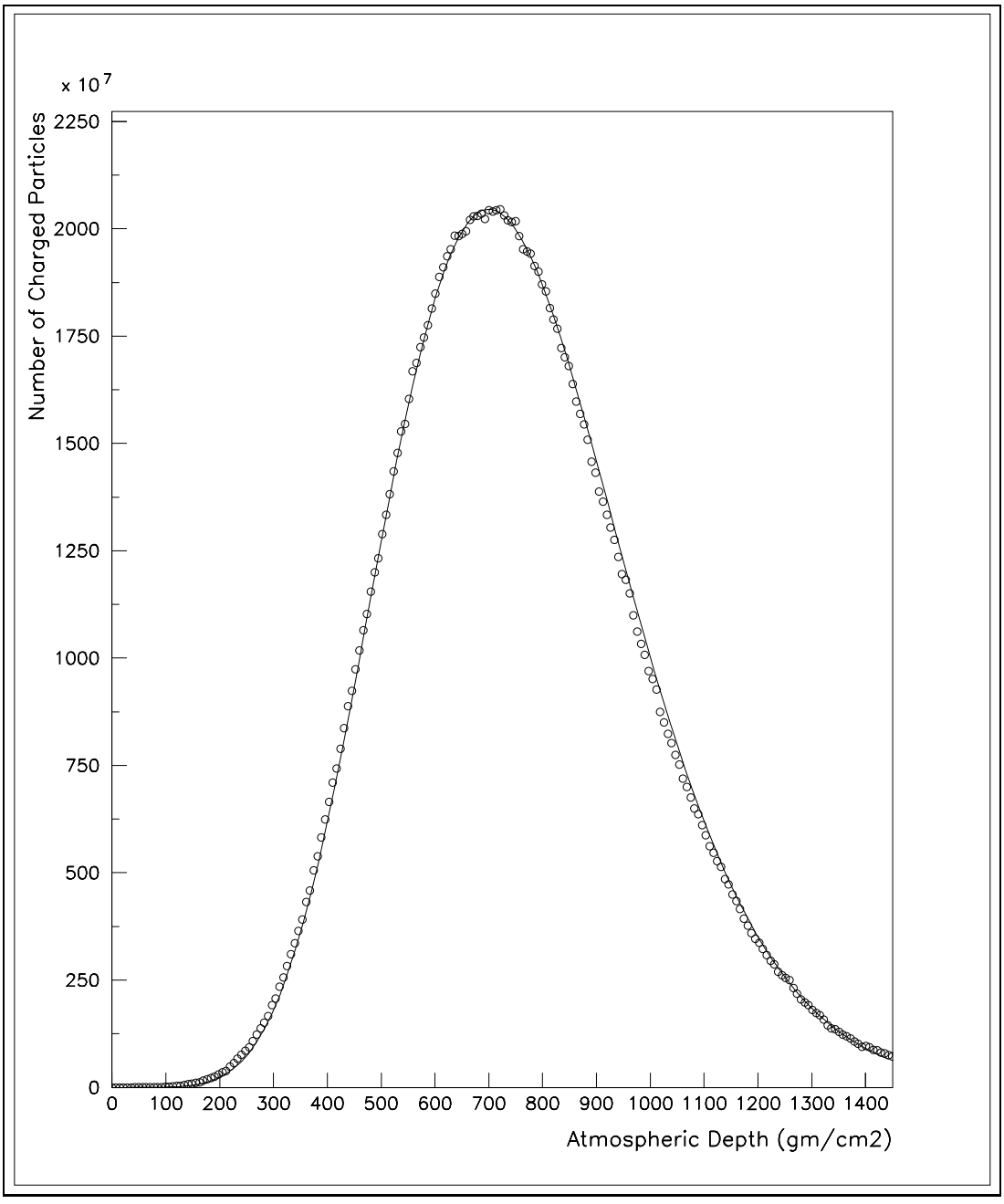

Figure 2.5. Typical Gaisser-Hillas fit to a shower profile

particle can be determined by integrating over the entire shower. As explained in Section 2.1.3, the depth of shower maximum can be used to extract information on the composition of the primary particle. The geometry of the event can be determined by the intersection of the line of the shower and the detector. More details of EAS reconstruction will be discussed in Section 5.2.

The disadvantages of air fluorescence detectors are that they have only high enough signal-to-noise ratio on moonless nights. Additionally, the presence of clouds or atmospheric anomalies may reduce or destroy viewing capabilities. Consequently, air fluorescence detectors typically have a duty cycle of about 10%.

For air fluorescence detectors, the atmosphere not only provides a scintillation medium for photons produced by EAS, but it also acts as the transmission medium for those photons. A thorough understanding of ultraviolet transmission in air in general and of the specific view conditions on any given night in particular is essential.

2.2.2 Ground Arrays

Ground arrays sample the particles of the shower with an array of separated detectors. Scintillators or water Čerenkov detectors measure the $e^{\pm}$ and $\mu^{\pm}$, the densities of which are used to determine the energy and composition as discussed in Section 2.1.4.

The lateral density distribution of the EAS particles can be used to measure the core position quite accurately if the core falls within the array, or to infer the core position if the core falls outside the array. Although they spread laterally, the particles remain fairly closely grouped longitudinally in a "pancake" shape. The particles at the leading edge of the pancake form a slightly curved shower front. The arrival direction of the shower can be determined by the relative arrival times of the shower front at the array elements.

Because the UHECR flux is low, ground arrays must cover large areas to be effective. On the other hand, they can operate at any time of day and in any weather, so they theoretically have the potential for 100% duty cycle. Another disadvantage of ground arrays is their heavy dependence on Monte Carlo simulations, and especially on the hadronic interaction models used [66].

CHAPTER 3

THE HIGH RESOLUTION FLY'S EYE COSMIC RAY OBSERVATORY

The High Resolution Fly's Eye Cosmic Ray Observatory (HiRes) is comprised of two sites on the U.S. Army's Dugway Proving Ground in the West Desert of Utah, about 90 miles from Salt Lake City and the University of Utah campus. The first site, HiRes-1, is on Little Granite Mountain, the original site of the Fly's Eye detector. HiRes-2 is 12.6 km to the southwest on Camel's Back Ridge. Dugway was chosen for its clean atmosphere and low light pollution. Additionally, each site is on a hill, above the bulk of most haze in the atmosphere.[1] The two sites gather data independently, and the data can be analyzed from each site in monocular mode or together in stereo mode. Reports of monocular analysis exist [66, 67]; this work will present results from stereo analysis. This chapter will describe the detectors at each HiRes site as well as the calibration of the detector and the atmosphere.

3.1 The HiRes Detector

HiRes is the realization of an extension of the method pioneered by the original Fly's Eye. The HiRes Prototype detector, located on Little Granite Mountain, incorporated high temporal resolution with Sample-and-Hold (S&H) electronics (described below) similar in concept to Fly's Eye electronics [16]. The prototype

[1] More discussion of the Dugway atmosphere will be presented in Sections 3.3, 5.3.1, and 6.1.1.

detector viewed from 3° to 70° in elevation and was arranged with an azimuthal coverage that overlooked the Michigan Muon Array (MIA) 3.4 km away. Studies showed that the aperture for events at 10^{20} eV would be optimized if the mirrors were redeployed in a ring with full 360° azimuthal coverage and 3° to 17° elevational coverage [67]. In 1997, the redeployment of the prototype cameras at Little Granite Mountain began. In parallel with the repositioning, work began on improved S&H electronics for the additional cameras needed to complete the HiRes-1 site and on an FADC data acquisition system for the then-planned HiRes-2 site. HiRes-1 began taking data in May of 1997, and the ring was complete in March of 1998.

HiRes-2 has two rings, giving complete azimuthal coverage with an elevational coverage from 3° to 31°. The cameras at HiRes-2 which face HiRes-1 were the first to be installed. Some data from a HiRes-2 prototype configuration were gathered, but this report uses only data after November of 1999, which is when HiRes-2 was completely operational.

Figures 3.1 and 3.2, taken from the HiRes event display, show the orientation of the cameras at the two sites. North is up, the zenith is at the center of each display, and the horizon is at the outer edge. Cameras 2 and 4 at HiRes-2 point toward HiRes-1, and camera 7 at HiRes-1 points toward HiRes-2. The basic element of HiRes is a camera consisting of a mirror with an associated cluster of photo-multiplier tubes (PMTs) and data-acquisition (DAQ) electronics. The mirror is assembled from four spherical quadrants with a total area of 4.18 m^2. The PMT cluster is placed at a distance from the mirror which optimizes the spot size.[2] Considering obscuration from the cluster, the effective area of each mirror is 3.72 m^2 [67].

[2] An excellent discussion of spot-size and related HiRes optics issues can be found in [34].

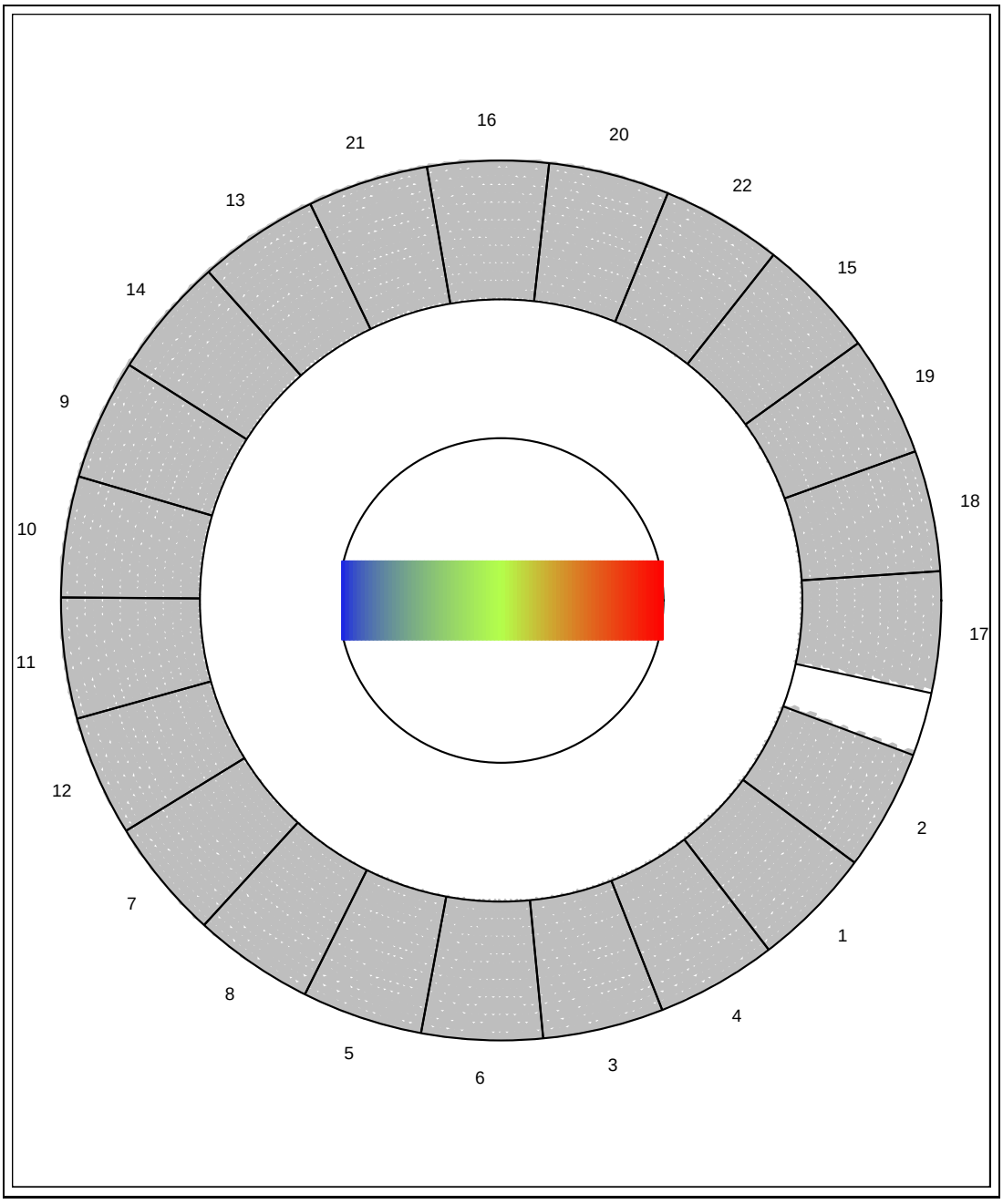

Figure 3.1. HiRes-1 event display. Camera 7 points to HiRes-2.

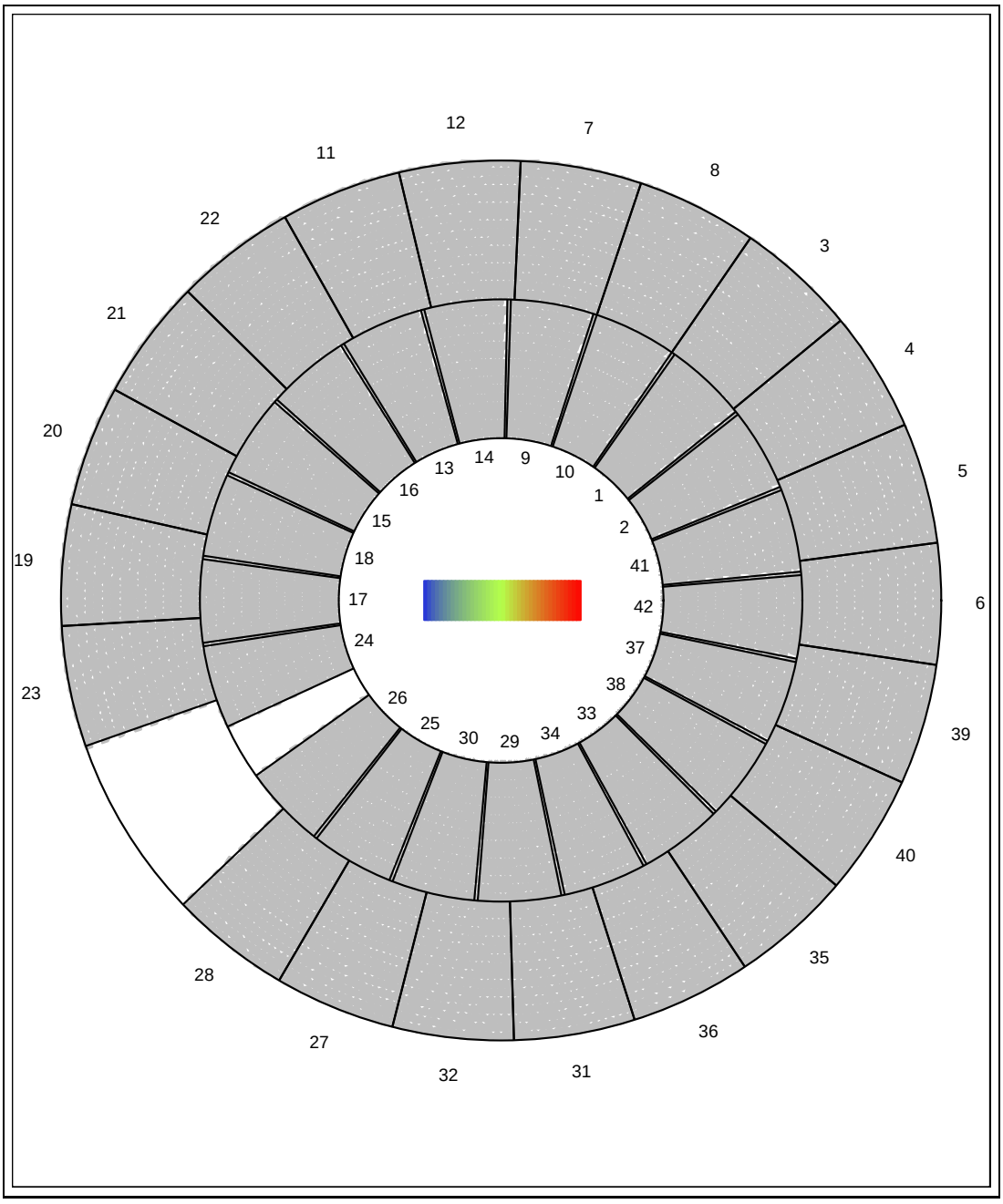

Figure 3.2. HiRes-2 event display. Cameras 2 and 4 point to HiRes-1.

The PMT cluster contains 16 rows of 16 hexagonal-faced PMTs 40 mm in diameter.[3] The backplane of the cluster box routes high and low voltage to the PMTs for distribution to the dynodes and the attached preamplifiers, respectively. With the chosen mirror-cluster arrangement, each tube has an angular coverage of approximately $1^\circ \times 1^\circ$, resulting in an angular coverage of $16^\circ \times 14^\circ$ for the entire cluster. A UV-pass filter is mounted in front of the PMTs to improve the signal-to-noise ratio [70].

3.1.1 HiRes-1

The HiRes-1 cameras are housed in 12 shelters. The detector is operated from a central facility which houses the DAQ computer and a GPS-based Central Timing crate (CT). The individual camera's electronics are connected to the DAQ computer via Ethernet and to CT via dedicated timing cables. Each camera's electronics crate houses 16 readout boards, a trigger logic board, a CPU board, a Programmable Pulse Generator (PPG) card, and a so-called "garbage" board.

Each readout board—known as ommatidial boards (OMB) because they function similarly to the ommatidial nerve in a fly's eye—acquires data from sixteen PMTs. The S&H electronics record the triggering time and integrated charge once the integrated charge reaches some threshold level. The threshold is dynamically adjusted as the sky noise changes to maintain a trigger rate of 200 Hz [69].

The trigger logic boards compare the individual tube triggers to preset patterns to determine if a mirror trigger should be generated [34, 68]. When a mirror triggers, the PMT charge and timing information are digitized (charge-to-digital $\longrightarrow$ QDC; time-to-digital $\longrightarrow$ TDC). The CPU board communicates with CT to get a time

[3] A detailed listing of HiRes PMT specifications is available in [16, 67, 68, 69].

stamp, gathers the QDC and TDC information, and sends it to the DAQ computer. The QDCs in the S&H system give the total integrated charge in a 5.6 μs time gate.

The PPG board generates waveforms for electronic calibration. The garbage board performs myriad functions such as building door control, environmental sensing, and interlock monitoring.

3.1.2 HiRes-2

As at HiRes-1, the HiRes-2 detector site is controlled from a central facility. Each of 21 buildings on Camel's Back Ridge houses two cameras, and the cameras share an electronics rack. The racks communicate via bi-directional, serially connected optical fiber [71]. The optical fiber network is used for all communications, including a site-wide time signal from the central 10 MHz clock, commands from the control computer, and data from the cameras to the DAQ computer.

In the electronics racks, each FADC module digitizes data from sixteen PMTs in a vertical column. Row and column sums are also collected, at a lower gain, to allow the detector a wider dynamic range. The gain of each channel is controlled individually and electronically. Incoming signals are digitized every 100 ns by 8-bit FADCs.

Every 100 ns, the Trigger/Host module for a camera compares all 16 column sums and all 16 row sums to a trigger threshold. If the threshold is exceeded with appropriate column or row coincidences, the data for every channel are read out to local memory where more rigorous camera-level triggering criteria are applied. If a trigger is confirmed, the FADC data is sent to the DAQ computer.

An additional module in the electronics crate monitors system temperature, voltage, and current, interlock status, and light levels. This module can also control the building doors, heat exchangers on the rack, and a programmable 32-channel pulser for each camera.

3.2 Calibration

Obtaining the number of photons incident on a PMT from its QDC or FADC information requires a calibration procedure which accounts for the tube's quantum efficiency (QE) as a function of position and its electronic gain. Additionally, to find the number of photons incident on the camera requires understanding the transmission of the UV-pass filter and the reflectivity of the mirror.

Each tube, before being placed in a cluster, was screened at a photo-tube calibration facility [72]. A subcluster of 16 tubes was placed on a translation table with a NIST-calibrated photodiode. Light at 325 nm from a He-Cd laser was passed through a standard HiRes UV-pass and filter and aimed at a beam splitter. A small fraction of the light went to a second photodiode which continuously monitored the laser output. The remainder of the light passed through the splitter, and 1 mm spot illuminated the calibrated photodiode. After comparisons between the two photodiodes established the relationship between laser output and light delivered to the subcluster, the translation table was moved to scan the face of each tube. The gain G of a PMT goes as $G \propto e^{\alpha}V^{\beta}$. By moving the scanning table and varying the voltage, the active area, the sensitivity, and the constants α and β were measured at seven points across each PMT face. Figure 3.3 shows a typical tube response profile. The QE was found not found to vary much from tube to tube [68], and QE was also consistent with the manufacturer's specifications [72].

PMTs with too small an active area, more than 20% nonuniformity across the face, or an unacceptably low sensitivity or gain at a given voltage were rejected. For HiRes-1, tube operating voltages were preselected and hard-wired in the electronics crate. Tubes with similar properties were grouped together in cluster boxes, facilitating the gain balancing [67].

At HiRes-2, the tube pre-amp gains can be dynamically adjusted by software. Gain balancing for each cluster was performed in a laboratory in Salt Lake before

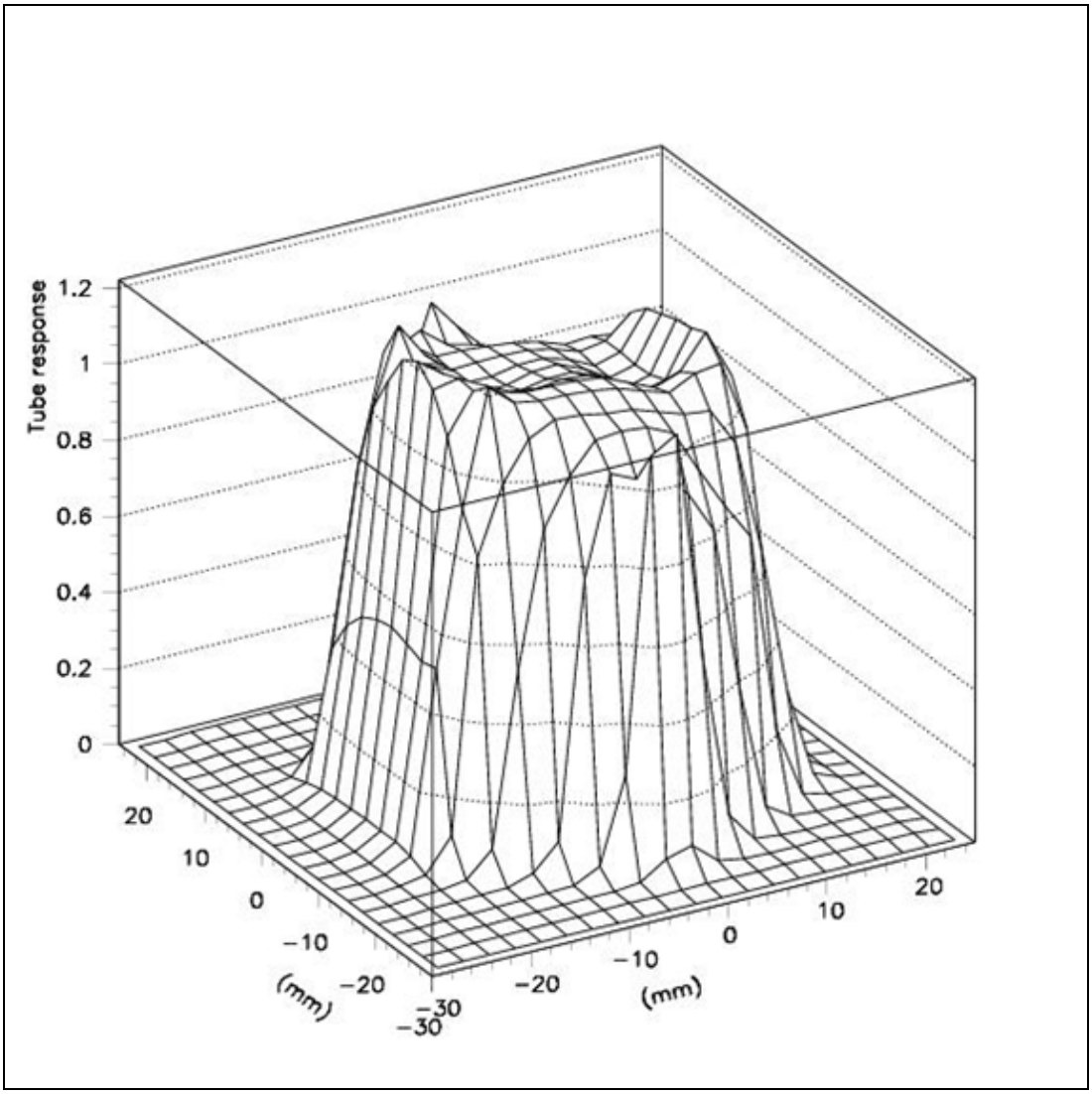

Figure 3.3. HiRes PMT response profile.

deployment to Camel's Back Ridge. Tubes which could not be brought into tolerance by software underwent a hardware change (i.e., a resistor was swapped). Gain balancing was performed again once the cluster was in place at the detector site and is still checked in the field periodically [73].

The gain and linearity of the pre-amplifiers and the OMBs (FADC boards) at HiRes-1 (HiRes-2) are measured nightly using an inserted wave form from the

installed PPG boards (channel pulser). The pulse is introduced at the pre-amplifier at the base of each tube, allowing monitoring of the remainder of the signal path [66, 71]. Although the measured response is linear over most of the dynamic range, small nonlinearities at the extremes of the QDC have been measured and parameterized [66]. At HiRes-2, the response is adjusted to give one FADC count per photoelectron, removing any concerns about nonlinearity in the low-signal-strength region [71].

The primary tool for the calibration of PMT sensitivity is a Roving Xenon Flasher (RXF). The RXF is a xenon flash bulb mounted in a portable housing. The housing can be moved from camera to camera, where it is placed in the center of the four segments of the mirror. The RXF illuminates the cluster directly. Xenon was chosen because its emission spectrum is strong in HiRes' 300-400 nm window but also broad enough to allow calibration at various wavelengths. The output of the RXF has been measured to be stable to within 1/3% flash-to-flash and within 2% over the course of a night [74, 75].

At HiRes-1, the RXF is fired several hundred times with different neutral density filters between the RXF and the PMTs. Using Poisson statistics, it can be shown that

$$\mu_{pe} = \alpha \frac{{\mu_{QDC}}^2}{{\sigma_{QDC}}^2} \tag{3.1}$$

where μ_{pe} is the mean number of photoelectrons, $\alpha^{1/2}$ is the PMT excess noise factor, and μ_{QDC} and σ_{QDC} are the mean and standard deviation of the QDC measurement, respectively [75]. The gain is the slope of a plot of pedestal-subtracted QDC counts vs number of photo electrons, as shown in Figure 3.4. (The YAG laser point in Figure 3.4 will be discussed below.)

Before the development of the calibration method which uses Eq. (3.1), analysis of RXF data assumed the RXF produced 12,000 photons per tube per flash. Data

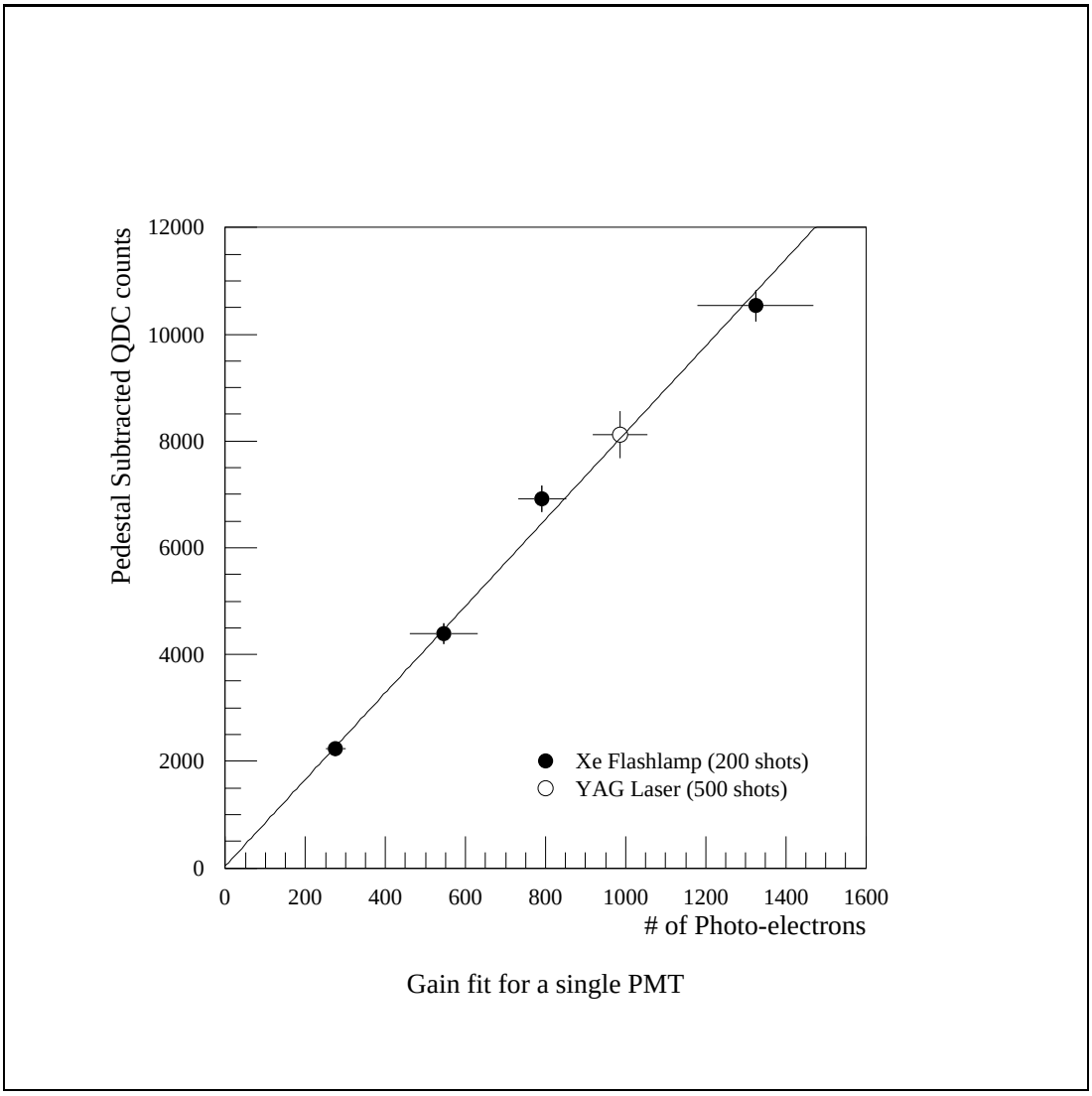

Figure 3.4. HiRes calibration plot. RXF calibration is performed about monthly, while YAG data are collected nightly. Adapted from [75]

were gathered using the same attenuating filters described above, and the measured gains agree very well with those obtained using the current method [67]. Because of this agreement and the known stability of the RXF, HiRes-2 calibration treats the RXF as a standard candle. Analysis of the RXF data also assumes a standard QE for each PMT and a standard UV-pass filter transmission curve. The software-controlled gains are then adjusted to give one FADC count per photoelectron [76].

Because the RXF can be at only one camera at a time, RXF calibration is time consuming and labor intensive. To monitor the PMT response on a nightly basis, each site has a frequency-tripled YAG laser which delivers light at 355 nm to each camera via quartz optical fibers. One fiber goes to the center of each mirror, and one to each side of each PMT cluster. The mirror-mounted fibers illuminate the cluster directly allowing monitoring of tube response, while the cluster-mounted fibers illuminate the mirrors so mirror reflectivity can be tracked.

Teflon diffusers at the ends of the fibers ensure uniform illumination of the PMTs. Because of nonuniform illumination of the fibers at the laser and differing fiber lengths, the thickness of each diffuser, and therefore the amount of attenuation at the end of each fiber, must be chosen to properly balance the light intensity at each camera.

The YAG Laser point in Figure 3.4 was obtained from YAG shots on the same night as the RXF calibration shown. The YAG data was analyzed with the method utilizing equation 3.1 described above. The agreement is excellent [75].

Both the mirror-mounted and the cluster-mounted fibers are illuminated several hundred times at both sites at the beginning and end of each nightly run. At HiRes-1, both sets of fibers are also illuminated at the end of the run, while only the mirror-mounted fibers are used at the end of the night at HiRes-2. Monitoring shots from the mirror-mounted fibers during the run were recently implemented at HiRes-2.

Each time the HiRes-2 YAG system fires, the energy from the laser and the energy delivered to the fiber bundle are recorded. Using a cron job, the log file is automatically transferred each morning to the University of Utah campus, where the data are automatically analyzed. A slide-show display of average laser energy and the ratios of bundle-energy-to-laser-energy automatically updates, giving a picture of both the current and the historical health and performance of the laser and its associated optical elements.

The YAG calibration data are not used in analysis yet, but significant efforts are underway to implement the information [77]. More details about the YAG systems can be found in [78] for HiRes-1 and [79, 80] for HiRes-2.

3.3 Atmospherics

Although the PMT and electronic calibrations allow determination of the number of photons incident on the camera from the measured QDC/FADC, full reconstruction of EAS requires knowing the number of charged particles at the shower. Because fluorescence photons from EAS are generated in and must travel through the atmosphere to reach the cameras, an understanding of the atmosphere is vital. Molecular scattering is well-understood, and molecular density profile variations from the U.S. Standard Atmosphere of 1976 [81] are small [82]. However, the aerosol scattering phase functions are less well-known and the aerosol spatial distribution in the atmosphere changes extensively and often. Atmospheric monitoring tools include operator observations, cloud monitors, xenon flashers, and steerable YAG lasers.

Hourly, the operator logs the weather conditions with special attention to the cloud cover. Cuts based on logged weather conditions will be discussed in Section 6.1.1.

A more objective measure of the cloud cover is made with infra-red sensors. About half the buildings at HiRes-1 have stationary $30^\circ \times 30^\circ$ sensors mounted on the stands that hold the PMT clusters. The monitors indicate when a cloud, which is much warmer than the deep-space background, enters the field of view. Additionally, a scanning cloud monitor samples the 2π steradians above and around HiRes-1 every 12-15 minutes. At HiRes-2 clouds are clearly visible in FADC snapshots of the night sky, so no other cloud monitoring devices are installed. None of the cloud monitoring information has yet to be incorporated in the analysis.

One inclined xenon flasher is mounted at the old Fly's Eye-II site. For historical reasons (i.e., the flasher sent light from Fly's Eye-II to Fly's Eye-I), this device is known as the Inter-Site Flasher (ISF). The ISF track now goes between HiRes-1 and HiRes-2. Eleven mirrors in HiRes-1 see the ISF, giving a wide range of scattering angles and affording an opportunity to investigate the amount of aerosol on a local level [67].

Ten vertical xenon flashers are deployed between HiRes-1 and HiRes-2 as shown in Figure 3.5. The flashers are fired throughout the run by radio signals originating at HiRes-2. A detailed description of the vertical flashers can be found in [83]. Because the ISF and some of the vertical flashers are seen in both detectors, they provide the most robust criterion for determining the acceptability of data. If flashers are not seen by both detectors in a time-matched data file, then the aperture was too hazy or the absolute timing between the sites was offset during the time that data was acquired.

The entire aperture of the detector is probed hourly by steerable frequency-tripled YAG lasers [84, 85]. For this analysis, the steerable laser at HiRes-2, which is seen by HiRes-1, is used.[4] The laser fires at predetermined azimuth and elevation

[4] Although a steerable laser has been installed at HiRes-1, it was not in operation during the collection of this data set.

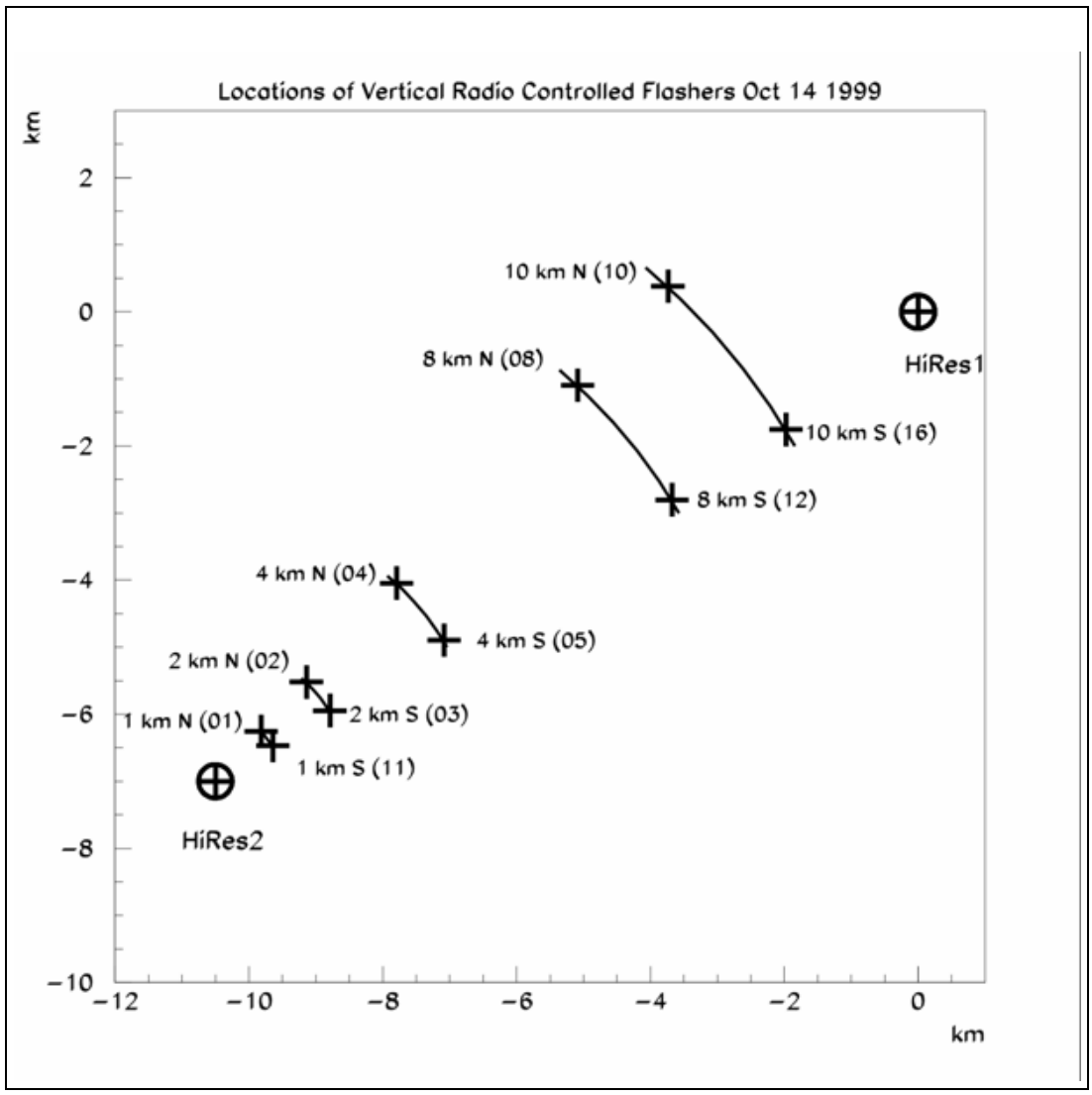

Figure 3.5. Map of vertical flashers.

pairs designed to cover the entire aperture, sweeping through its program every hour. The light scattered into the cameras at HiRes-1 gives information about the atmosphere.

The atmosphere can be considered a mix of molecules and aerosols, where the term "aerosols" is used to describe dust, haze, and everything else that is not molecular. Rayleigh scattering from the molecules is well understood, as is the

atmospheric density profile. Understanding Mie scattering from aerosols is more challenging. In a simplified model, the aerosol density at a given height is described by the horizontal attenuation length L^a which results from the aerosol density at that height. An exponential density fall-off with scale height H_S is assumed. With this construction, the transmittance of the aerosols T_a can then be written as

$$T_a = e^{-AOD/sin\theta} \tag{3.2}$$

where θ is the elevation angle of the tube receiving the signal and AOD, the aerosol optical depth, is [86]

$$AOD = e^{-\int_0^z \frac{\rho^a(z)dz}{L^a(\lambda)}}. \tag{3.3}$$

If $z \gg H_s$, Eq. (3.3) simplifies to

$$AOD = \frac{H_s}{L^a}. \tag{3.4}$$

Because the aerosol density profile can change on very short time scales, the aerosol horizontal attenuation length and the scale height are determined hourly, and a database of the hourly parameterizations of the atmosphere is used in the reconstruction and data analysis [76].

3.3.1 Using the Steerable Lasers to Localize Clouds

For this analysis, the AOD was the only weather criterion used. Unfortunately, the AOD is measured from vertical shots [87, 88]. If a cloud was directly above the HiRes-2 steerable laser, the AOD would be unacceptable and the entire hour of data would be thrown out even though some significant part of the aperture may have been clear.

The cloud detectors can certainly give a more localized picture of the cloud cover. Another effective tool is the steerable lasers themselves. Because the lasers

sweep the entire aperture every hour at many precise positions, the laser data can be used both to show not only which parts of the aperture were cloudy but also which parts of the aperture were clear.

Figure 3.6 shows a typical laser track in the event display on a clear night. Figure 3.7 shows an event display for the same laser geometry on a cloudy night. The difference is clear to the eye: the cloud scatters a significant amount of the laser light to tubes pointing far from the laser track. An algorithm has been developed to identify clouds at specific locations and times by exploiting the extra track width introduced by clouds.

For each tube that fires on a laser shot, the pointing direction of the tube is compared to the known track of the laser. Tubes pointing within 2° of the laser track are discounted, because they are expected to always fire, and the method is looking for extra track width introduced by scattering in clouds. For tubes pointing more than 2° from the track, the shortest distance between the tube's pointing vector and the laser track—called the off-track distance—is found. The pseudo-width is defined as the product of the off-track distance and the number of photons in that tube divided by the measured laser energy recorded for the shot. The pseudo-width for each tube triggered by the laser shot is summed.

When all tubes which fired in the shot have been considered, the resulting pseudo-width sum is divided by the track length, giving the pseudo-width-vs-length ratio (PWVLR). The PWVLR is then compared to two standards, one for obviously bad shots and the other for questionable shots, determined globally for all evaluated laser geometries. Clouds are expected to shorten and widen the track, so a large PWVLR indicates a cloud, a small PWVLR indicates no cloud, and an intermediate value indicates further investigation is required.

This method was used in conjunction with operator comments in the logs to

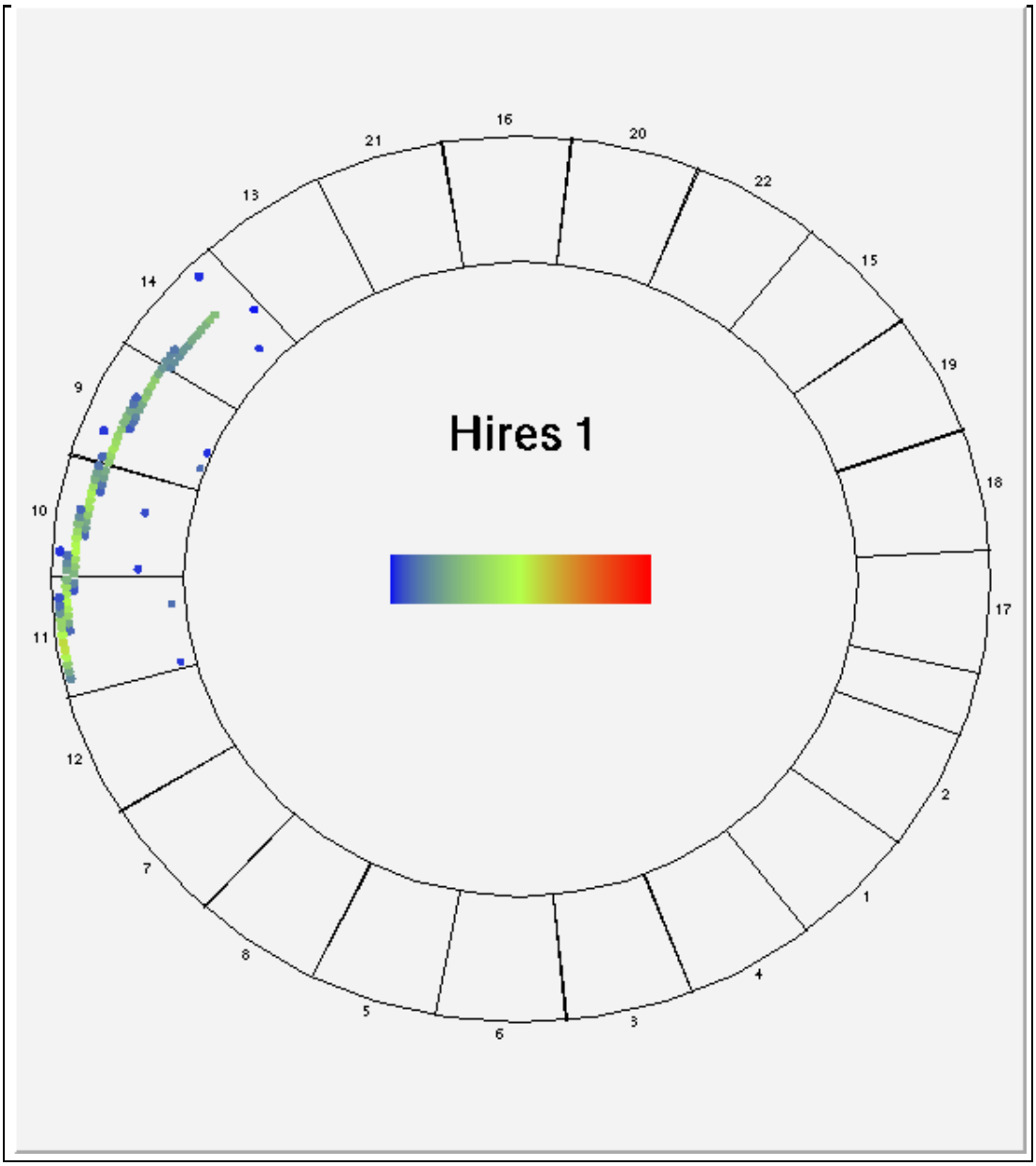

Figure 3.6. Laser track on a clear night. Note the length and width of the track. Compare Figure 3.7.

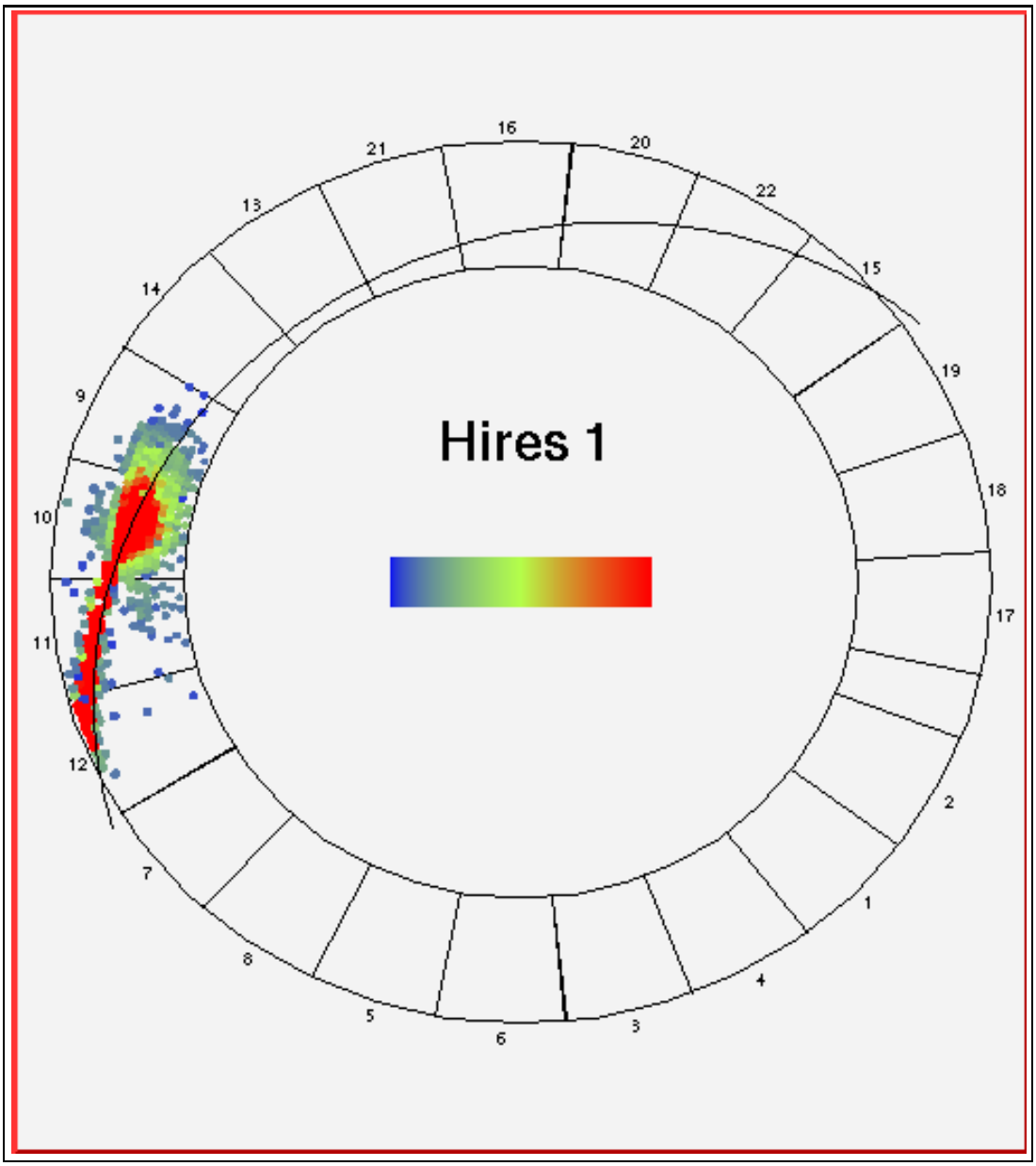

Figure 3.7. Laser track on a cloudy night. Note the length and width of the track. Compare Figure 3.6.

select nights with possible weather problems if no AOD was available in the database. Other more rigorous and complete quantitative cloud-finding algorithms are in development [89].

CHAPTER 4

EXTENSIVE AIR SHOWER SIMULATION

Because the air fluorescence technique indirectly measures a small number of showers from a steeply falling spectrum, each with its own fluctuations, "progress toward the goal of measuring the primary composition at high energy has been slow and difficult" [90]. Better measurements depend not only on better detectors but also on better EAS simulation routines and within those routines better hadronic interaction models.

Hadronic interaction models began as parameterizations of accelerator data which were extrapolated to forward angles and UHECR energies [91]. The sophisticated models in use today base the extrapolations on physically motivated models, but accelerators still cannot reach UHECR energies. Additionally, accelerator experiments cannot put instrumentation in the beam path. Consequently, data are not available in the fragmentation region so important to understanding particle cascades [91].

For this work, the QGSJet [92] and SIBYLL [91, 93] hadronic interaction models were used in the CORSIKA [94] shower generator. Each of these will be discussed further below, but the discussion will be facilitated by the introduction of the nomenclature, following [49].

- The **inelasticity** is the fraction of energy not carried away by the leading particle, which is to say the energy available for secondary particle production.

• The **multiplicity** is the number of secondary particles of a given type produced in an interaction.

4.1 CORSIKA

CORSIKA (COsmic Ray SImulations for KAscade) is a detailed EAS simulation generator [94]. Originally developed for the KASCADE experiment at Karlsruhe, Germany, it is now used by many experimental groups. CORSIKA allows simulation of showers initiated by a variety of particles, including photons and nuclei. This computational tool is flexible, allowing the use of the VENUS [95], DPMJET [96], NEXUS [97, 98], QGSJet [92], or SIBYLL [91, 93] hadronic interaction models at high energies and the UrQMD [99, 100] or GHEISHA [101] models at low energies. The electromagnetic cascades can be treated with NKG lateral distribution functions or the EGS4 routines [103].

4.1.1 QGSJet

In air shower physics, the interesting hadronic processes are labeled "soft" because they are characterized by small transverse momentum. The Quark-Gluon-String Model (QGS) uses the concept of pomeron exchange to describe the soft interactions [92]. The pomeron is an object exchanged between hadrons with the quantum number of the vacuum. A simple example in the soft regime would be a two-gluon glueball [34].

Accelerator data show that with increasing energy, the hadronic interaction cross-sections rise and the onset of mini-jet formation is observed. The mini-jets suggest the rise in cross-section is due to a growing "hard" contribution from parton-parton scattering [34]. The QGS with Jets (QGSJet) model addressed the mini-jets by introducing pomeron emission in this semihard region followed by the hard interaction of partons [92]. As the energy increases, the pomeron

can be treated as a ladder of gluons with each vertex adding to the cross-section. Additionally, parton formation can occur in qq loops in the ladder [34].

The QGSJet authors tune the pomeron parameters and the relative weights of the soft and hard contributions to the cross-section to match accelerator data. With the pomeron description complete, cross-sections are computed and extrapolated to UHECR energies [92].

4.1.2 SIBYLL

The SIBYLL hadronic interaction model superimposes mini-jet production on the Dual Parton Model (DPM) [91], which considers the interaction of each valence quark in the target and the primary. Below laboratory energies of about 200 GeV, the cross-sections follow Feynman scaling [56], and the model is verified by comparison to experimental information [91].

As in QGSJet, SIBYLL treats the mini-jet production as the onset of a "hard" part of the cross-section. Instead of introducing the pomeron, SIBYLL uses the best measurements of the electric form functions of the valence quarks, assumes a monopole distribution of the gluons around the valence quarks, and then applies perturbative QCD to calculate the interaction cross-sections [91].

The modeling of the hadron-hadron interactions is extended to hadron-nucleus collisions. These extensions and the extrapolations to the highest energies and momentum transfers are governed by the assumptions that energy-momentum conservation drives the leading particle distribution and multiple parton-parton interactions are possible in each hadron-hadron collision [93].

4.1.3 Model Comparison

The differences in the hadronic interaction models are most evident in the multiplicity, inelasticity, and hadron-air cross-section they predict. Each of these

directly affects the shower development. The QGSJet multiplicity goes as log(E), whereas the multiplicity in SIBYLL is below that of QGSJet at relevant energies and rises more slowly than log(E) (see Figure 4.1) [103]. Considering just multiplicity, QGSJet showers would be expected to age more quickly. Both models show an increase of inelasticity with energy [91, 92, 93], but QGSJet is more inelastic in the UHECR regime [34], again contributing to faster shower development predicted by QGSJet [103]. The hadron-air cross-sections in SIBYLL are larger than those of QGSJet at relevant energies. The inelastic p-air cross-section in QGSJet rises about linearly with log(E), while in SIBYLL it rises more rapidly than linearly with log(E), as illustrated in Figure 4.2 [104]. The nucleus-air cross-sections of the two models are comparable in magnitude and rise slowly with energy [34, 104].

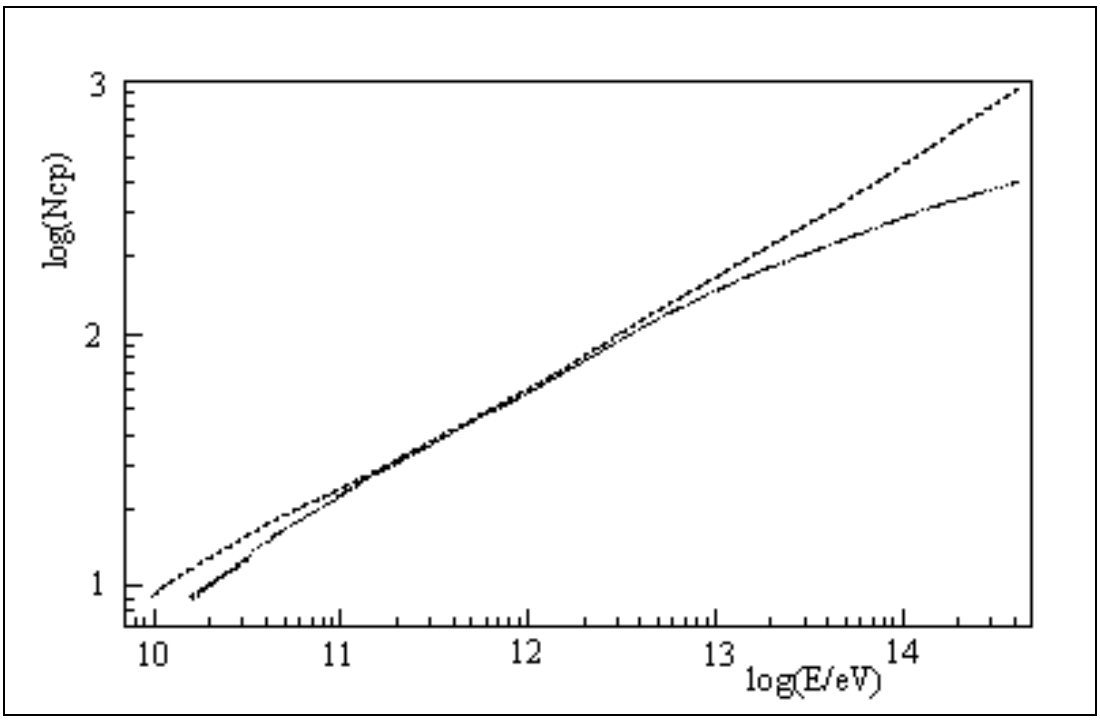

Figure 4.1. Hadronic interaction model multiplicities for proton-^{14}N collisions. The upper line is for QGSJet01 and the lower line is for SIBYLL 2.1. Adapted from [103].

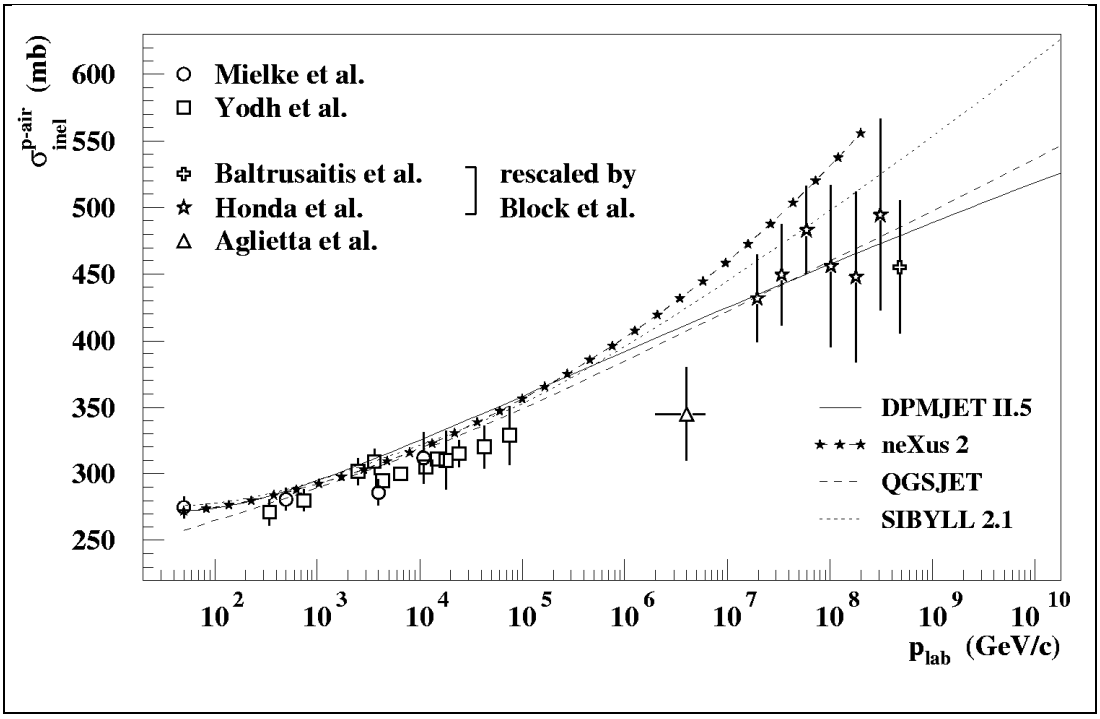

Figure 4.2. Hadronic interaction model inelastic cross-sections. Low energy data are from particle accelerators, and high energy data are from UHECR experiments. The QGSJet and SIBYLL models are considered in this work. Adapted from [104].

4.1.4 Simulation Runs

CORSIKA makes many forms of output available. For this work, the most convenient output is the longitudinal shower development in tabular form. At each 5 gm/cm^2 of vertical atmospheric depth, the numbers of gammas, positrons, electrons, muons, hadrons, nuclei, and total charged particles are listed. An accompanying table lists the longitudinal energy deposit of gammas, electrons and positrons, muons, and hadrons as well as the energy carried away by neutrinos.

For this work, simulations were generated with CORSIKA 6.005 and 6.010,[1]

[1]The CURVED option was used, so the reported problems of muon treatment in magnetic fields with the CURVED option in these versions of CORSIKA are germane. Comparison of simulation results by the CORSIKA author [103, 105] in which the CURVED option was not used and the results of locally-generated showers employing the CURVED option showed that the shower parameters measured with HiRes were not affected by this known bug.

using both QGSJet01 and SIBYLL 2.1 for both protons and iron nuclei.[2] In all simulations, the EGS4 option was selected enabling explicit treatment of each electromagnetic interaction for particles above a threshold energy. Electrons, positrons, and photons with energies below 100 keV were no longer tracked in order to conserve CPU time. Hadrons and muons with energies below 300 MeV were also cut. All showers were initiated at 45° to the vertical, so sampling at 5 gm/cm^2 of vertical atmospheric depth gave bins of about 7 gm/cm^2.

Thinning is a popular technique for reducing the CPU time needed for an EAS simulation. The basic idea is that after an interaction which generates several secondary particles below some threshold energy, only one of the particles is tracked. The selected particle will be assigned a weight such that energy is conserved, and it will then represent all of the particles emerging from the interaction [106]. Thinning in CORSIKA ensures that particle identity is roughly conserved—i.e., a positron can represent both positrons and electrons, but it could not represent a hadron [94]. The thinning procedure tends to accentuate the fluctuations in the number of charged particles in an atmospheric depth sampling bin when the behavior of the surviving particle is multiplied by the weight determined at the onset of the thinning routine. Numerous studies have shown that setting the threshold for thinning at 10-5 of the energy of the primary reduces computation time without significantly changing the results of mean X_{max} and elongation rate [34, 64, 106, 107], so the thinning level for this work was set at 10^{-5}.

Iron nucleus-initiated showers are expected to have smaller shower-to-shower fluctuations than proton-initiated showers. Heuristically, it is anticipated that the 56 nucleons in the primary particle—each sharing the energy—will already

[2]Historically, protons and iron nuclei are considered as the light and heavy extremes, respectively, of the primary particles. Nothing heavier than iron is expected at any significant flux level because of iron?s position on the binding energy per nucleon curve and the common assumption that cosmic ray composition follows stellar abundances.

have nucleon-to-nucleon fluctuations equivalent to the fluctuations in 56 individual nucleon showers. A proton's primary, of course, is an individual nucleon. Studies with shower generators, including CORSIKA, have verified the suspicions and have shown that generating as few as 200 iron showers at a given energy is sufficient to study primary composition parameters, whereas 500 proton showers are needed [105]. More common numbers are 400 iron showers and 500 proton showers [64].

For this study, at least 400 iron showers and 500 proton showers were generated using each hadronic interaction model in each 0.1 step of log(E/eV) from E = $10^{17.5}$ to 10^{20} eV. Tables 4.1 and 4.2 summarize the number of showers for each model and primary species at each energy, including the mean X_{max}, and the variance of the mean. The CORSIKA version is also listed.

4.2 Fitting to the CORSIKA data

Having generated an extensive library of EAS with different primary energies and primary composition for each of two hadronic interaction models, the next question is whether or not the primary composition information can be recovered from the longitudinal profile of the EAS. A variety of potential composition-indication parameters will be discussed in Section 4.3, but each depends on some fit and parameterization of the data.

4.2.1 Gaisser-Hillas function

Recall the Gaisser-Hillas function (GH), 2.18 from Section 2.2.1

$$N(X) = N_{max}\left(\frac{X - X_\circ}{X_{max} - X_\circ}\right)^{(X_{max}-X_\circ)/\lambda} exp\left[\frac{(X_{max} - X)}{\lambda}\right] \qquad (2.18)$$

which can be fit to a shower profile to find N_{max}, X_{max}, $X_\circ$, and λ. X_{max} is related to changes in the composition by 2.11

$$\alpha = \frac{d\langle X_{max}\rangle}{d\log(E_\circ)} = K\lambda\left[1 - \frac{d\log(\langle A\rangle)}{d\log(E_\circ)}\right] \qquad (2.11)$$

Table 4.1. CORSIKA showers using QGSJet. X_{max} is in gm/cm^2, and the uncertainties are the variance of the mean. Showers for log(E/eV) >= 18.0 were produced with CORSIKA Version 6.005, and those with log(E/eV) <= 17.9 used Version 6.010.

	Protons		Iron	
log(E/eV)	Number	Mean X_{max}	Number	Mean X_{max}
17.5	500	706.2 ± 3.2	400	601.4 ± 1.3
17.6	500	702.3 ± 3.2	400	607.5 ± 1.2
17.7	500	712.3 ± 3.0	400	613.8 ± 1.2
17.8	500	709.2 ± 3.0	400	619.2 ± 1.3
17.9	500	717.4 ± 3.1	400	625.6 ± 1.2
18.0	872	727.1 ± 2.2	858	631.6 ± 0.8
18.1	989	728.9 ± 2.0	996	637.1 ± 0.8
18.2	851	737.1 ± 2.4	931	642.4 ± 0.7
18.3	544	736.2 ± 2.7	553	650.7 ± 0.9
18.4	500	748.0 ± 3.0	523	655.0 ± 0.9
18.5	522	753.0 ± 3.1	518	662.6 ± 0.9
18.6	511	759.2 ± 3.0	510	667.4 ± 1.0
18.7	522	762.1 ± 2.9	509	673.7 ± 0.9
18.8	502	766.5 ± 2.8	523	681.4 ± 0.9
18.9	508	769.2 ± 2.8	501	686.7 ± 1.0
19.0	612	776.6 ± 2.7	727	693.1 ± 0.8
19.1	525	781.9 ± 2.6	508	698.2 ± 0.9
19.2	516	789.4 ± 2.8	538	706.2 ± 0.9
19.3	522	788.2 ± 2.7	519	712.4 ± 1.0
19.4	519	796.2 ± 2.9	509	717.9 ± 0.9
19.5	547	794.5 ± 2.7	471	722.9 ± 0.9
19.6	515	801.9 ± 2.7	504	728.7 ± 0.9
19.7	508	812.2 ± 2.8	500	735.9 ± 0.9
19.8	515	818.2 ± 2.8	506	739.7 ± 0.9
19.9	507	819.9 ± 2.7	468	746.5 ± 1.0
20.0	588	825.4 ± 2.5	414	753.5 ± 1.0

Table 4.2. CORSIKA showers using SIBYLL. X_{max} is in gm/cm^2, and the uncertainties are the variance of the mean. All SIBYLL showers were generated with CORSIKA 6.010.

	Protons		Iron	
log(E/eV)	Number	Mean X_{max}	Number	Mean X_{max}
17.5	500	714.4 ± 2.9	400	613.3 ± 1.3
17.6	500	713.3 ± 2.5	400	619.8 ± 1.4
17.7	500	722.6 ± 2.8	400	625.4 ± 1.3
17.8	500	731.5 ± 2.7	400	630.0 ± 1.2
17.9	500	736.9 ± 2.6	400	635.4 ± 1.2
18.0	600	741.6 ± 2.2	400	640.9 ± 1.2
18.1	600	749.1 ± 2.5	400	645.7 ± 1.2
18.2	600	749.9 ± 2.4	400	655.6 ± 1.2
18.3	545	760.4 ± 2.5	405	658.4 ± 1.1
18.4	520	767.1 ± 2.7	400	664.7 ± 1.2
18.5	588	769.1 ± 2.4	400	669.5 ± 1.1
18.6	600	775.7 ± 2.4	400	675.5 ± 1.1
18.7	574	779.8 ± 2.3	400	681.4 ± 1.1
18.8	589	785.4 ± 2.2	414	686.2 ± 1.1
18.9	520	795.6 ± 2.6	419	694.3 ± 1.1
19.0	553	800.0 ± 2.4	404	698.6 ± 1.2
19.1	512	810.7 ± 2.5	419	705.1 ± 1.1
19.2	501	814.8 ± 2.7	400	709.1 ± 1.1
19.3	506	815.8 ± 2.4	428	715.4 ± 1.0
19.4	658	822.6 ± 2.2	419	723.0 ± 1.1
19.5	514	828.0 ± 2.3	405	727.7 ± 1.0
19.6	562	835.6 ± 2.2	569	734.8 ± 0.9
19.7	500	843.0 ± 2.4	402	739.9 ± 1.0
19.8	786	848.1 ± 1.9	416	744.7 ± 0.9
19.9	500	850.8 ± 2.3	422	750.0 ± 1.0
20.0	542	861.1 ± 2.3	413	756.4 ± 1.0

where α is the ER (see Section 2.1.3). $X_\circ$, once considered the depth of first interaction, is now treated as a fitting parameter which has been shown to have no correlation to the composition of the primary [34, 66, 107]. In the simple branching model of Section 2.1.2, λ was the characteristic length of the branching process, which would be related to the cross-sections of the interacting particles. In reality, λ represents all of the cross-section information for all of the interactions and may show some correlation with the composition of the primary UHECR.

4.2.2 Gaussian-in-Age

As in Eq. (2.16), it is often convenient to define the EAS "age" s as

$$s = \frac{3X}{X + 2X_{max}} \tag{2.16}$$

In this parameterization, s = 0 at the top of the atmosphere, s = 1 at the shower maximum, and s = 3 at infinite atmospheric depth. The effective extent of the shower is from s = 0 to s = 2, and for showers in the $E_\circ = 10^{17}$ eV to 10^{18} eV range, the profile is well-described by a Gaussian centered at s = 1 [108].

For computational simplicity, the Gaussian-in-Age function (GIA) can be written in terms of the familiar atmospheric depth X and the depth of shower maximum X_{max} as

$$N(X) = N_{max} \exp\left[-\frac{2}{\sigma^2}\left(\frac{X - X_{max}}{X + 2X_{max}}\right)^2\right] \tag{4.1}$$

where σ is a parameter describing the width of the Gaussian [108]. Included in σ is the information about the shower development (similar to λ in the Gaisser-Hillas parameterization), so σ possibly reveals information about the composition of the primary cosmic ray.

An attractive feature of the Gaussian-in-Age parameterization is its exploitation of the symmetry of the shower profile to find X_{max}. Even though s does not appear

in Eq. (4.1), the shape of Eq. (4.1) is symmetric about s = 1, so there is a reasonable expectation that a fit of Eq. (4.1) to a shower profile will properly find X_{max}.

4.2.3 Fitting to the CORSIKA output

The CORSIKA output is conveniently listed in tabular form, sampling the longitudinal shower development every 7 gm/cm^2 of atmospheric depth. The first step in determining which shower parameterizations will be useful in the determination of primary composition is to study this full description of the shower without the effects of propagation through the atmosphere, dusty mirrors, filters, PMT quantum efficiencies, and electronics response. If correlations between λ in GH (or σ in GIA) and UHECR composition cannot be found directly from the CORSIKA output, no confidence can be placed in those parameters after all the pieces of the air fluorescence technique have come into play. The rest of this section will discuss studies of the CORSIKA output.

Because ER is expected to be one of the strongest indications of changes in UHECR composition, an easy and reliable method for determining X_{max} is essential. With the entire shower profile available, it is tempting to merely find the bin with the largest number of charged particles and call it X_{max}. Figure 4.3 shows that because of fluctuations which are enhanced by the use of thinning, such a naïve method will often yield a significantly incorrect result. In the upper-left part of Figure 4.3, the bin with the largest number of charged particles is at 813 gm/cm^2, but features near the peak make determination of the true X_{max} difficult. In the upper-right box of Figure 4.3, the number of charged particles has been adjusted as a weighted average of that bin and its three nearest neighbors. The bin itself has a weight of 4, the adjacent neighbors a weight of 3, the next neighbors a weight of 2, etc. The bin with the most charged particles is now at 862 gm/cm^2,

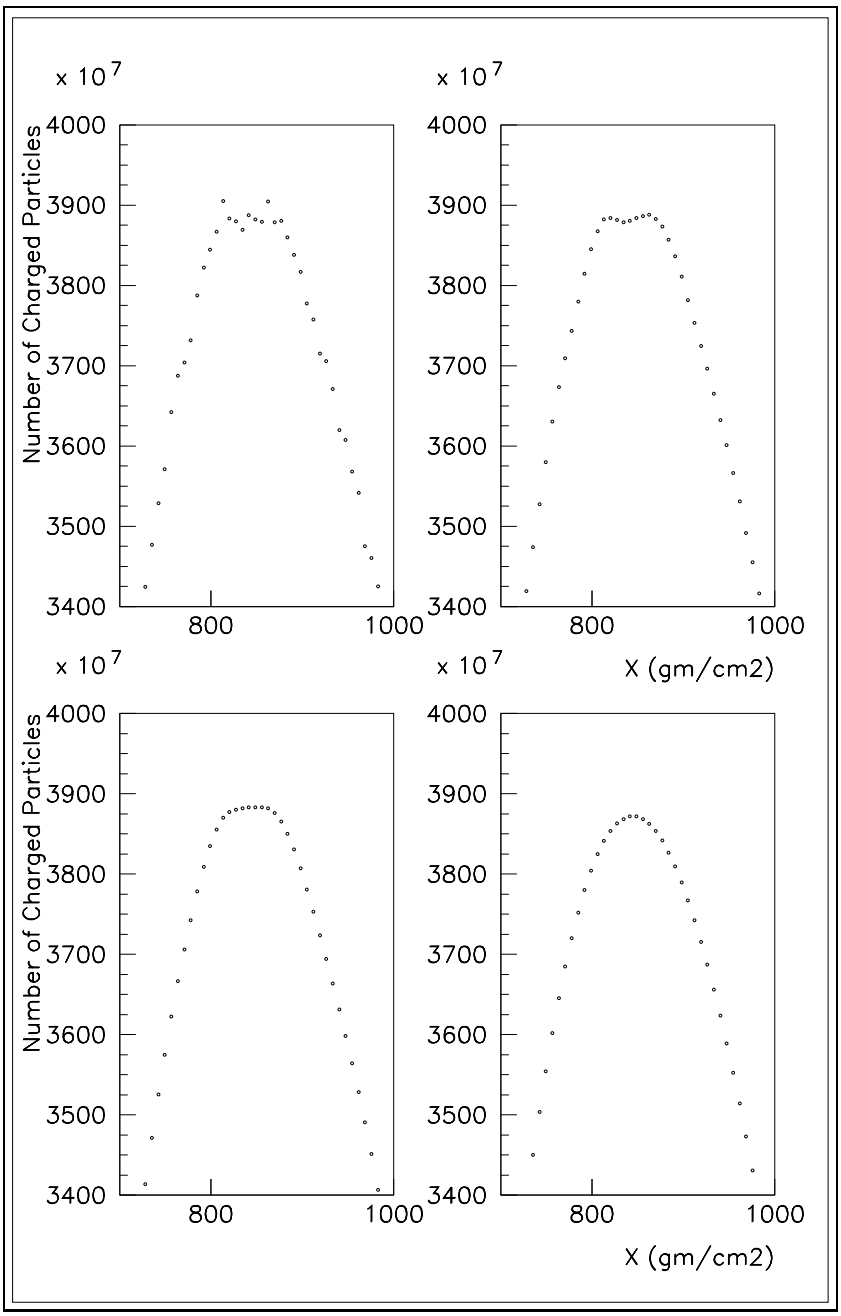

Figure 4.3. Effects of smoothing CORSIKA output on finding X_{max}. Upper-left: No smoothing; Upper-right: Three-neighbor smoothing; Lower-left: Five-neighbor smoothing; Lower-right: Ten-neighbor smoothing. Only the portion of the shower near X_{max} is shown to display the effect more clearly.

but there is still not a peak to the distribution. The smoothing routine is extended to five neighbors on each side in the lower-left box of Figure 4.3, and finally in the lower-right box of Figure 4.3, with the smoothing extended ten bins on each side, the profile is smooth enough to give confidence in X_{max}. The X_{max} values used to obtain the mean X_{max} listed in Tables 4.1 and 4.2 were obtained using the weighted-average smoothing process.

Inspection of Figure 4.3 shows that the weighted-average smoothing process has pulled down N_{max}, which will affect any reconstructed energy. However, for this library of CORSIKA-generated showers, the energy of the primary particle is known from the input. For this study of parameterization of the CORSIKA output, the input energy can be used, and for the purpose of determining the ER of the two hadronic interaction models for protons and iron, the weighted-average smoothing gives the true X_{max}.

For the fitting of GH and GIA to the CORSIKA output, χ^2 optimization was used. For both functions, the χ^2 is defined as

$$\chi^2 = \sum_{bins} \frac{(ncp_{CORSKIA} - ncp_{fit})^2}{ncp_{CORSIKA}} \tag{4.2}$$

where ncp is the number of charged particles, the bins are the 7 gm/cm^2 atmospheric depth bins, and the uncertainty in each bin is assumed to be the square root of the number of particles in the bin.

For GH fits, X_{max} was fixed at the value known from the weighted-average smoothing. The $X_\circ$ and λ ranges were chosen based on previous studies [66]. $X_\circ$ was varied from -200 gm/cm^2 to the depth of the first CORSIKA output bin with more than one charged particle (which is within 7 gm/cm^2 of the depth of first interaction, X_1) in 5 gm/cm^2 steps. In steps of 1 gm/cm^2, λ was varied from 60 to 80 gm/cm^2. N_{max} was allowed to vary in 1% steps from 90% to 110% of the highest number of charged particles in the CORSIKA output (which was not necessarily at

X_{max}, but was the highest value of N before the weighted-average smoothing pulled down N_{max}).

For GIA fits, X_{max} and N_{max} were treated as described above for the GH fits. The range for σ was chosen to be 0.180 to 0.220 in steps of 0.001 based on previous studies [107].

For both fits, the parameters were varied over the entire phase space described above, and the global minimum χ^2 was determined. Figure 4.4 shows the longitudinal profile of a representative CORSIKA shower and the resulting best fits for both GH and GIA. The behavior of GH having a too low N_{max} and GIA having a too high N_{max} with a cross-over somewhere near the half-maximum was typical. Additionally, the average χ^2 per degree of freedom for both functions was far from one.

The poor quality of the fits to the CORSIKA output is attributable to the accentuation of the fluctuations introduced by the use of thinning. A correct χ^2 depends on the proper determination of the uncertainties in the denominator of Eq. (4.2). The correct χ^2 for fitting the shower generated utilizing thinning is

$$\chi^2 = \sum_{bins} \frac{\left(\sum_{i=1}^{\#particles} ncp_i w_i - ncp_{fit}\right)^2}{\sum_{i=1}^{\#particles} ncp_i w_i} \tag{4.3}$$

where ncp_i now represents only the particles actually tracked. Particles above the thinning threshold would have weight w_i of one, and those below the threshold would have the weight as assigned by CORSIKA. The w_i are recorded in one of the CORSIKA output files every time an interaction produces daughter particles below the threshold and thinning is induced, but the w_i are very difficult to recover bin-by-bin.

When thinning is utilized at UHECR energies, fits to CORSIKA shower using Eq. (4.2) are poor even in the best possible scenario where the added effects of the

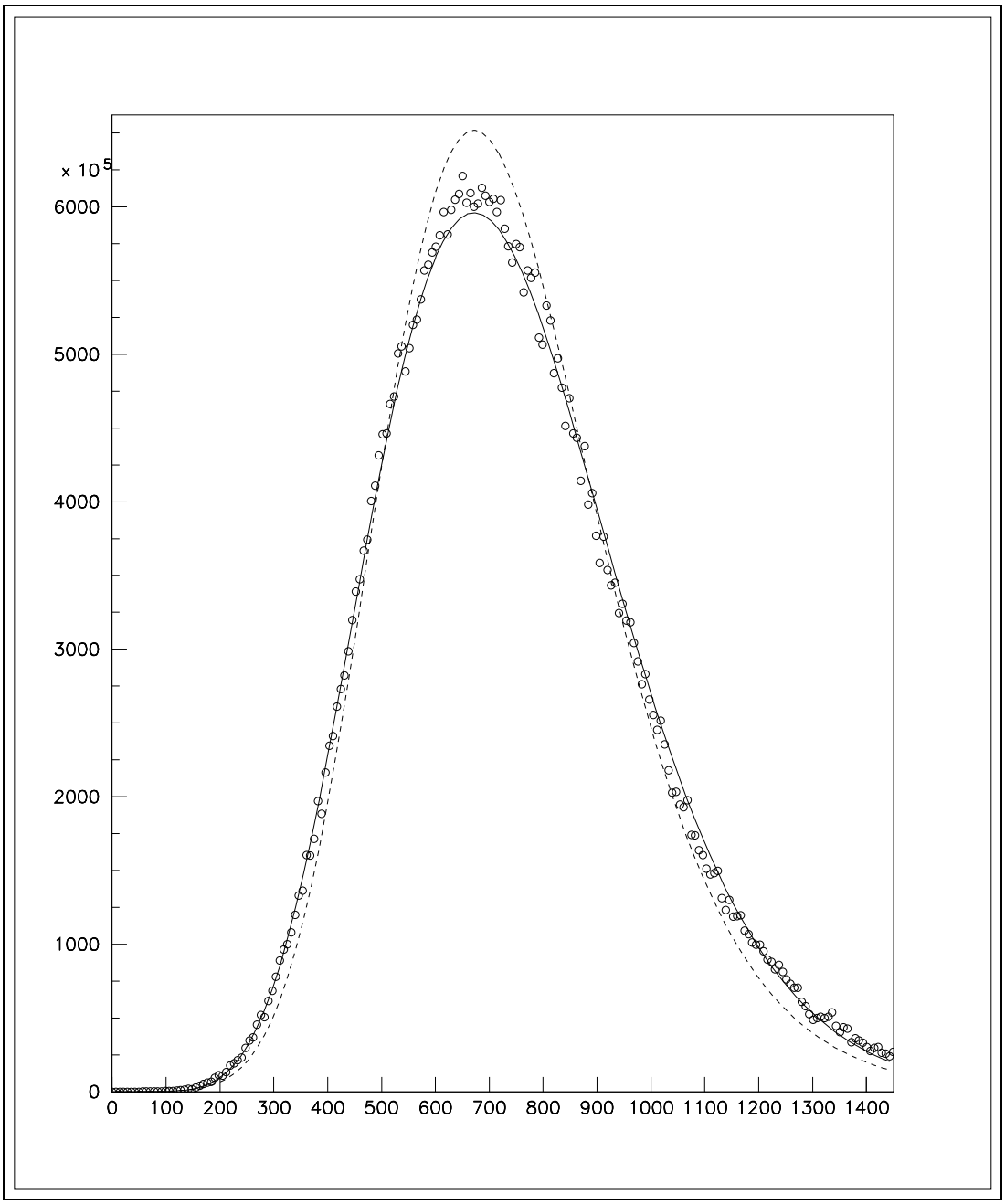

Figure 4.4. Typical poor fits to CORSIKA output. The dashed line is the Gaussian-in-Age fit, and the solid line is the Gaisser-Hillas fit.

atmosphere and detector are absent, and improving the fits by using Eq. (4.3) is prohibitively problematic. Consequently, conclusively showing the small correlations between composition and λ in GH or σ in GIA is difficult. Previous studies have shown that the correlation between λ and UHECR composition is weak [66, 107], and that λ can be set at 70 gm/cm^2 without affecting the ER measurement [34]. Similar studies have shown that the difference in σ for proton-initiated showers and iron-initiated showers is too small to make composition determinations [107]. Therefore, λ and σ were not used to infer composition information in this work.

Historically, results from shower-generation programs have been fit with GH or GIA functions and only the parameters of the fits have been saved in a shower library [109, 110]. When an atmospheric and detector Monte Carlo program (see Section 5.1) made a call to a shower generator, the library of parameters was sampled and the number of charged particles at a given atmospheric depth was computed from the appropriate function. Not only does functional shower generation make an a priori assumption about the shower shape, but at UHECR energies, the poor quality of GH and GIA fits to CORSIKA output makes such shower generation unattractive. For this work, shower generation in the Monte Carlo was accomplished by actually sampling a shower in the library described in Tables 4.1 and 4.2. For the desired primary particle energy and species and the specified hadronic interaction model, an appropriate shower in the library is identified. The actual number of charged particles at the atmospheric depth of interest directly from the CORSIKA output table is read into the Monte Carlo. More discussion of the use of the shower library in Monte Carlo resolution studies and the Inverse Monte Carlo portion of the event reconstruction will be presented in Chapter 5.

One more study can be made that does not rely on GH or GIA fits. The Full Width at Half Maximum (FWHM) of the longitudinal development is a candidate parameter. The FWHM for each of the showers in the library was determined

using the longitudinal profiles after weighted-average smoothing. After X_{max} was determined, the smoothed N_{max} was recorded. The depth of the bins with $N = N_{max}/2$ was found, and the FWHM is simply the difference of these depths.

Figure 4.5 shows the mean FWHM for showers generated with QGSJet at every 0.1 in log(E/eV) for E ranging from 10^{18} to 10^{20} eV. The separation between the two species is only about 2%, and this is before the information from the shower propagates through the atmosphere and the detector. FWHM is not a promising indicator of primary UHECR composition.

4.3 Measurable Parameters

Clearly the best parameter for measuring a change in UHECR composition is X_{max} and especially the ER as was anticipated in Section 2.1.3. Figure 4.6 shows the ER for protons and iron for both QGSJet and SIBYLL. The X_{max} of each shower represented in Tables 4.1 and 4.2 was found using the smoothing routine described in Section 4.2.3. The mean X_{max} in each energy bin is used, and the errors shown are the variance of the mean. For this experiment with a small sample size, the argument can be made that the most likely value is more meaningful than the mean value, however the mean value has become the standard in UHECR physics. For comparison with other studies [64, 105] and other experimental results [39, 40], mean X_{max} is used throughout this work.

One more use of X_{max} data may yield insight into the composition of the primary particles. As explained in Section 4.1.4, protons are expected to show more shower-to-shower fluctuation than iron nuclei. Indeed, Figure 4.7 shows that at each of the three energies shown, both QGSJet and SIBYLL predict the distribution of X_{max} is wider for proton showers than for iron showers. If the composition is changing from ferric to protonic as energy increases, then the X_{max} distribution at lower energies will be narrower than at higher energies.

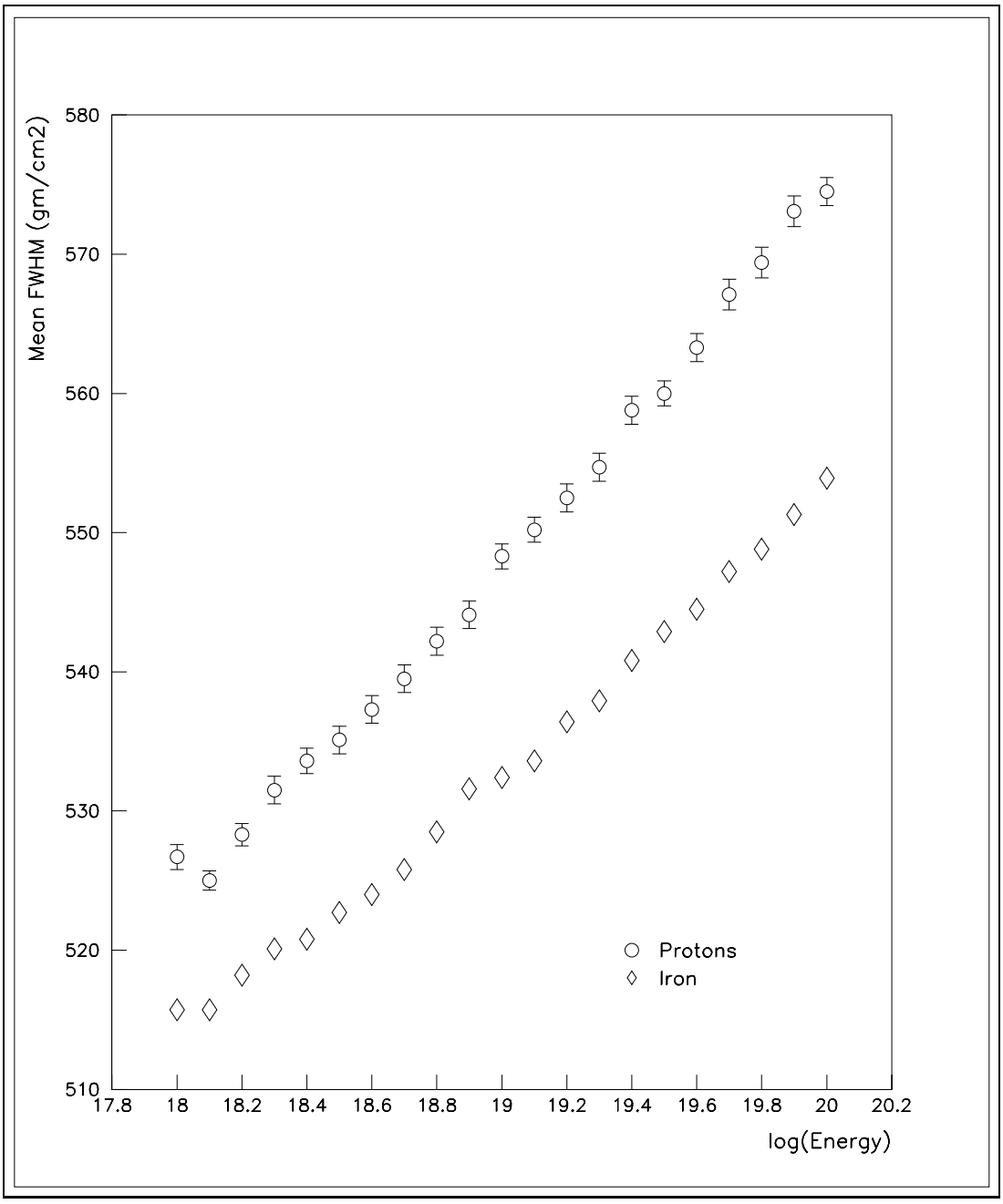

Figure 4.5. FWHM study.

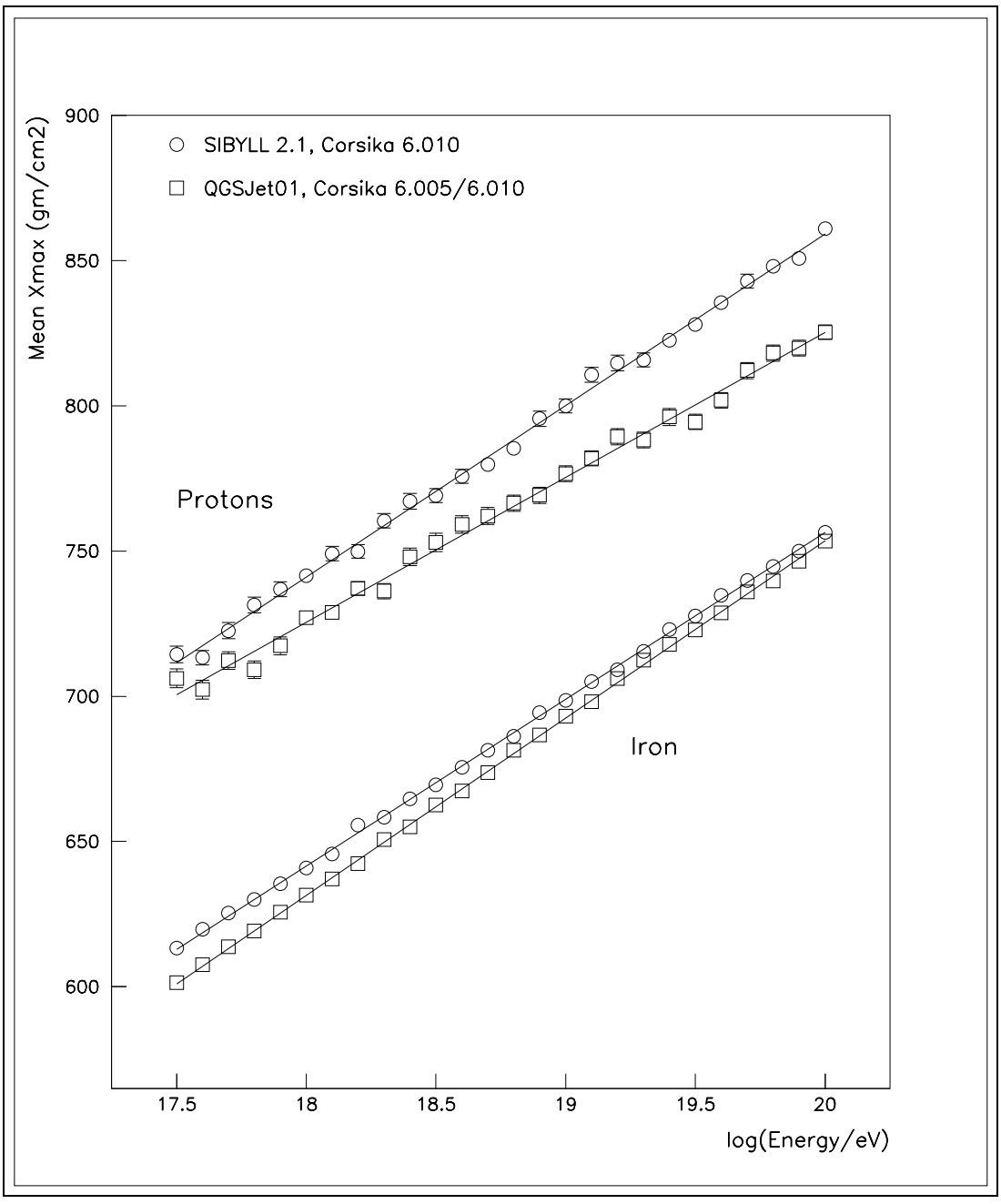

Figure 4.6. Elongation rates from CORSIKA. The error bars are the variance of the mean.

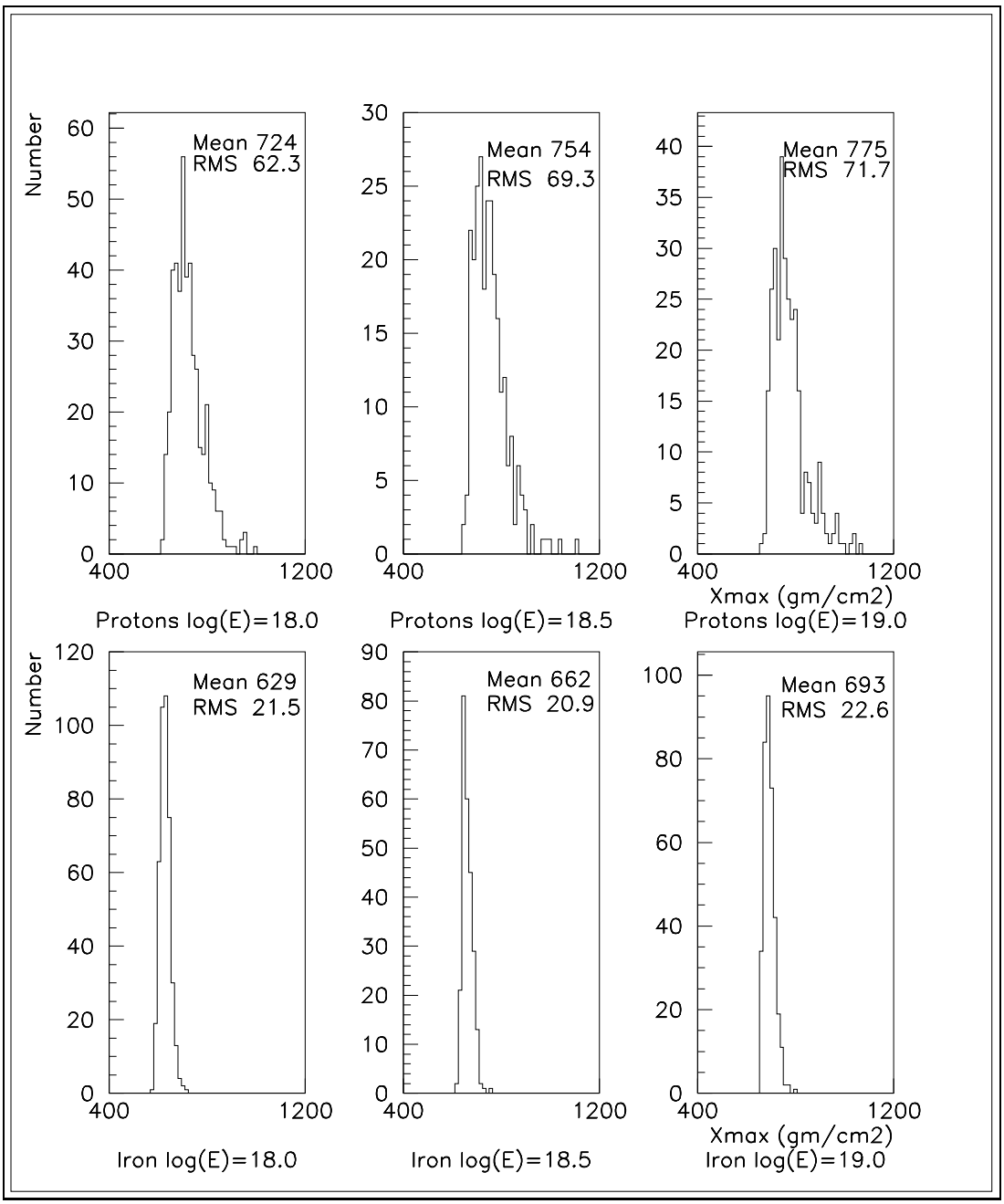

Figure 4.7. X_{max} distributions from CORSIKA. At each energy, the iron distribution is much narrower than the proton distribution. As energy increases, a widening (narrowing) of the distributions in the data indicates the composition is becoming lighter (heavier).

On the other hand, the composition may not be changing rapidly enough for the above method to be useful. In that case, instead of looking at the X_{max} distribution within narrow energy bins, one could consider the X_{max} distribution over the entire energy range of the experiment. Figure 4.8 shows the X_{max} distributions expected from a purely light or a purely heavy flux with an E^{-3} spectrum. For both hadronic interaction models, the difference between iron nuclei and protons is clear even with this large energy range.

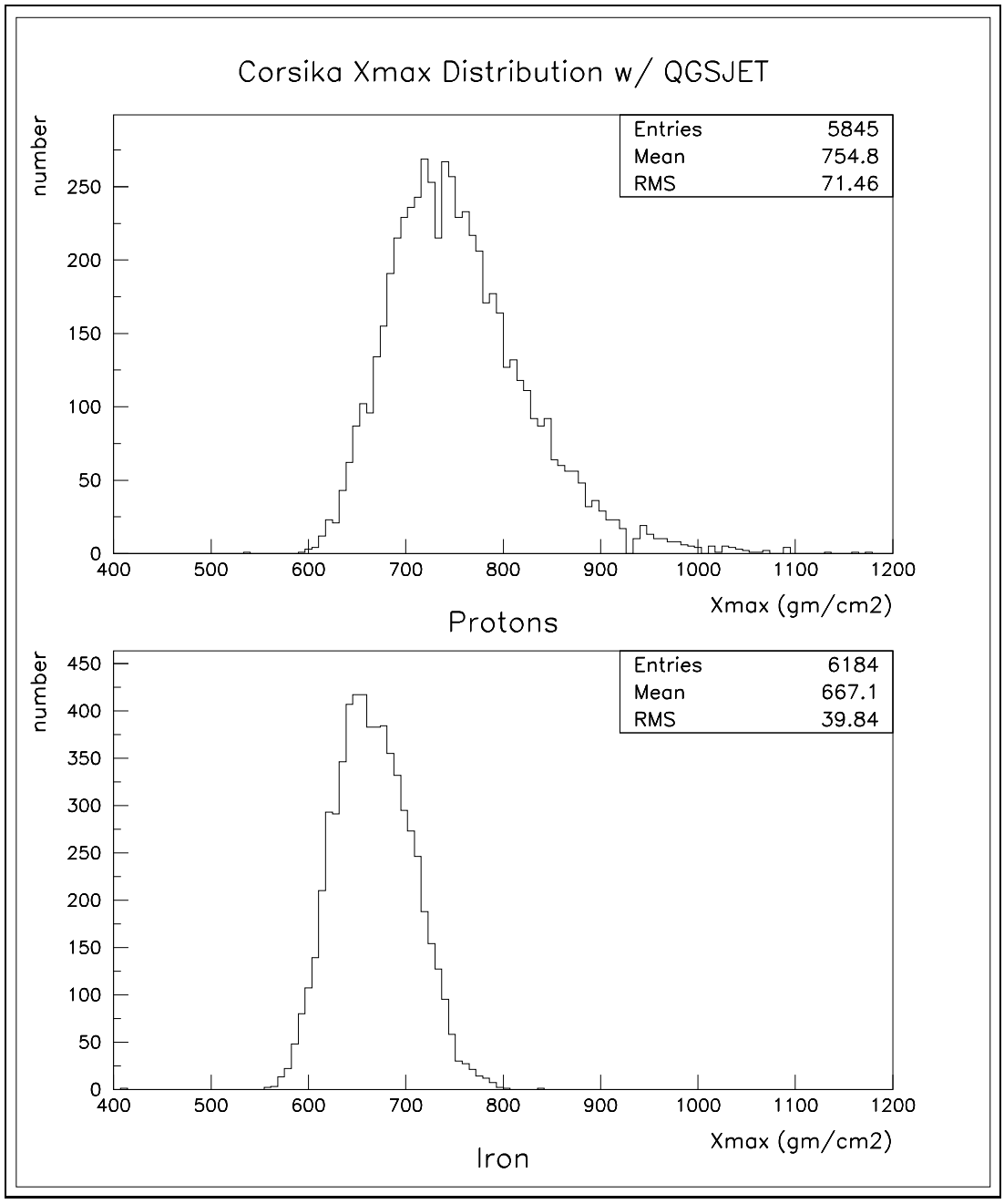

Figure 4.8. X_{max} distributions from CORSIKA for all UHECR energies.

CHAPTER 5

RECONSTRUCTION AND RESOLUTION

Once an EAS was observed by the detector, the arrival direction, energy, and composition of the incident cosmic ray were reconstructed. A detailed Monte Carlo model of light production, atmospheric transmission, and detector response was developed in conjunction with the reconstruction routines, allowing the study of the reconstruction codes ability to correctly recover information about the primary particle.

5.1 Monte Carlo

The full Monte Carlo simulation of a cosmic ray event begins with the generation of an EAS. Although a brief description follows, the reader is referred to [66] and [76]. As explained in Sections 4.1.4 and 4.2.3, the longitudinal development of each CORSIKA shower used in obtaining the elongation rates of Figure 4.6 and the distributions of Figures 4.7 and 4.8 was stored in the library described in Tables 4.1 and 4.2 for use in the Monte Carlo. The library contains the number of charged particles every ≈ 7 gm/cm^2 of atmospheric depth X. After appropriately selecting a primary particle energy from the input spectrum, which, for this work, was the Fly's Eye Stereo Spectrum, the Monte Carlo randomly selects a shower from the library energy bin closest to the desired energy. Because the shower library was generated at discrete energies in steps of 0.1 in log(E), the desired energy may not

exactly match the library showers energy, so the number of charged particles in each X bin is scaled linearly by the ratio of desired energy to library energy.[1] The Monte Carlo throws the shower at a zenith angle chosen from the zenith angle distribution of the Fly's Eye Stereo data. In each atmospheric depth bin, scintillation light and Čerenkov light are calculated based on the number of charged particles in that bin. The propagation of the light is simulated accounting for molecular and aerosol scattering (see Section 3.3) and ozone absorption. The scale height and horizontal attenuation length of the aerosol distribution are specified by the user, with default values of 1 km and 25 km, respectively.

The photon flux reaching the detector is distributed among the PMTs by a detailed ray-tracing program which was developed with ray optics and has been checked by surveys of stars in the night sky [111, 112]. The ray tracing accounts for PMT cluster obscuration of the mirror, mirror shape, and UV filter transmission. Cracks between PMTs are simulated. Mirror reflectivity is assumed to be 80% of the reflectivity measured immediately after the mirrors are cleaned. A PMT quantum efficiency of 28% is used, based on specifications provided by the manufacturers, to obtain the number of photo-electrons (pe).

Once a Monte Carlo photo-electron is generated, the gain of the PMT and its preamplifier is simulated, generating a simulated QDC or FADC signal as described in Sections 3.1.1 and 3.1.2. The triggering conditions described in those sections are applied, with the resulting output stored in the same format as real data. The full timing of each Monte Carlo photon, from production at the shower to the PMT face, is stored so that the trigger timing in the output is accurate.

[1] Studies by Reil have shown that over these small intervals in energy, the linear relationship between primary particle energy and number of charged particles in each bin holds extremely well [76].

The Monte Carlo also simulates noise. Tube response noise and electronics noise are added to each signal following a Poissonian distribution, and random noise tubes are added to each event.

5.2 Reconstruction

Because the Monte Carlo output is in the same format as the data, the same reconstruction routines can be and are used on both. The early steps of the data processing are long-established and well-documented [67, 76]. First the raw data are calibrated using the information described in Section 3.2. The relative timing information from each mirror is next converted to an absolute time as determined by GPS [69]. The individual mirror triggers are matched to form multiple-mirror events, and the multiple-mirror events from each site are time-matched to build stereo events.

Most of the stereo events are not cosmic rays, but are the flashers and lasers described in Section 3.3. These known sources are removed from the data stream based on their geometry and timing [76] and are analyzed separately to obtain information about the atmosphere. Specifically, the steerable lasers are fired at assigned fractions of the GPS second, making them easily recognized in the data stream.

Even after off-line time matching, some stereo events are noise. To separate noise events from track-like events, a Rayleigh filter is employed [107]. Figure 5.1 illustrates how the Rayleigh vector $\vec{r}$ is formed. A unit step is taken between each triggered tube which has an adjacent triggered tube in the direction of the tube triggering order. The sum of all steps gives the magnitude of $\vec{r}$. After n steps,

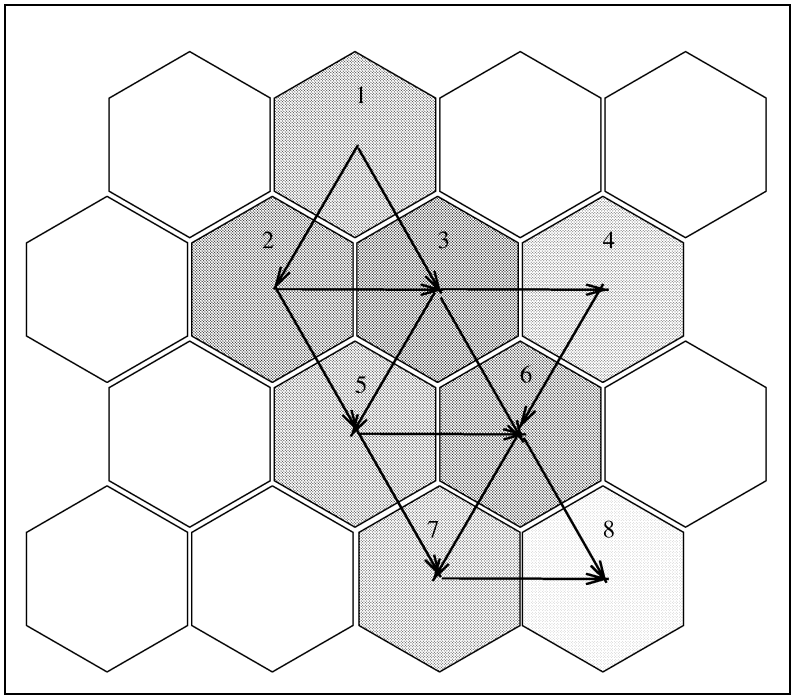

Figure 5.1. Constructing the Rayleigh vector. Adapted from [107].

the probability P that $\vec{r}$ is larger than the vector $\vec{R}$ that would be formed by a two-dimensional random walk is

$$P(r > R) = e^{-R^2/n} \tag{5.1}$$

The probability that an event was created by random noise is required to be less than 0.1%. Additionally, if no adjacent pairs of triggering tubes can be found, which is to say, r cannot be formed as described, the event is rejected as noise.

Because $\vec{r}$ is built in the order of tube firings, the direction of $\vec{r}$ gives an indication of whether the event was downward-going as expected for cosmic rays. Any event within 20° of horizontal is discarded because it is likely the ISF or one of the steerable lasers [76].

5.2.1 Geometry

The line of the EAS and the point of the detector uniquely define the Shower-Detector Plane (SDP), as illustrated in Figure 5.2. The location of each camera and the pointing direction of each PMT cluster have been measured [111, 112, 113], so the pointing direction ni of each PMT is known. With the signal in pe S_i in each of the N tubes in the event known, the amplitude-weighted normal $\hat{n}_{SDP}$ of the SDP is found by minimizing the χ^2

$$\chi^2_{SDP} = \sum_{i=1}^{N} \frac{(n_{SDP} \cdot n_i) S_i}{\sigma_i^2} \tag{5.2}$$

where σ^2 is the error in each tube signal given by

$$\sigma_i^2 = \frac{S_i + S_{noise}}{S_i} \tag{5.3}$$

and $S_{noise} = 40$ pe/μsec/tube from both sky noise and electronics noise [107, 111].

Eq. (5.2) is minimized using all tubes in the event, and tubes more than three degrees off the SDP are tagged as bad. Successive iterations of Eq. (5.2) are performed until the set of good tubes is stable. If fewer than three tubes are still considered good after the plane fit, the event is discarded.

Once the SDP is known for each site, the intersection of the planes gives the direction and location of the EAS. With the geometry of the EAS known, the next step in the reconstruction is to fit the data to the Gaisser-Hillas profile described in Eq. (2.18). The light arrives at the detector and is collected in discrete PMTs, each of which covers about $1^\circ \times 1^\circ$ of the sky. The signal from a segment of the EAS is necessarily split among many PMTs. For profile fitting, the signal must be re-combined into bins which correspond to the segments of the EAS. The most complete profile fit would use both the time and geometry information of the signal. For this analysis, the two types of information are used in separate but complementary ways.

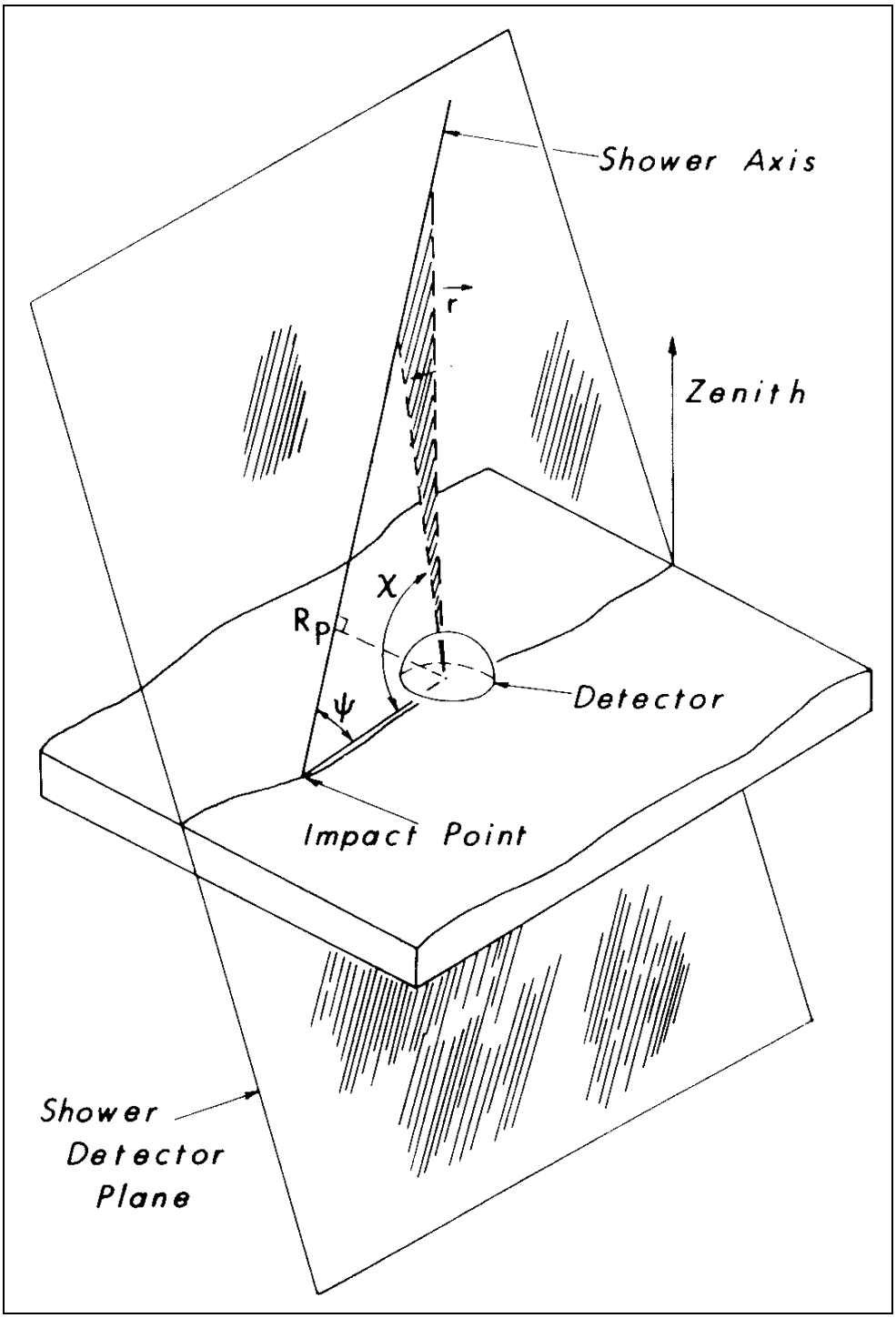

Figure 5.2. The shower-detector plane. The point of the detector and the line of the shower define a plane. The geometric parameters R_p and ψ are defined as shown.

5.2.2 Angular Binning

The angular binning technique discussed in this section was developed by Kevin Reil, and an excellent description can be found in his thesis [76]. Once the signal at the detector is known, the track is divided into angular bins along the direction of the track and the light flux Φ arriving at the camera in each angular bin is computed by

$$\Phi_i = \sum_{j=1}^{n_i} N_{pe_i} \times C_{A_{eff_i}} \tag{5.4}$$

where n_i is the number of tubes in the bin and

$$C_{A_{eff}} = \frac{1}{A_{eff}}. \tag{5.5}$$

The effective area of each PMT, A_{eff}, is computed from the same ray tracing table used in the Monte Carlo, accounting for cluster obscuration, PMT arrangement, gaps between PMTs, spot size, and spot position on the PMT. However, in the Monte Carlo each photon is traced individually from its creation to the detector, while in the reconstruction the photon flux is being calculated from the number of photo electrons per degree per square meter, N_{pe}. As a result, the reconstruction ray tracing uses an average of millions of incoming photons and lacks some asymmetry effects. A_{eff} also depends on how far off-plane the triggered tube is.

With the flux in each bin known, an "inverse Monte Carlo" method is employed wherein the reconstruction routine calls the Monte Carlo to generate a shower. Instead of using the shower library as described in Section 5.1, a Monte Carlo shower is generated with a Gaisser-Hillas profile per

$$N(X) = N_{max}\left(\frac{X - X_\circ}{X_{max} - X_\circ}\right)^{(X_{max}-X_\circ)/\lambda} \exp\left[\frac{(X_{max} - X)}{\lambda}\right]. \tag{2.18}$$

Historically, the Gaisser-Hillas profile has descrbied air fluorescence data very well. The shortcomings of fitting with 2.18 discussed in Section 4.2.3 were an artificial result of the enhanced flucuations introduced by the use of thinning in CORSIKA.

When a CORSIKA shower is used as part of the Monte Carlo, the enhancement is effectively washed out by the size of the Monte Carlo's sampling bins, the propagation of the resulting photons through the atmosphere, and the propagation of the signal through the PMTs and the electronics.

X_1 is set to zero, and λ is set to 70 gm/cm^2. Each photon, including both scintillation photons and Čerenkov photons, is individually traced up to the same point where the flux Φ was computed from the data, giving Φ^{MC}. This trace uses the atmospheric model described in Sections 3.3 and 5.1. If measured values of horizontal attenuation length and scale height are available in the data base for the hour during which the event occurred, those measured values are used. Otherwise, the average values of 25 km and 1 km are used [88]. N_{max} and X_{max} are allowed to vary to minimize the χ^2

$$\chi^2_{MC} = \sum_{i=1}^{\#ofbins} \frac{(\Phi_i - \Phi_i^{MC})^2}{\sigma_i^2} \tag{5.6}$$

For this χ^2, σ is given by

$$\sigma_i^2 = N_{pe_i}^2 \sigma^2_{C_{A_{eff_i}}} + \sigma^2_{N_{pe_i}} C_{A_{eff_i}} \tag{5.7}$$

and

$$\sigma^2_{N_{pe_i}} = N_{pe_i} + 40(pe/\mu sec). \tag{5.8}$$

For wide tracks, tubes far from the track center have very small A_{eff} and thus large $C_{A_{eff}}$. These tubes also tend to have a small N_{pe} with an associated large relative uncertainty in N_{pe}. Tubes with large $C_{A_{eff}}$ are therefore discarded from the fit. Considering only the surviving tubes, tracks less than six degrees long in either detector were cut because they cannot be accurately reconstructed.

Eq. (5.6) can be minimized for HiRes-1 and HiRes-2 individually, or for both sites globally. The N_{max} and X_{max} that minimize Eq. (5.6) (along with the defined X_1 and λ) define the shower profile. The total number of charged particles is obtained

from the integral of Eq. (2.18), and the energy is calculated by multiplying the total number of charged particles by the well-known energy deposited per charged particle.

5.2.3 Time Binning

Sections 5.2.1 and 5.2.2 describe typical "stereo" reconstruction. With two sites, the geometry is easily determined by the intersection of the SDP. Event timing information is mainly used to match events from both sites. When performing "monocular" reconstruction—i.e., reconstructing with data from only one site—finding the SDP does not change, but finding the geometry of the EAS within the SDP, specifically ψ and R_p in Figure 5.2, requires the use of the PMT timing information. Excellent discussions of monocular reconstruction can be found in [34, 66, 67, 107], which are all theses on HiRes-1 monocular results.

The HiRes team at Rutgers has developed a monocular reconstruction routine that takes advantage of the FADC timing at HiRes-2 [114, 115]. Instead of binning the signal by angle along the track, the signal is binned by time. For monocular reconstruction, the SDP is found in the same way as described for stereo reconstruction, except this method requires at least five good tubes. All possible ψ are then scanned to find the best ψ and R_p pair. For this work, the EAS geometry obtained from the intersection of the SDP is inserted into the time-binned reconstruction.

Once the SDP and EAS geometry within the SDP are known, a first estimate of the number of charged particles at the EAS in each time bin is calculated assuming all of the photons reaching the detector are from scintillation. The calculations include the same kinds of ray tracing considerations as the angular binning, but use a different ray tracing table. The standard horizontal attenuation length and scale height atmospheric model is used, but every event for this work is reconstructed with values of 25 km and 1 km, respectively.

The first guess of the number of charged particles at the shower obtained from the data is compared to the number of charged particles from a Gaisser-Hillas profile with $X_1 = 0$ gm/cm^2 and $\lambda = 70$ gm/cm^2. A scan through each X_{max} and its associated most likely N_{max} is performed to find the best fit. Čerenkov light is then introduced, based on the number of charged particles from the Gaisser-Hillas fit. The Čerenkov light is traced to the detector and subtracted from the signal, and the process is repeated to find the new X_{max} and N_{max}. The iterations continue until satisfactory agreement between the predicted data and real data is obtained. The energy of the event is calculated from the shower profile exactly as in the stereo technique.

Although the time binning method has been used with the S&H electronics at HiRes-1, for this work it was only used on the FADC data. The time-binned method was performed only on those events that survived the stereo reconstruction.

5.3 Resolution

For this study, nearly equal numbers of proton- and iron-initiated showers were created, with an equal number of SIBYLL and QGSJet showers for each species. Zenith angle was allowed to vary from 0 to 90, and core location varied through all azimuth such that the largest R_p was no more than 70 km. The thrown energy distribution followed the Fly's Eye Stereo Spectrum. The Monte Carlo events were processed by the stereo and time-binned reconstruction routines with the minimal cuts of probability that noise generated the event less than 0.1%, tracklength greater than 6 degrees at both sites, track direction greater than 20° above the horizon, and at least one stereo-reconstructed energy (HiRes-1 fit alone, HiRes-2 fit alone, or Hires-1/HiRes-2 global fit) greater than $10^{17.7}$ eV.

5.3.1 Atmospheric Comparisons

Real UHECR events occur in whatever atmospheric conditions present themselves in the aperture. However, if no measurement of those conditions exists in the database, the events are reconstructed with the average atmospheric description. The average paratmeters are a horizontal extinction lenght of 25 km and an aerosol scale height of 1 km, giving an optical depth of 0.04 $\pm$ 0.02 (stat) + 0.02 (sys). Studies show that optical depths less than 0.1 can be classified as "good" [88]. To mimic this situation, Monte Carlo events were generated with input atmospheric parameters sampled from the database and then reconstructed with the average parameters. Figure 5.3 shows the distribution of atmospheric parameters in the database, which is the distribution used for thrown events. Only horizontal extinction length and scale height pairs which gave an optical depth less than or equal to 0.1 were used, and only those pairs are represented in Figure 5.3. Inspection of Figure 5.3 reveals that the mean of the atmospheric parameters represented in the Figure do not match the quoted average atmospheric parameters. The quoted averages for optical depth and horizontal attenuation length are pulled to the right by measurements which give optical depths greater than 0.1 and are therefore not shown. The mean scale height is inferred from the mean horizontal attenuation length, the mean optical depth, and [88]

$$AOD = \frac{H_s}{L^a}. \tag{3.4}$$

Monte Carlo events were also generated with the average atmosphere parameters. Resolution studies using the two sets were indistinguishable, suggesting that the historically high uncertainty from atmospheric variation in air fluorescence experiments can be greatly reduced by a cut on measured optical depth.

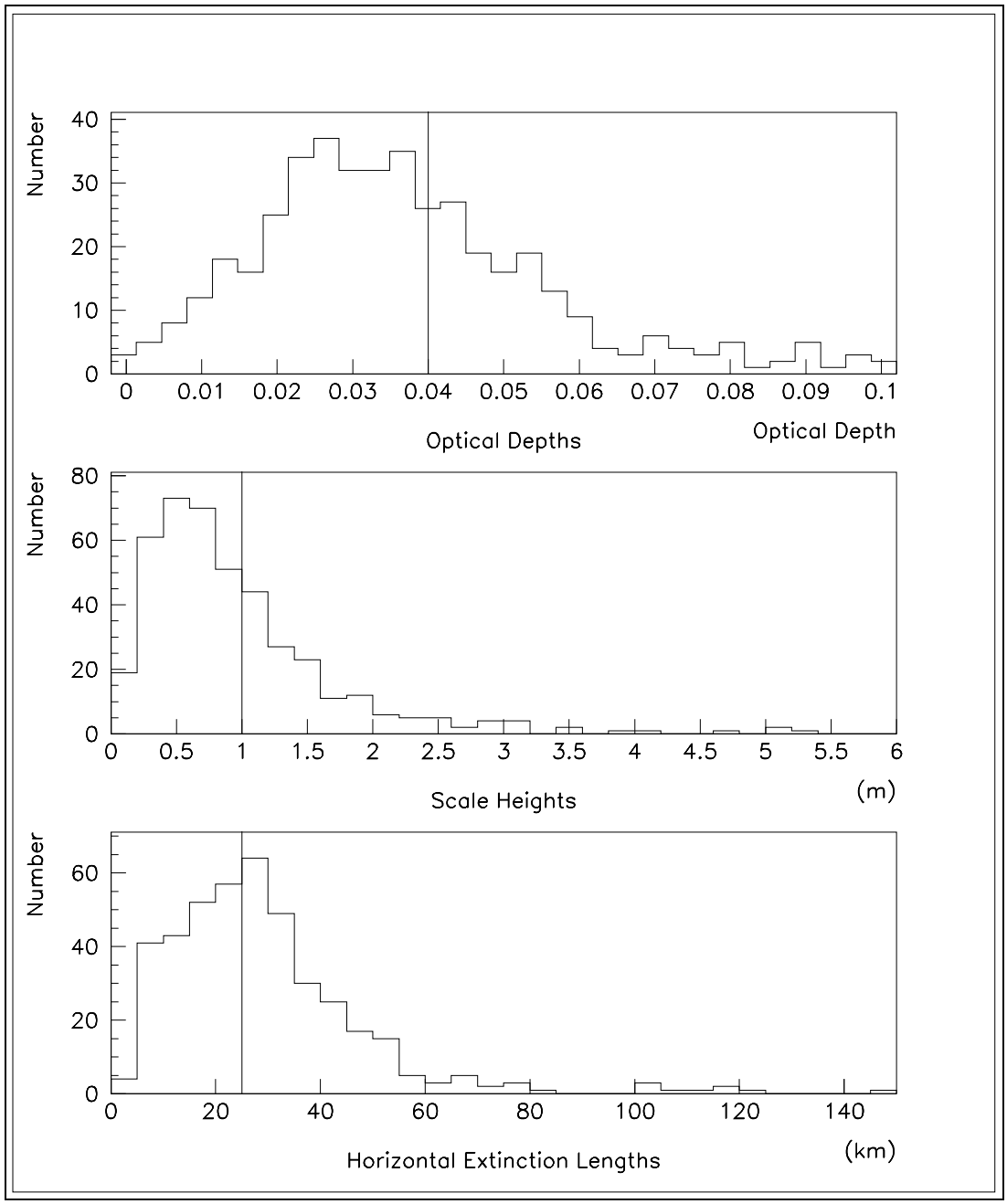

Figure 5.3. Distributions of atmospheric parameters. The vertical lines show the quoted average values.

5.3.2 Data-Monte Carlo Comparisons

If the Monte Carlo accurately models the detector, then the application of an event selection criterion will have the same effect on Monte Carlo events and data. The Monte Carlo can then be used to determine resolution by reconstructing Monte Carlo events and comparing the results to the input parameters. Additionally, the effects of selection cuts on the resolution can be studied. To determine how well the Monte Carlo models the detector, comparisons were made between over 20,000 Monte Carlo events and 926 UHECR events.

With no other cuts than those described in Section 5.3 applied, Figures 5.4–5.10 show the data-Monte Carlo comparisons for distributions in energy, zenith angle, ψ, R_p, tracklength in degrees and gm/cm^2, and maximum single N_{pe}/deg/m^2 in each event.

In each figure, the Monte Carlo histogram represents the results of reconstructing all 20,000+ Monte Carlo events, normalized to have the same area under the curve as the data histogram. The bin-by-bin ratios shown are ratios of the data bin height to the normalized Monte Carlo bin height.

5.3.3 Geometry Resolution

Obtaining a good profile fit is undermined by an incorrect geometry. The advantage of a stereo experiment is the ease with which the geometry of the EAS is obtained. Figures 5.11–5.13 show the resolution in determining the SDP, zenith angle, ψ, and R_p. In each of the plots, the Monte Carlo value is subtracted from the reconstructed value.

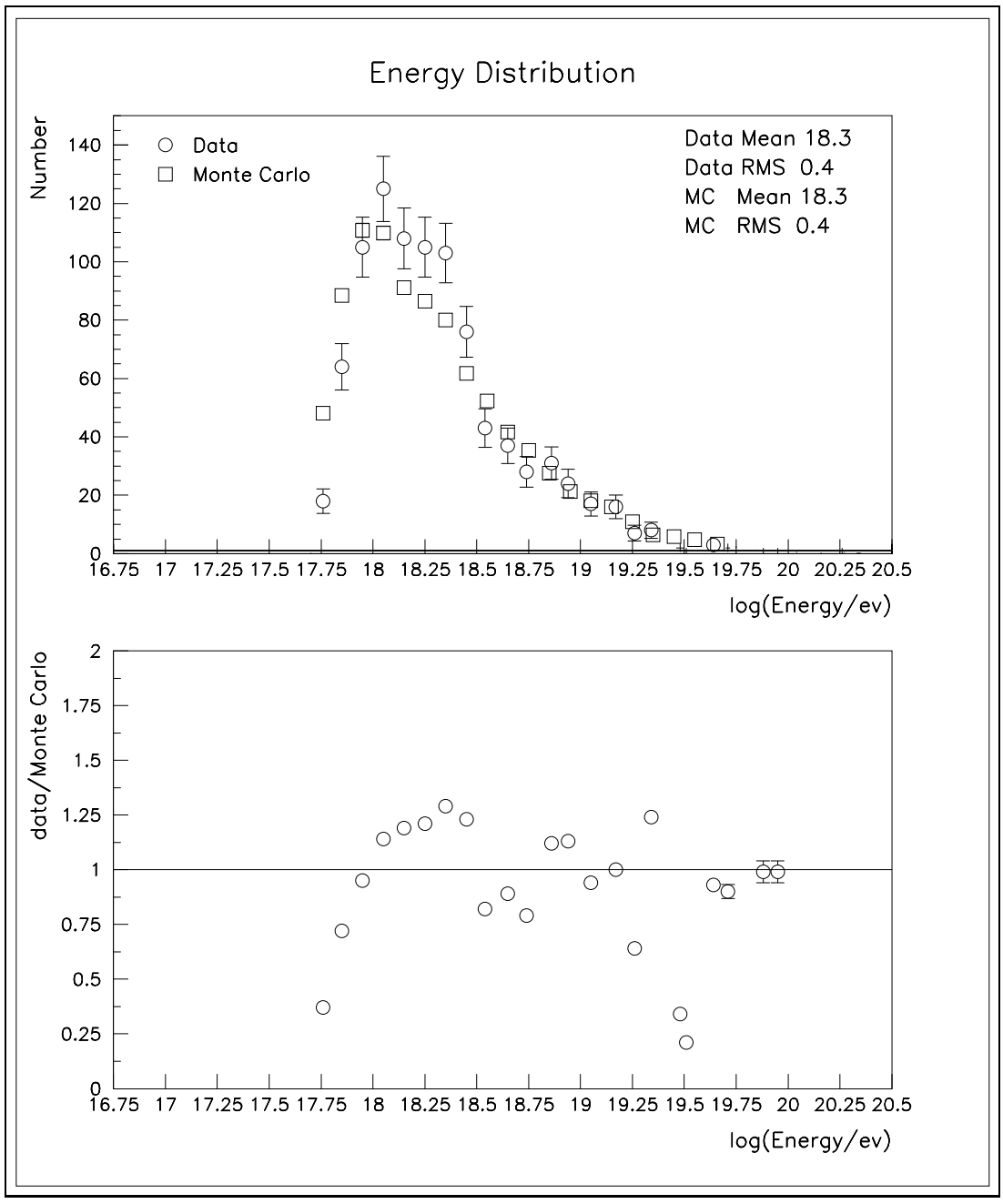

Figure 5.4. Data/Monte Carlo comparison—reconstructed energy.

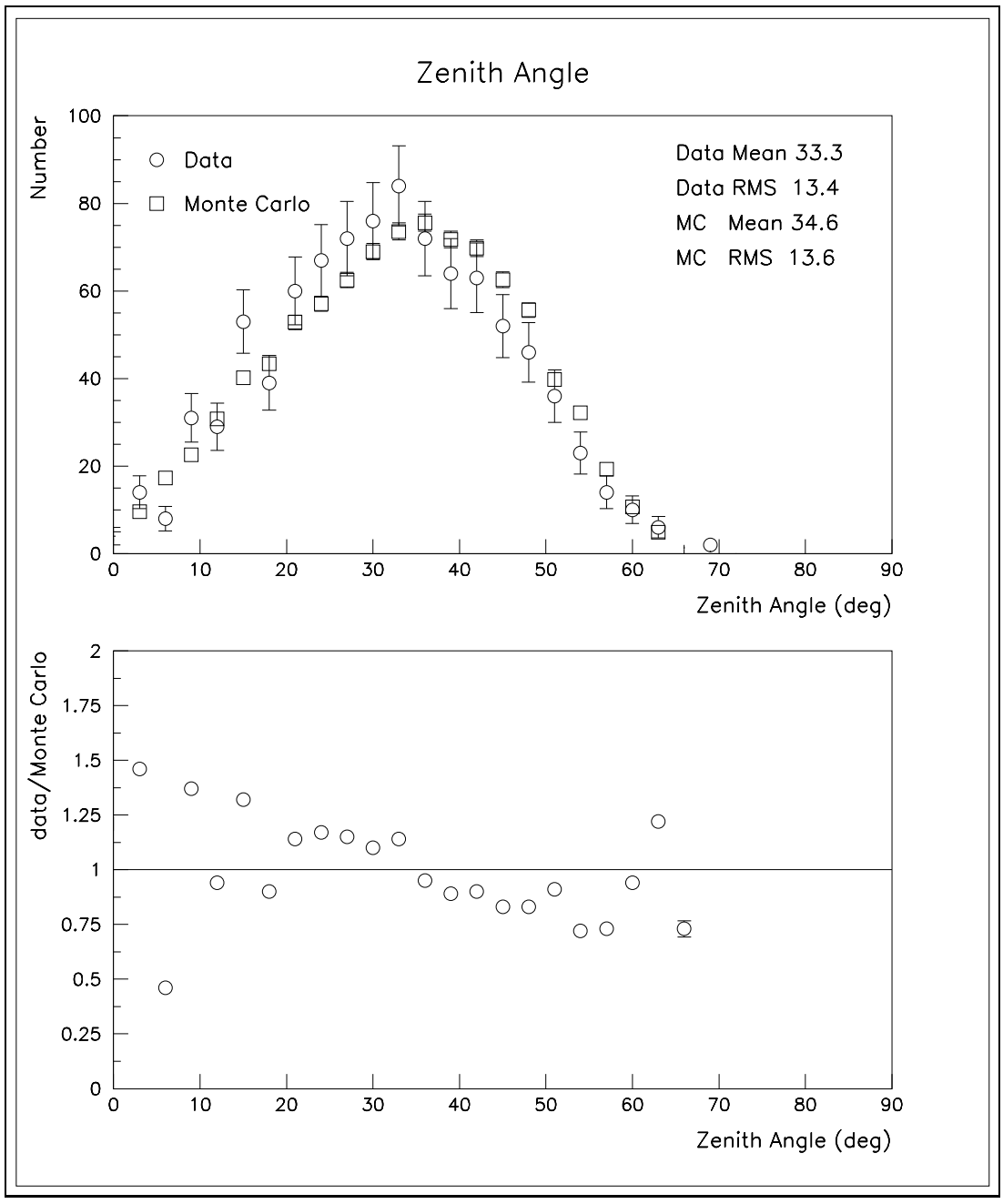

Figure 5.5. Data/Monte Carlo comparison—reconstructed zenith angle.

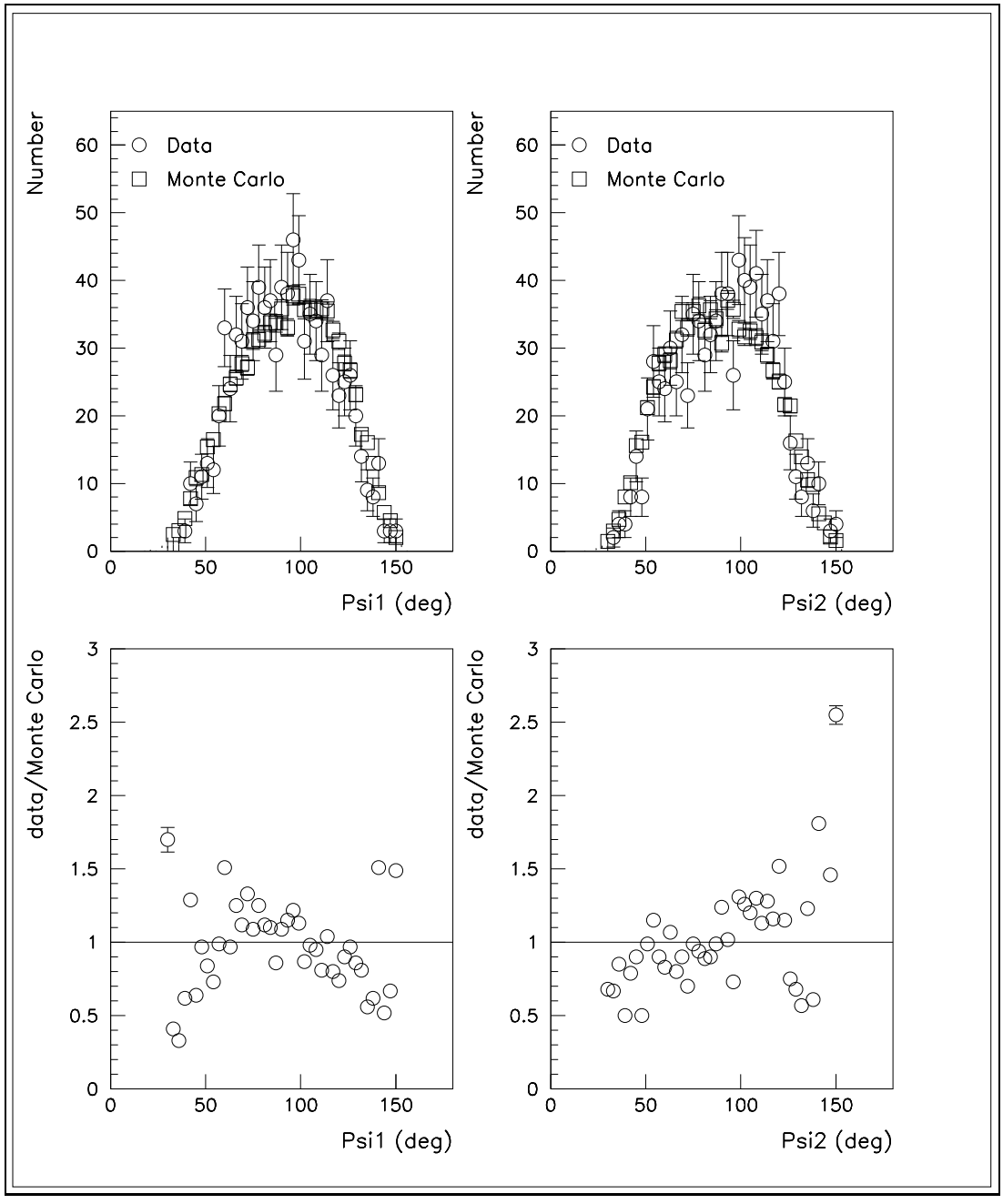

Figure 5.6. Data/Monte Carlo comparison—reconstructed ψ.

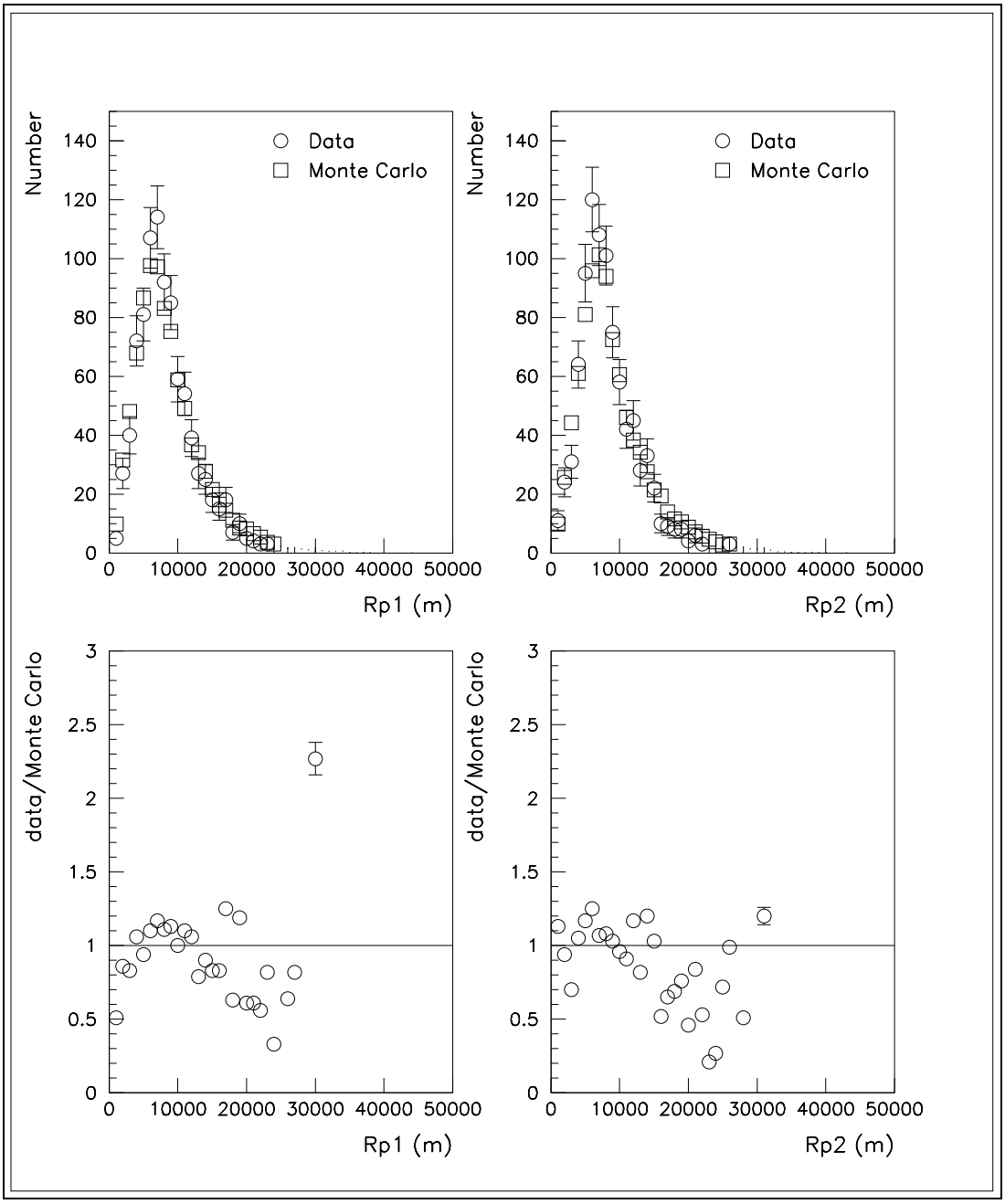

Figure 5.7. Data/Monte Carlo comparison—reconstructed R_p.

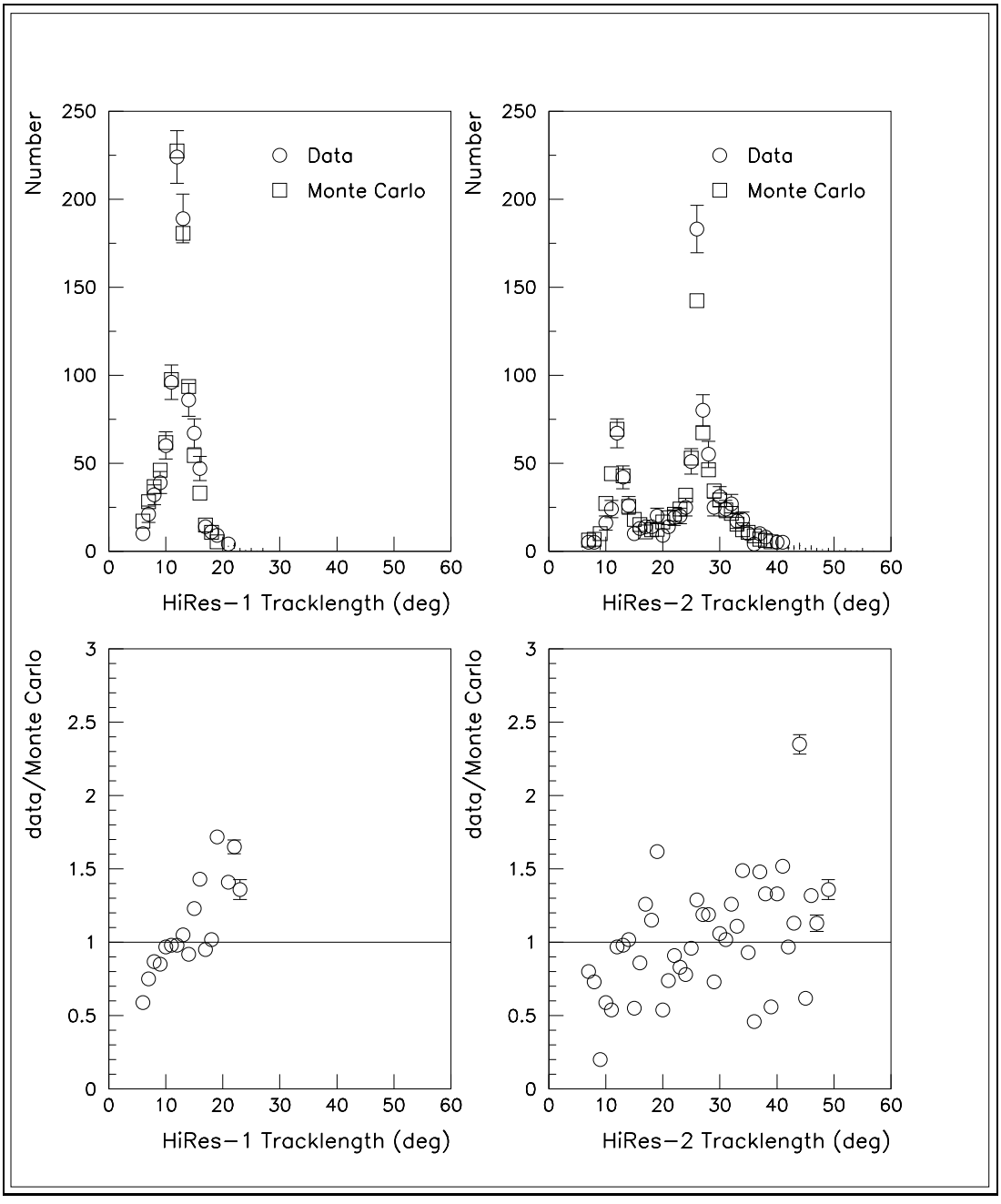

Figure 5.8. Data/Monte Carlo comparison—reconstructed angular tracklength.

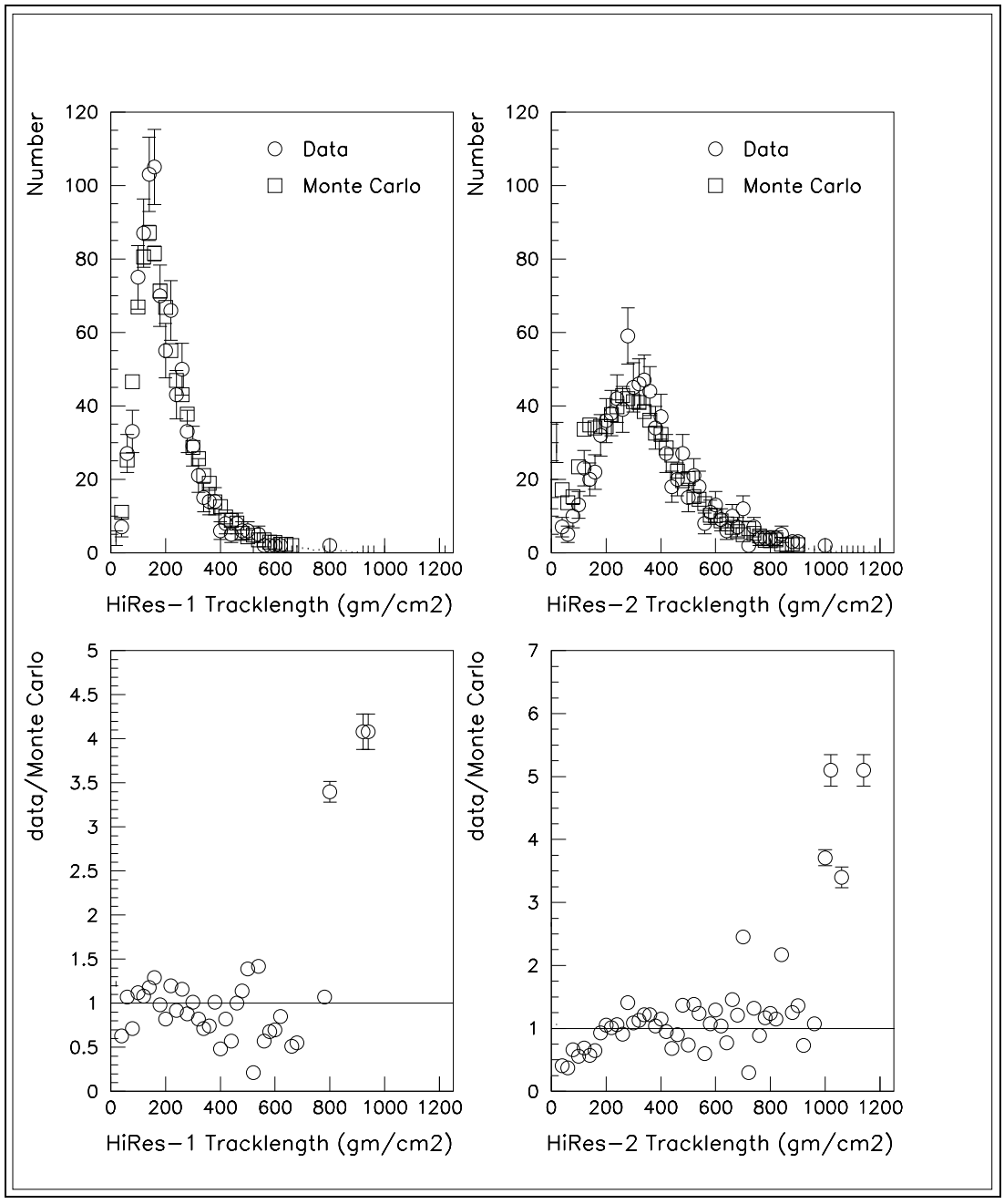

Figure 5.9. Data/Monte Carlo comparison—reconstructed atmospheric depth tracklength.

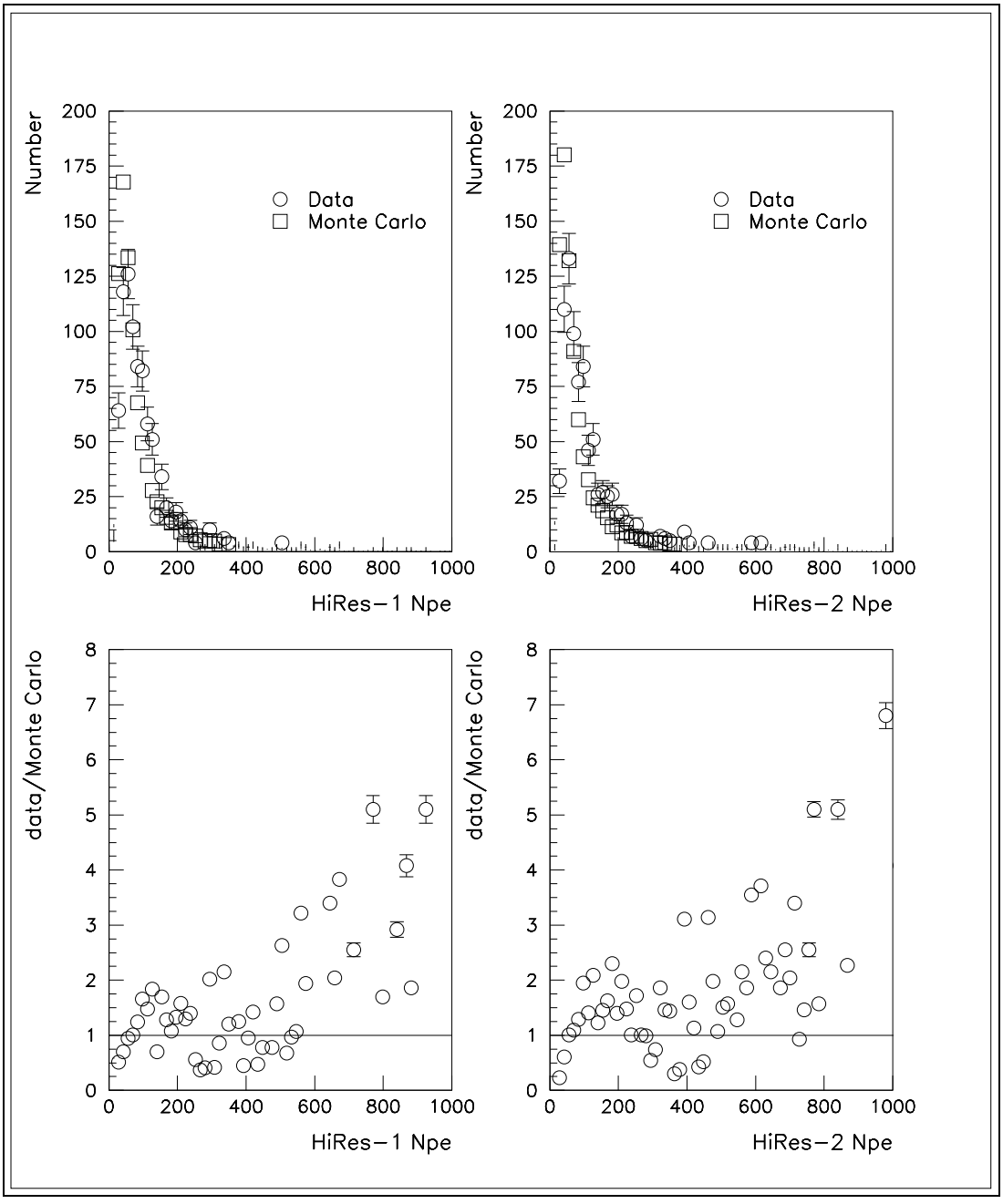

Figure 5.10. Data/Monte Carlo comparison—reconstructed N_{pe}.

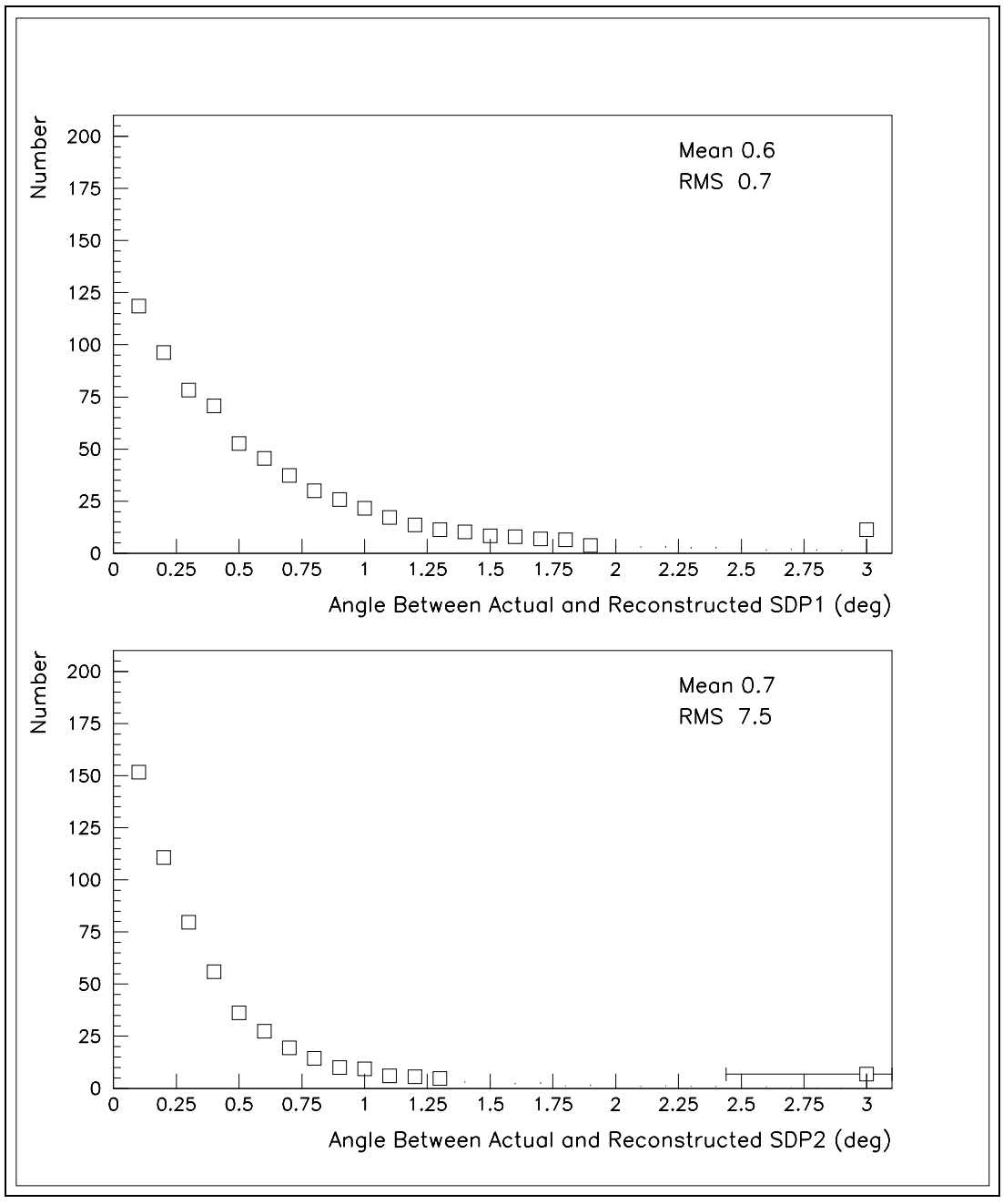

Figure 5.11. Resolution in determining the SDP. The far right bin in each plot is an overflow bin.

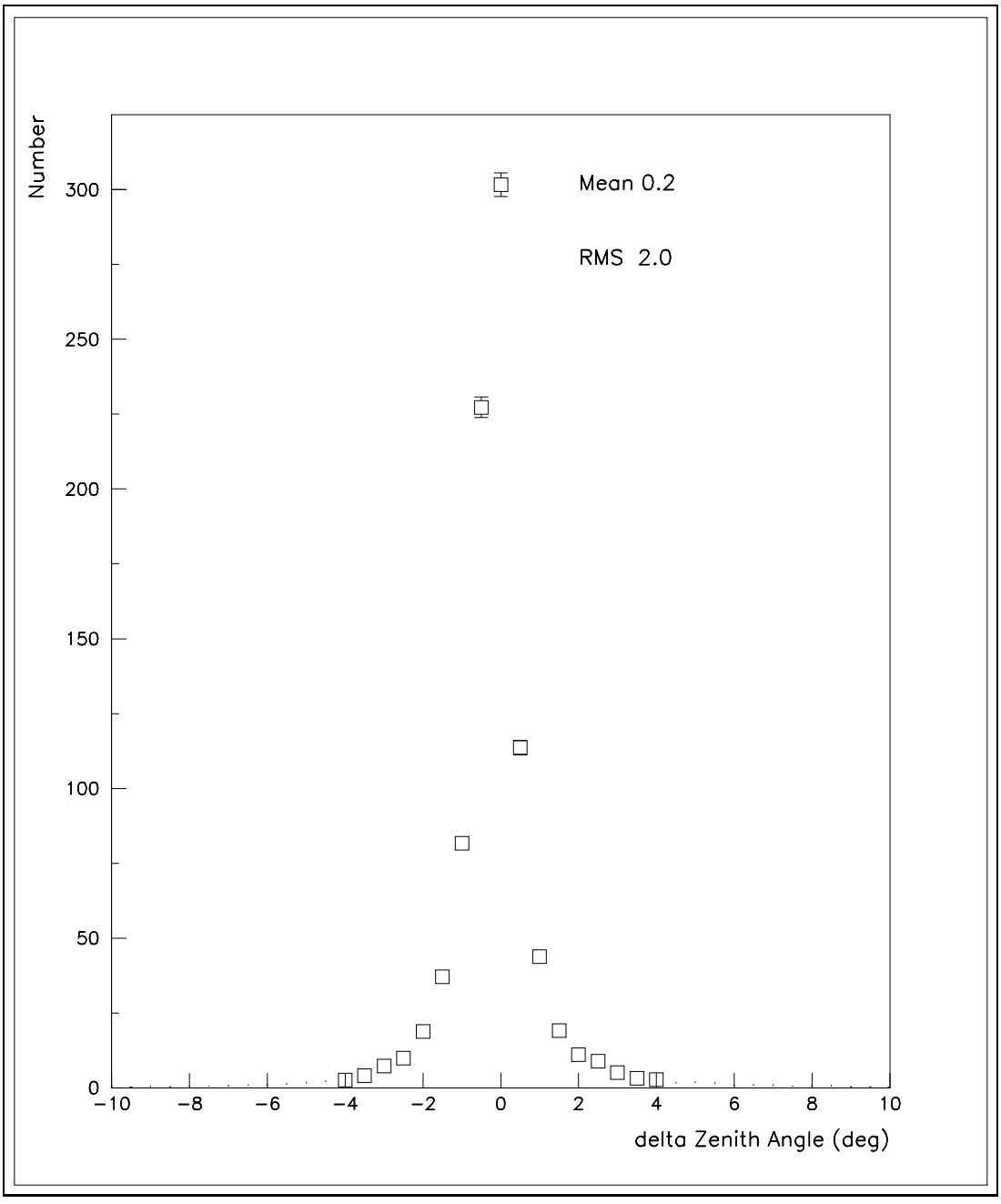

Figure 5.12. Resolution in determining the zenith angle.

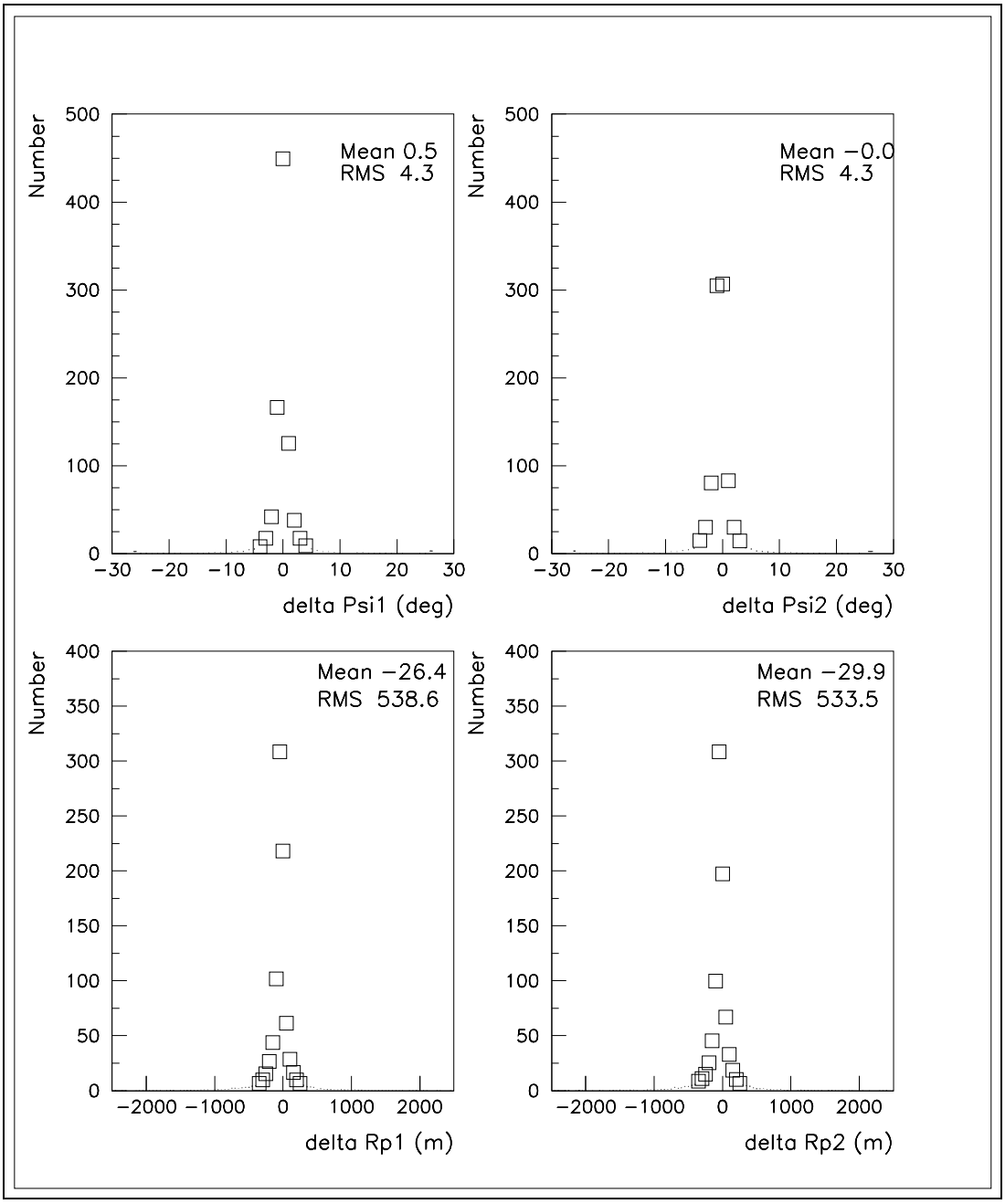

Figure 5.13. Resolution in determining ψ and R_p.

5.3.4 Geometric Uncertainty

As seen in Figure 5.11, the SDPs are reconstructed well but not without uncertainty. The uncertainty in the geometry will propagate to an uncertainty in the reconstructed X_{max}. The SDP-finding routine returns the normal to the SDP as well as the uncertainties in each component of the normal. For each SDP in each event, each component of the normal was varied by its uncertainty in all possible combinations. The new planes generated from these variations were compared to the original SDP, and the largest resulting angle between the new plane and the SDP was recorded. The original SDP was then rotated by that angle in the direction of the normal, giving a new intersection with the other site's SDP. All nine combinations of SDP rotation were tried, giving nine different geomtries which resulted in nine different X_{max} and Energy results. The difference between the largest and smallest X_{max} gave the uncertainty in X_{max} due to the uncertainty in geometry. Figure 5.14 shows the distribution of these uncertainties for X_{max} in the data and the Monte Carlo.

5.3.5 X_{max} and Energy Resolution

As explained in Seciton 4.3, the elongation rate and the width of the X_{max} distributions are the best indications of changes in the UHECR composition. Both require good resolution in both primary energy and X_{max}.

Figures 5.15 and 5.16 show the energy and X_{max} resolution, respectively. For the energy resolution, the differences in Monte Carlo energy and reconstructed energy are divided by the Monte Carlo energy.

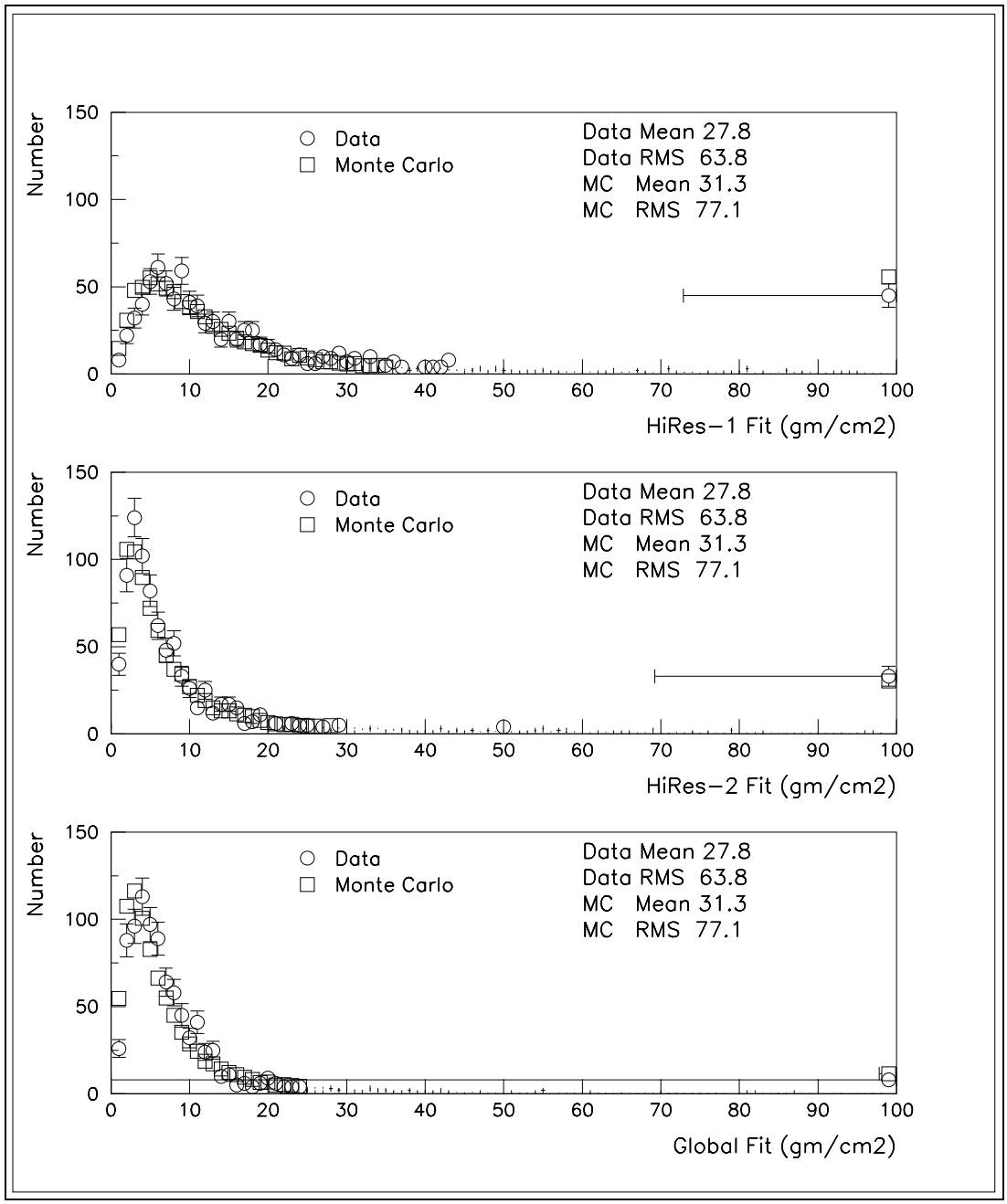

Figure 5.14. Effects of geometric uncertainty on reconstructed X_{max}. The far right bin in each plot is an overflow bin.

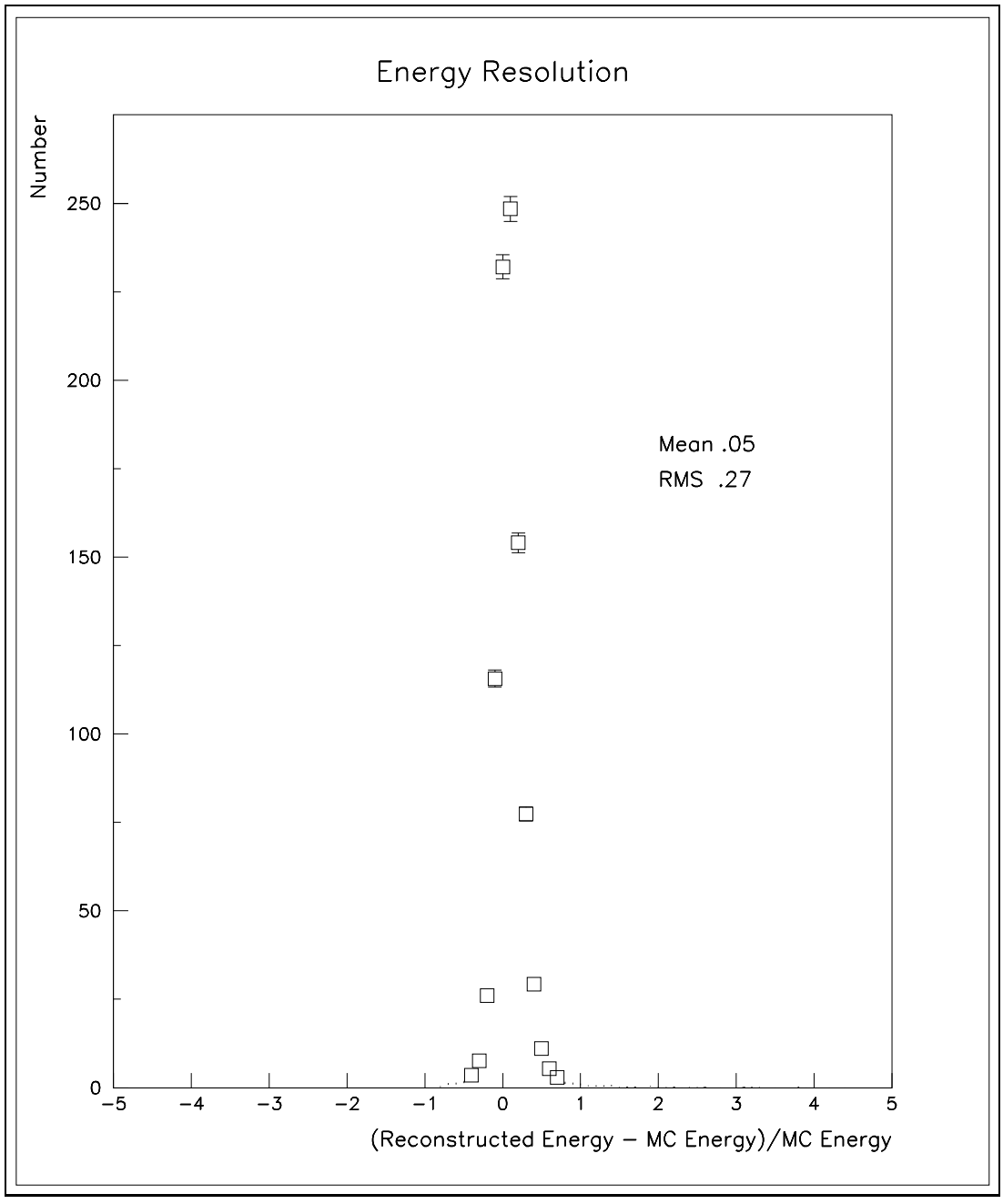

Figure 5.15. Resolution in determining energy.

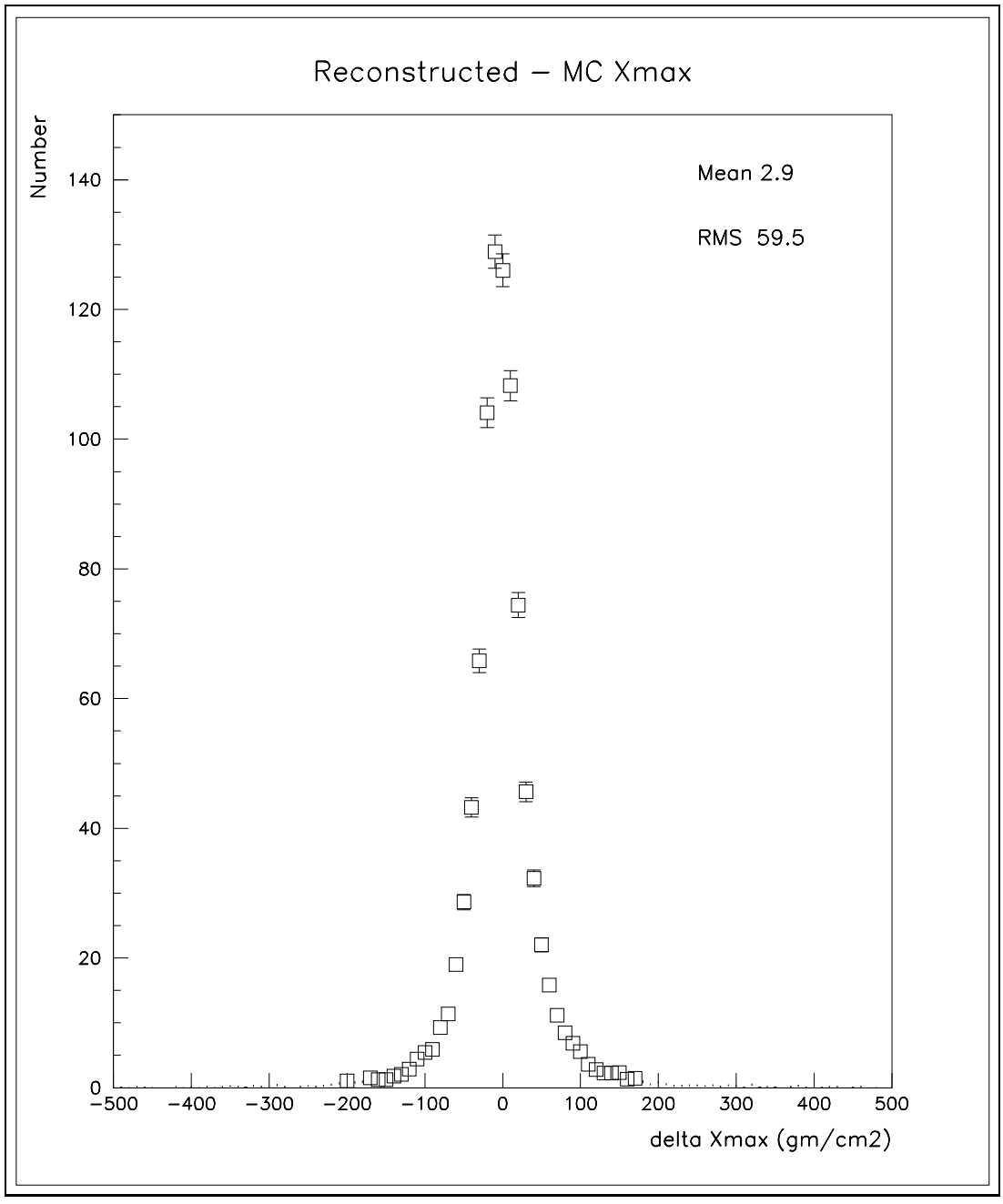

Figure 5.16. Resolution in determining X_{max}.

CHAPTER 6

RESULTS

6.1 Event Selection

In the first step of the stereo reconstruction, described in Sections 5.2.1 and 5.2.2, data for the same event from the two sites is matched in time. The most rigorous check that the two sites were synchronized is the presence of the flashers described in Section 3.3 in the matched data. Only data parts in which at least 20 flashers are seen were used for this analysis [73].

The noise filter, described in Section 5.2, determines the probability that the pattern of fired tubes could have been produced by random noise. Only events with less than a 0.1% chance of having been produced by noise were kept. The Rayleigh vector formed for the noise filter also gives the direction of the track. To reduce the possibility that tracks from the lasers described in Section 3.3 are tagged as UHECR events, any track with a direction within 20° of the horizon is rejected.

To form a valid SDP, the routine described in Section 5.2.1, requires at least three tubes within 3° of the resulting SDP. The time-binning technique of Section 5.2.3 requires five good tubes. Events not meeting these criteria were cut. Events which did not have at least 6° of tracklength at both sites were also cut, as were events that did not have at least 3 bins at each site following the angular binning procedure.

For the period between November of 1999 and September of 2001, 1198 events were reconstructed with at least one reconstructed energy (HiRes-1 or HiRes-2 individual fit or the global fit) greater than $10^{17.7}$ eV.

6.1.1 Atmospheric Cuts

Because photons from an EAS must travel through the atmosphere to the detector, understanding the scattering in the atmosphere is crucial to proper reconstruction of the UHECR event. As highlighted in Section 3.3, the horizontal attenuation length of the atmosphere and the scale height of the aerosol component of the atmosphere are measured hourly with steerable lasers and recorded in a database. Unfortunately, because of equipment down time, not every hour for which data in this analysis occurred has a database entry. For each event, the database is sampled. If an entry exists for the hour of the event or the hour on either side, the database values are used for reconstruction.

Figure 5.3 shows the distributions of the horizontal attenuation lengths, scale heights, and optical depths in the database. The measured mean optical depth at Dugway Proving Ground is 0.04 ± 0.02 (stat) $+ 0.02$ (sys), with the corresponding best values for horizontal attenuation length and scale height of 25 km and 1 km, respectively [88]. For this analysis, any event with a corresponding optical depth measurement of larger than 0.12 was cut. Of the 1198 events, 760 had database entries. Of the 760, 53 had optical depths greater than 0.12, leaving 707 events reconstructed with atmospheric parameters from the database.

The data set included 438 events that did not have entries in the atmospheric database. For the days on which these events occurred, the operators' log comments and the PWVLR measurements (see Section 3.3.1) were searched. Without regard for what time during the night the event occurred, periods during which the operators' comments suggested bad weather (e.g., "Haze so thick you could chew it") and/or the PWVLR indicated that the aperture was cloudy were discarded. 219 of the 438 events were cut due to bad weather. The remaining 219 events that had no database entry but occurred during good weather were reconstructed with a horizontal attenuation length of 25 km and a scale height of 1 km.

6.1.2 Quality Cuts

All 926 remaining events were viewed using the event display of Figures 3.1 and 3.2. Eleven were clearly not UHECR events at one site and were discarded.

Because the Monte Carlo models the detector well, it can now be used with confidence to identify selection criteria for quality events. A Monte Carlo set of 20,460 events was generated with a Fly's Eye Stereo spectrum for the study in Section 5.3. With good agreement between the data and the Monte Carlo, it is acceptable to use a 8341-event subset of those 20,460 events for the remainder of the resolution studies. The input composition for the Monte Carlo was nearly even numbers of protons and iron nuclei, evenly divided between the QGSJet and SIBYLL hadronic interaction models.

Table 6.1 summarizes the cuts chosen for each parameter. Figures 6.1 through 6.11 show the various parameters vs. the difference between reconstructed and Monte Carlo X_{max} for $\approx$ 8300 Monte Carlo events. The cuts in Table 6.1 are indicated by the horizontal lines in the figures.

Table 6.1. Quality Cuts

Parameter	Cut
Minimum Viewing Angle (both sites)	10°
Minimum Opening Angle Between SDPs	5°
Individual Site Fit χ^2	20
Global Fit χ^2	15
Timing Fit X_{max} - Global Fit X_{max}	500 gm/cm^2
HiRes-1 Fit X_{max} - HiRes-2 Fit X_{max}	500 gm/cm^2
Geometric Uncertainty in Individual Site Fit	400 gm/cm^2
Geometric Uncertainty in Global Fit	200 gm/cm^2

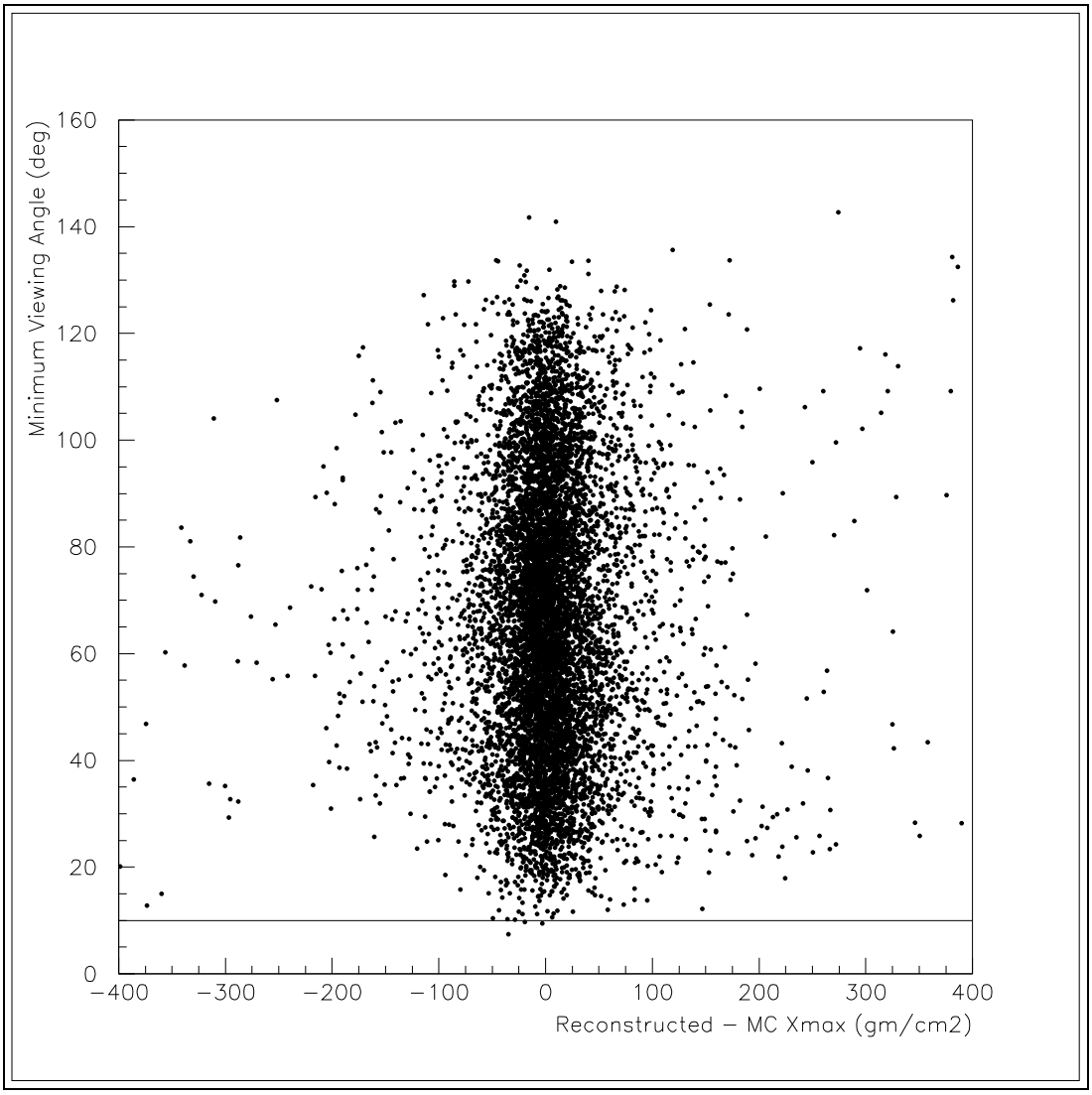

Figure 6.1. Viewing angle cut at HiRes-1.

Minimum viewing angle is a concern because proper reconstruction of events pointed at the camera is especially dependent on the modeling of the forward-beamed Čerenkov light and the atmospheric scattering. The cut on opening angle between the SDPs is necessary because the geometry obtained by the intersection of the SDPs is not well-constrained when the planes are nearly parallel.

As explained in Section 5.2.2, the Gaisser-Hillas profile can be fit to HiRes-1 or

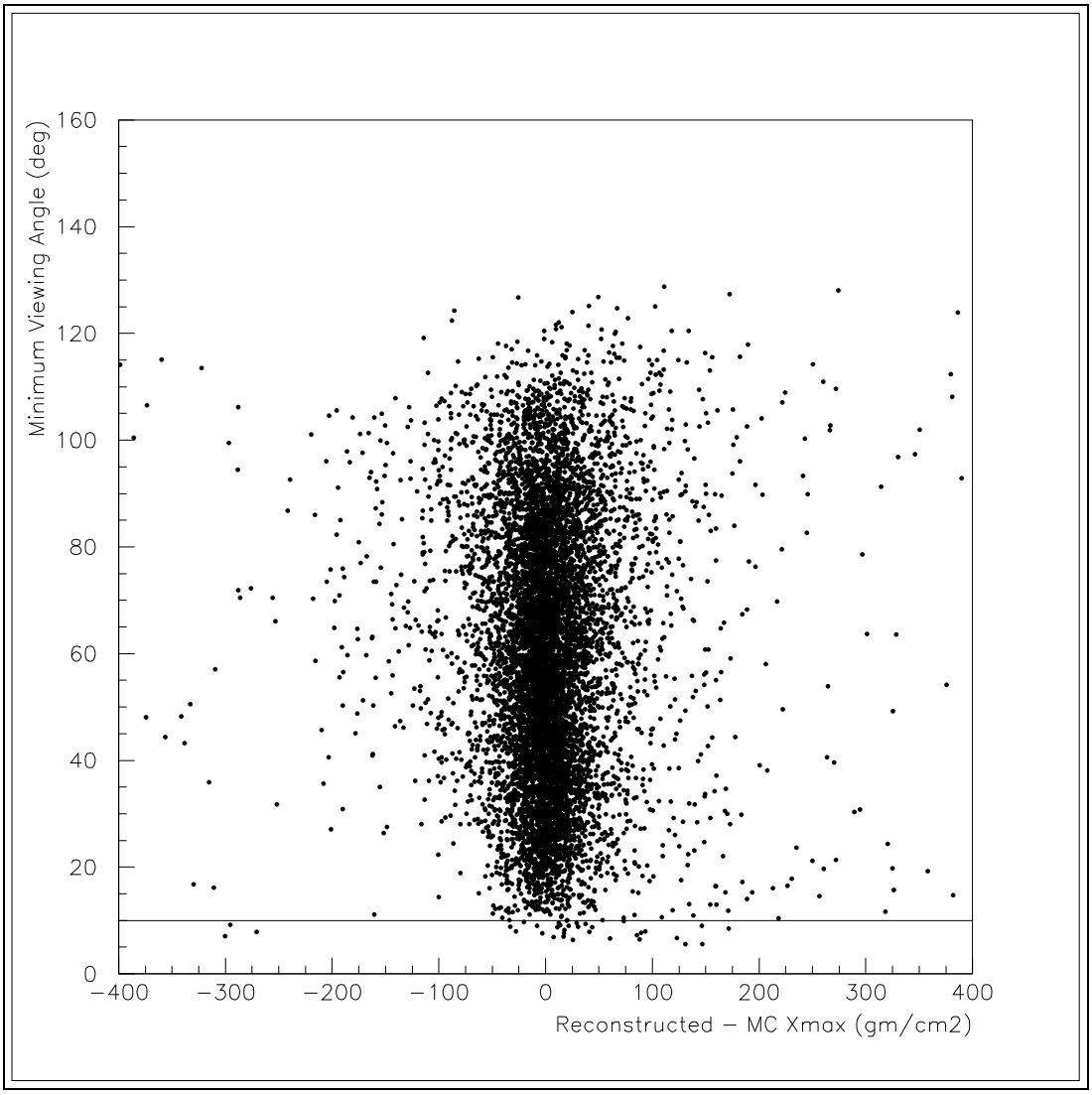

Figure 6.2. Viewing angle cut at HiRes-2.

HiRes-2 data individually or to both globally. The results reported here are from the global fit, but the individual fits do provide quality selection criteria. Events for which the χ^2 per degree of freedom of either of the individual fits was larger than 20 were cut. For the global fit, the χ^2 cut was 15.

Events for which the disparity between the HiRes-1 and HiRes-2 fits was more than 500 gm/cm^2 were discarded. Similarly, each X_{max} from the time binning

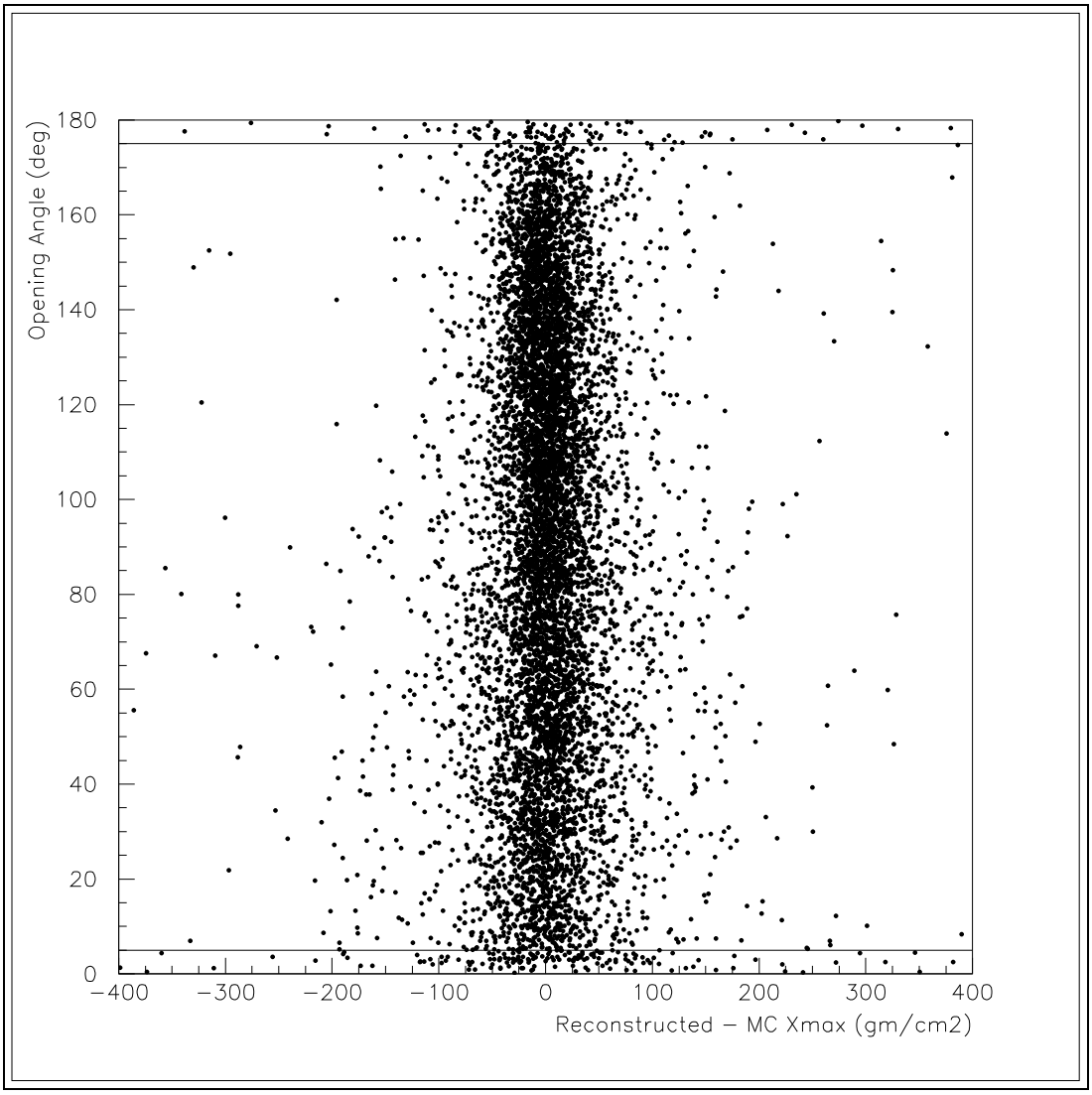

Figure 6.3. Opening angle cut.

technique of Section 5.2.3 was compared to the X_{max} from the angular binning global fit, and events differing by more than 500 gm/cm^2 were cut.

Finally, the geometric uncertainty explained in Section 5.3.4 was required to be smaller than 400 gm/cm^2 for the HiRes-1 and HiRes-2 and smaller than 200 gm/cm^2 for the global fit.

These loose cuts reduced the data set to 842 events, but improved the resolution

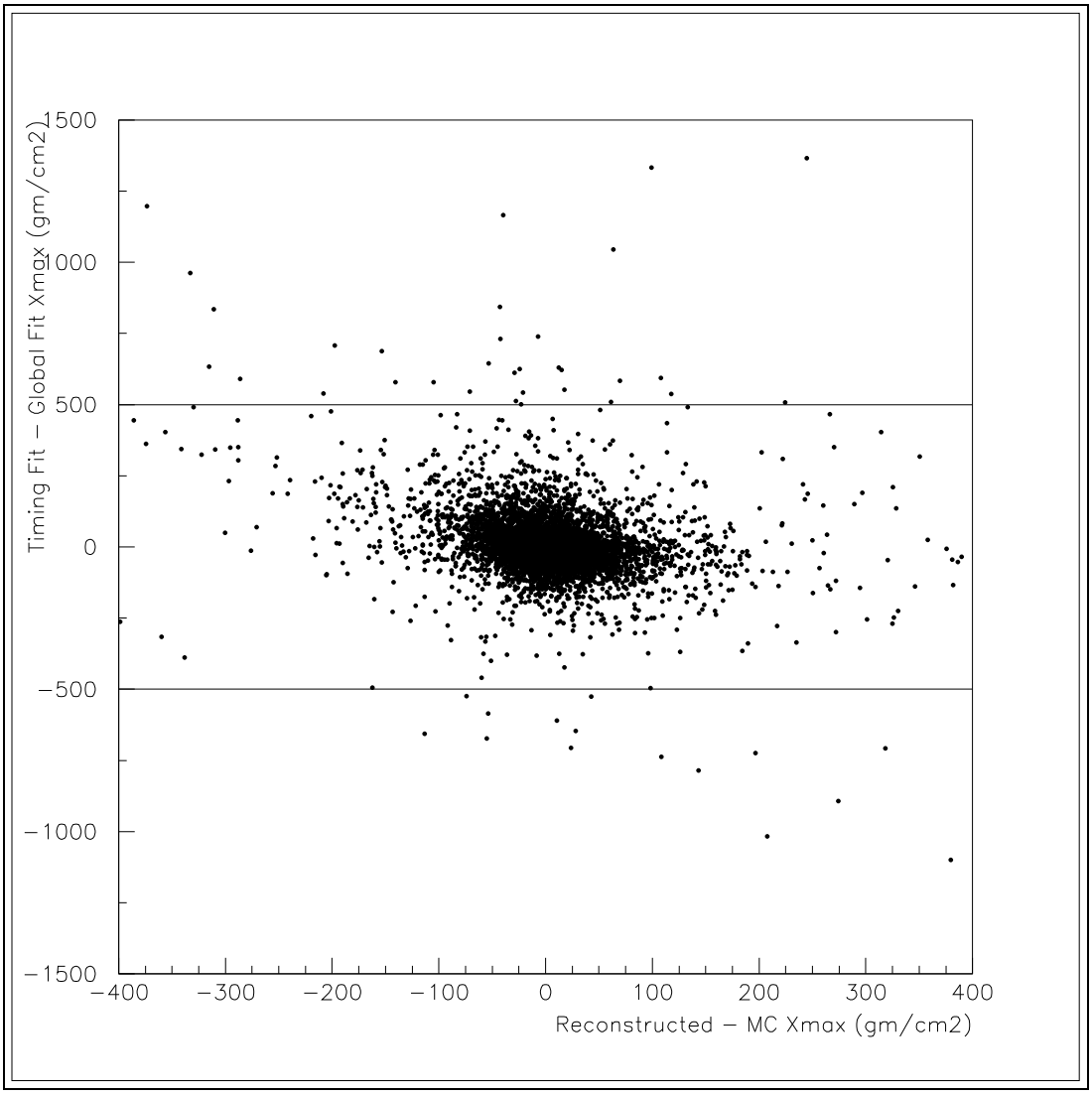

Figure 6.4. Timing fit X_{max} − global fit X_{max} cut.

in X_{max} from 60 to 45 gm/cm^2 (see Figures 5.16 and 6.12) and in energy from 27 to 17% (see Figures 5.15 and 6.13). Tightening the cuts was studied, but resulted in the removal of events from the data set without improving the resolution.

The final cut, dubbed a bracketing cut, required that at least one of the two sites "see" X_{max}. The two sites often view different parts of the EAS. Confidence that the fit to Eq. (2.18) found the correct X_{max} is bolstered when one of the sites

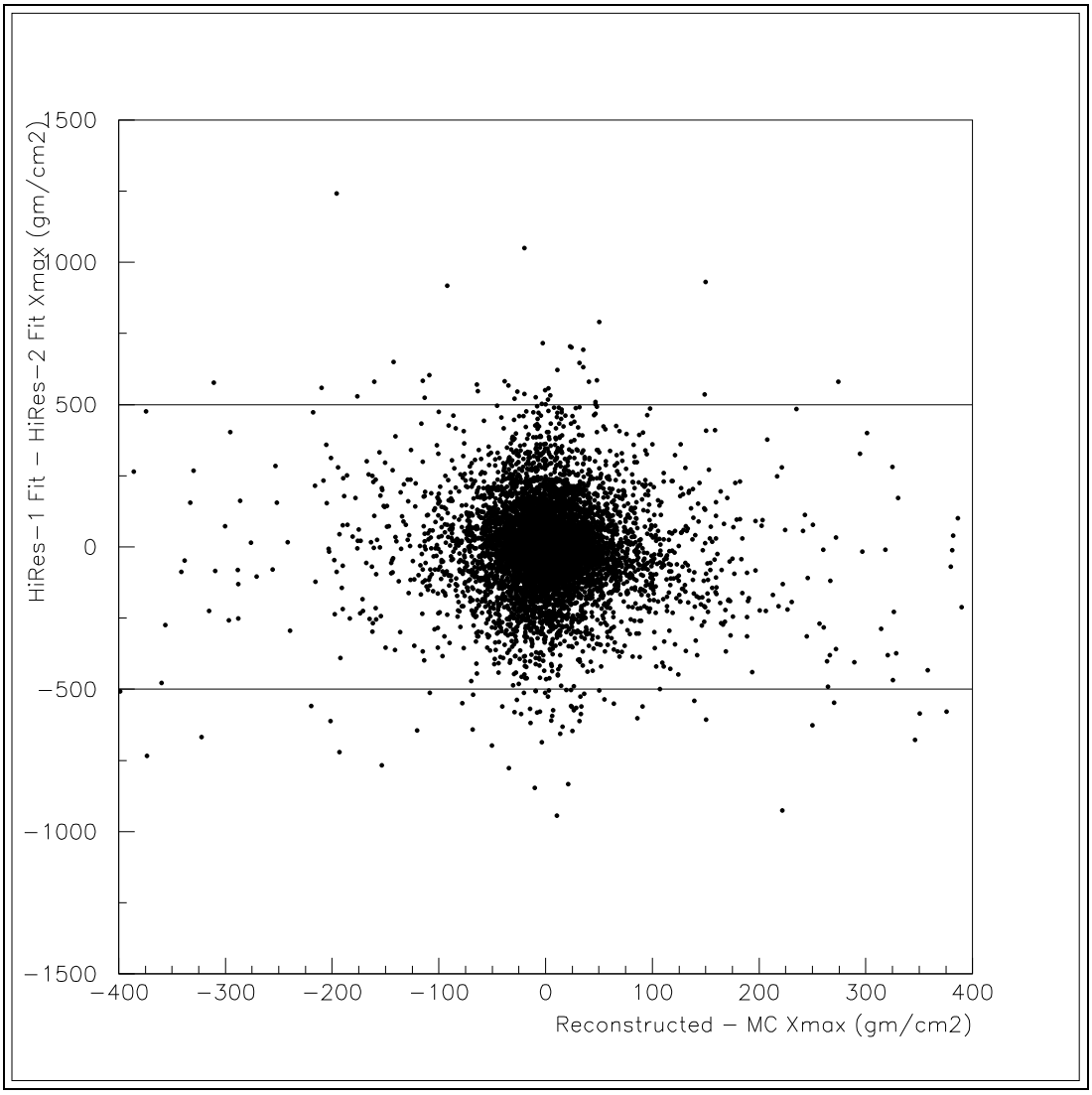

Figure 6.5. HiRes-1 fit X_{max} − HiRes-2 fit X_{max} cut.

saw both the rise to and fall from X_{max}. The bracketing cut required that both the rise and fall were viewed for each event. However, because the resolution is about 40 gm/cm^2, the bracketing cut was given some latitude. The cut required that the measured X_{max} was no more than 60 gm/cm^2 beyond the viewed track.

The final data set was comprised of the 723 events that survived all of the above cuts, 542 of which were reconstructed with parameters from the atmospheric

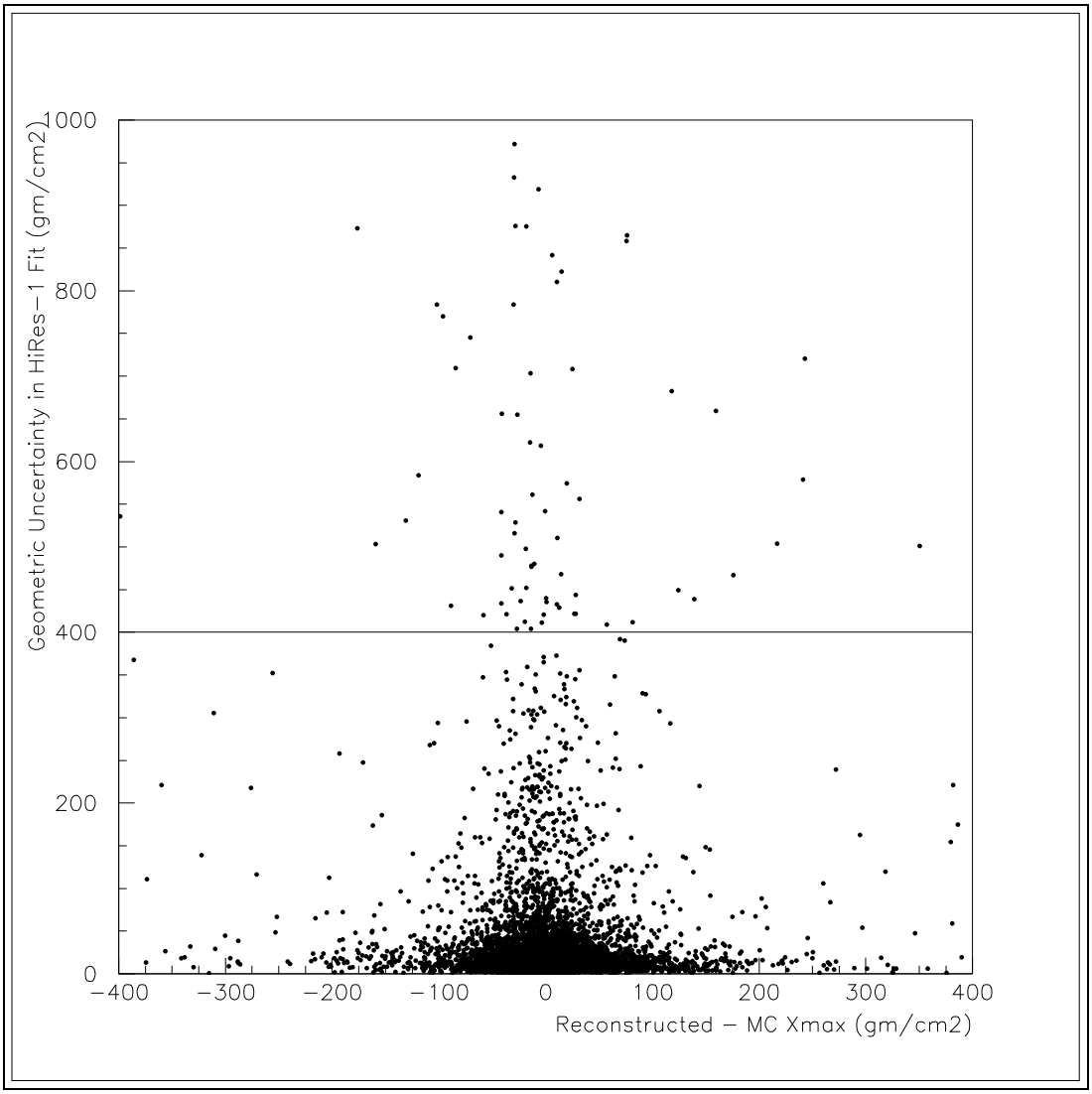

Figure 6.6. Cut on geometric uncertainty in HiRes-1 fit.

database. The same cuts applied to the Monte Carlo set gave an X_{max} resolution of 30 gm/cm^2 and an energy resolution of 13%. (See Figures 6.14 and 6.15.)

6.2 Elongation Rate Result

The data were binned in energy as shown in Table 6.2. Some of the bins above log(E/eV) = 19.4 were widened to increase the sample size per bin. The statistical

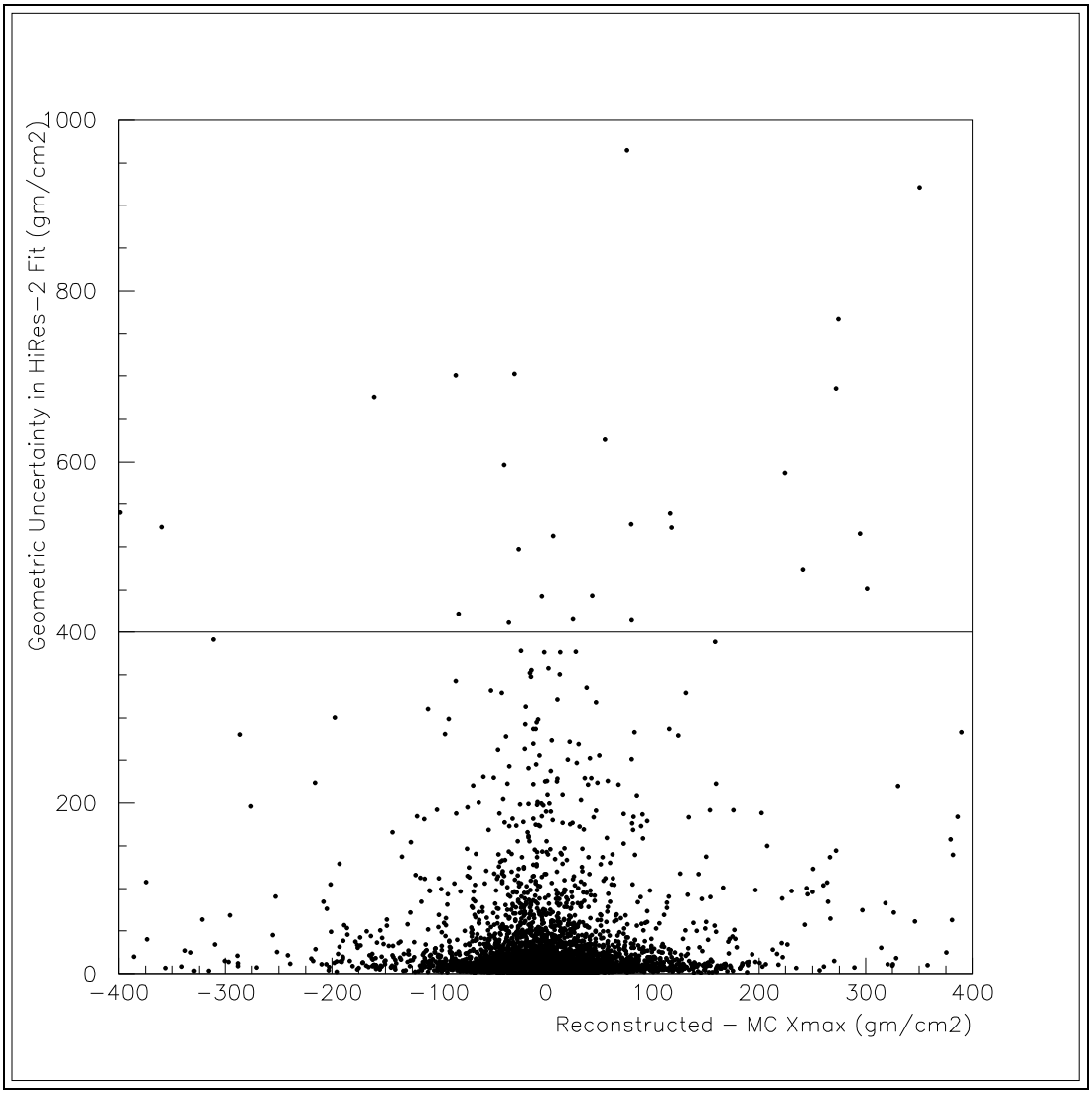

Figure 6.7. Cut on geometric uncertainty in HiRes-2 fit.

errors are the variance of the mean.

Figure 6.16 shows the ER result. The QGSJet model predictions and the HiRes Prototype result are also indicated. The measured ER is 55.2 $\pm$ 5.0 (statistical uncertainty only; see Section 6.2.1), compared to the model predictions of 50 and 61 for QGSJet protons and iron nuclei, respectively, and 57 and 59 for SIBYLL protons and iron nuclei, as well as to the HiRes Prototype result of

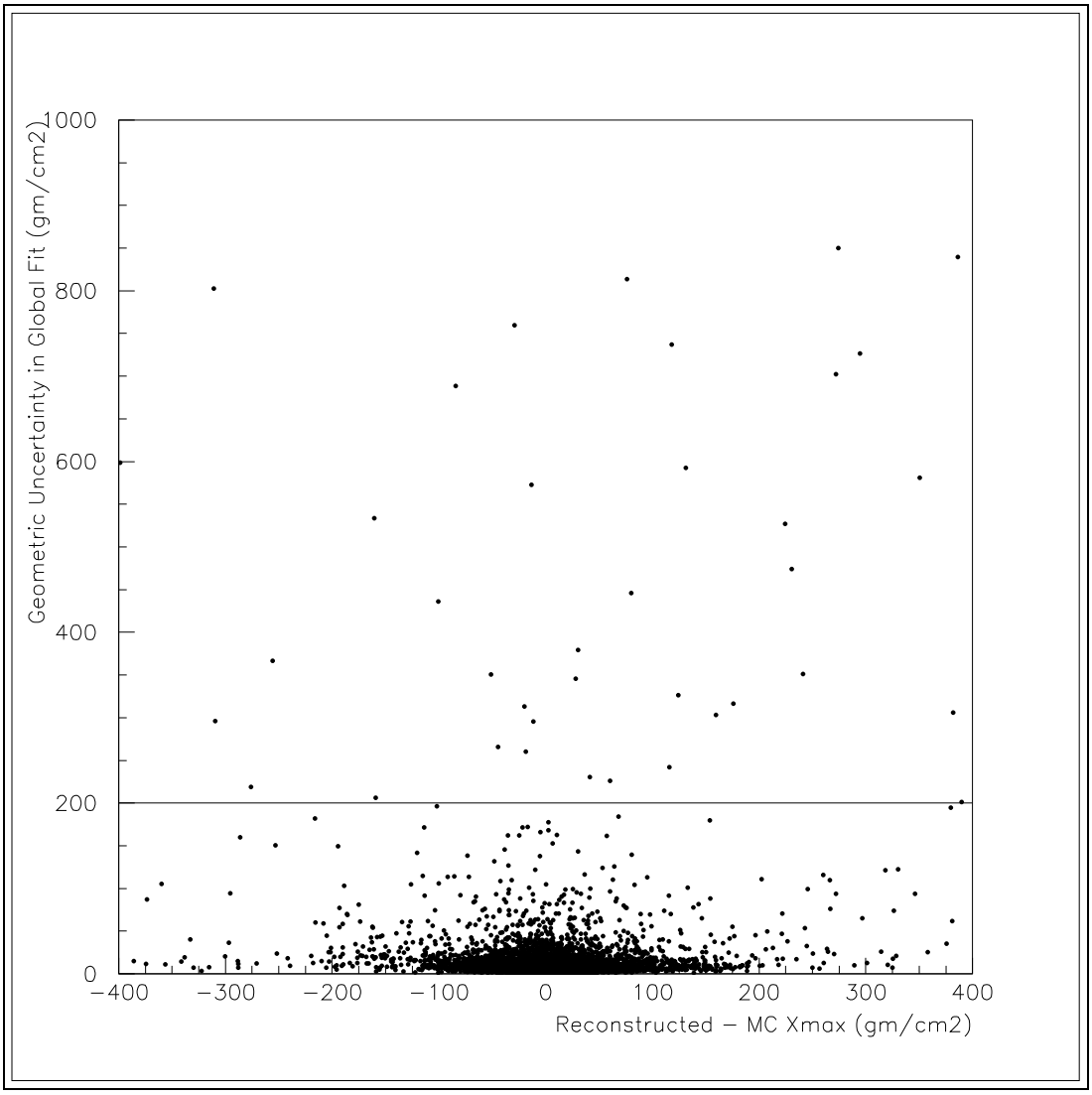

Figure 6.8. Cut on geometric uncertainty in global fit.

93.0 ± 8.5 (stat) $\pm$ 10.5 (sys).

6.2.1 Systematic Uncertainty in Elongation Rate

Historically one of the largest systematic errors in the air fluorescence technique is the error introduced by the uncertainty in the atmosphere. As discussed in Section 6.1.1, the measured atmosphere at HiRes is parameterized by an optical

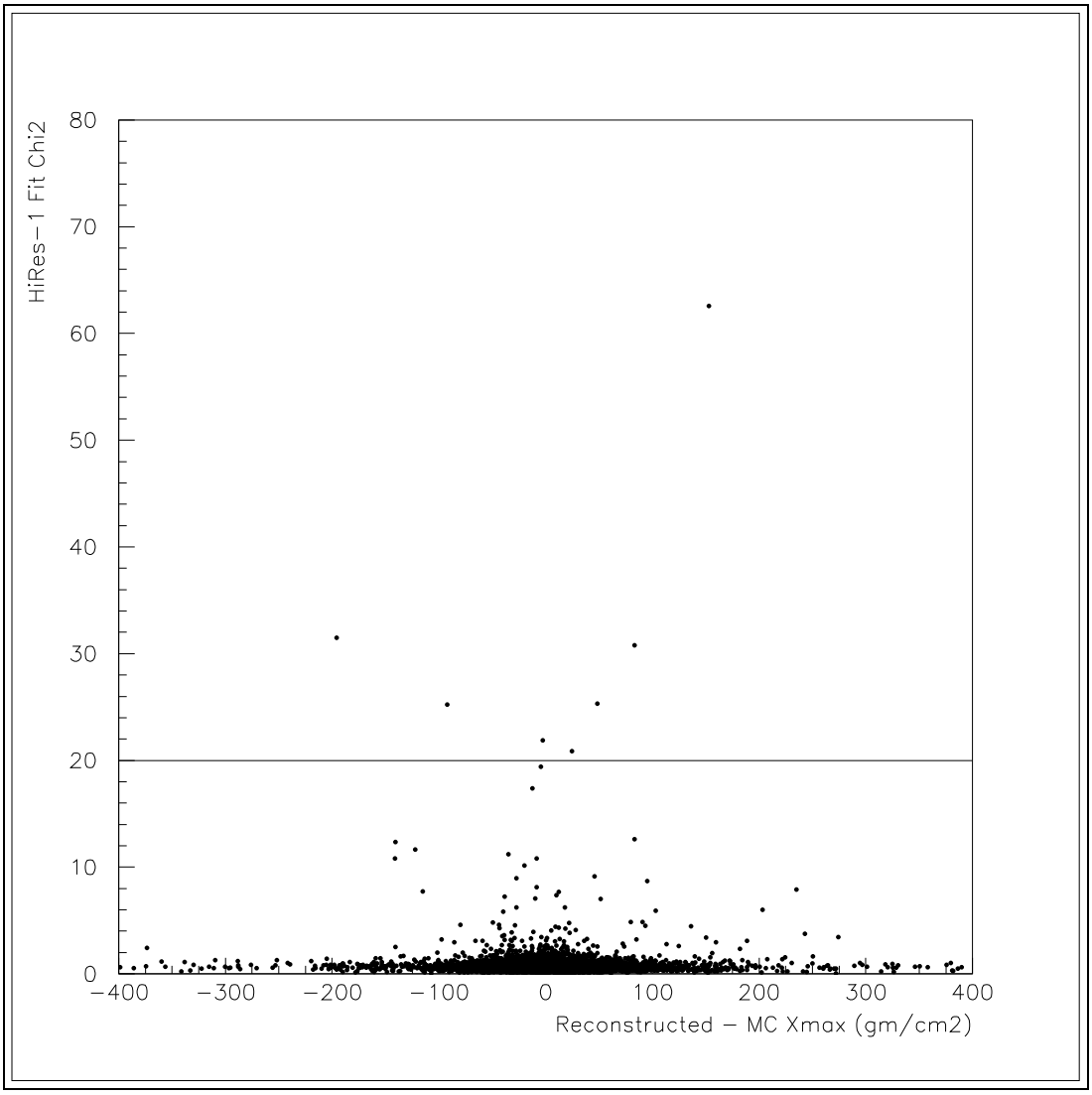

Figure 6.9. HiRes-1 fit χ^2 cut.

depth of 0.04 $\pm$ 0.02 (stat) + 0.02 (sys). Because the database used to obtain this result was used in the reconstruction of about 3/4 of the events, the statistical variation is already represented in the data. The effects of the systematic error were studied by re-processing the data with a dirtier atmosphere. Just as in the original processing, the atmospheric database was sampled and either the database entry or the standard atmosphere was used, as appropriate. However, for each event, the

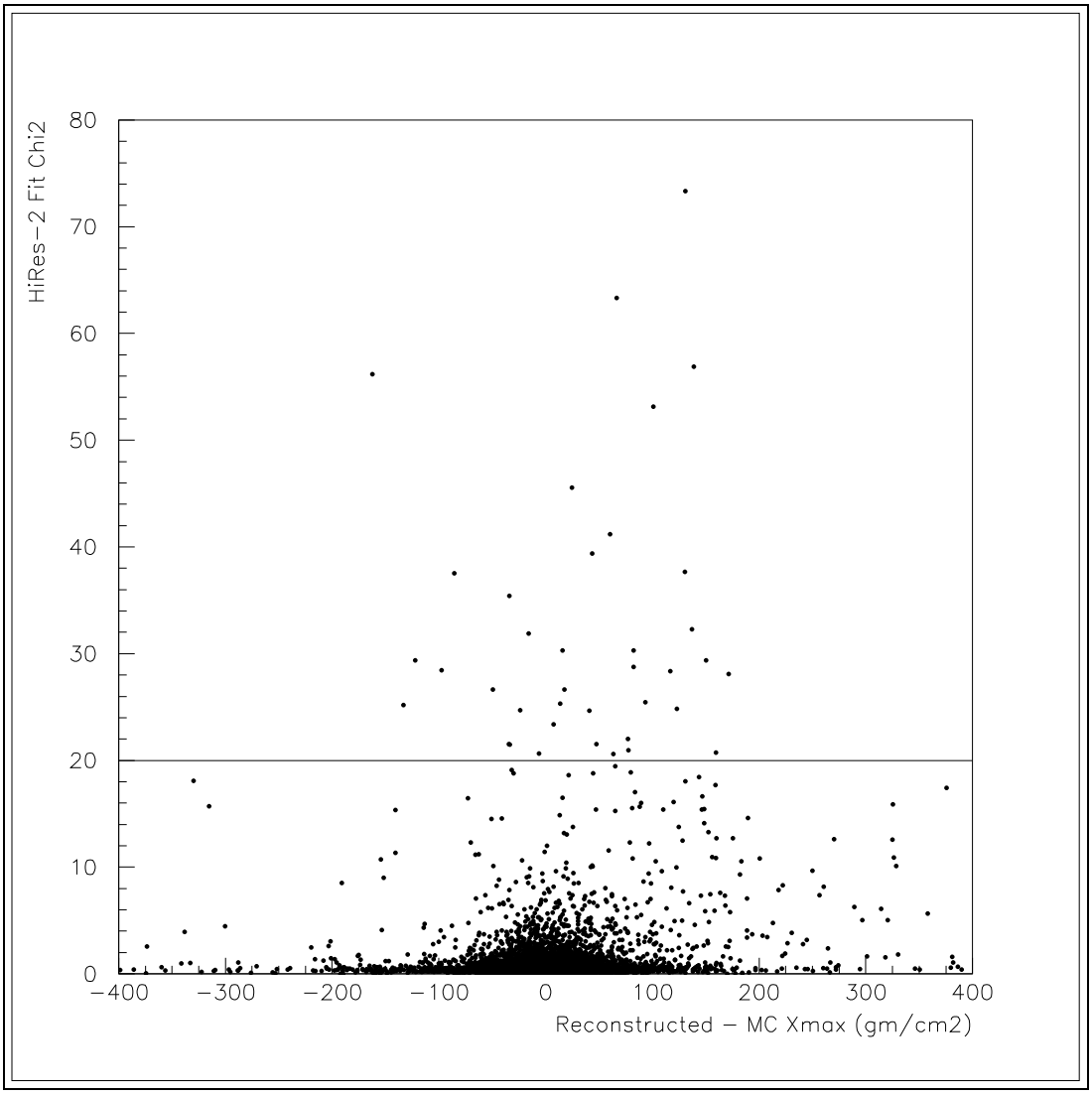

Figure 6.10. HiRes-2 fit χ^2 cut.

aerosol scale height was increased such that the optical depth was increased by 0.02.[1] The dominant effect of the dirtier atmosphere was to increase the reconstructed energies. The reconstructed X_{max} values also decreased slightly, with the two effects

[1]Referring to Eq. (3.4), either scale height or horizontal attenuation length can be changed to increase optical depth. Scale height was chosen because the measurement of horizontal attenuation length is much more rigorous and less dependant on assumptions than the measurement of vertical scale height.

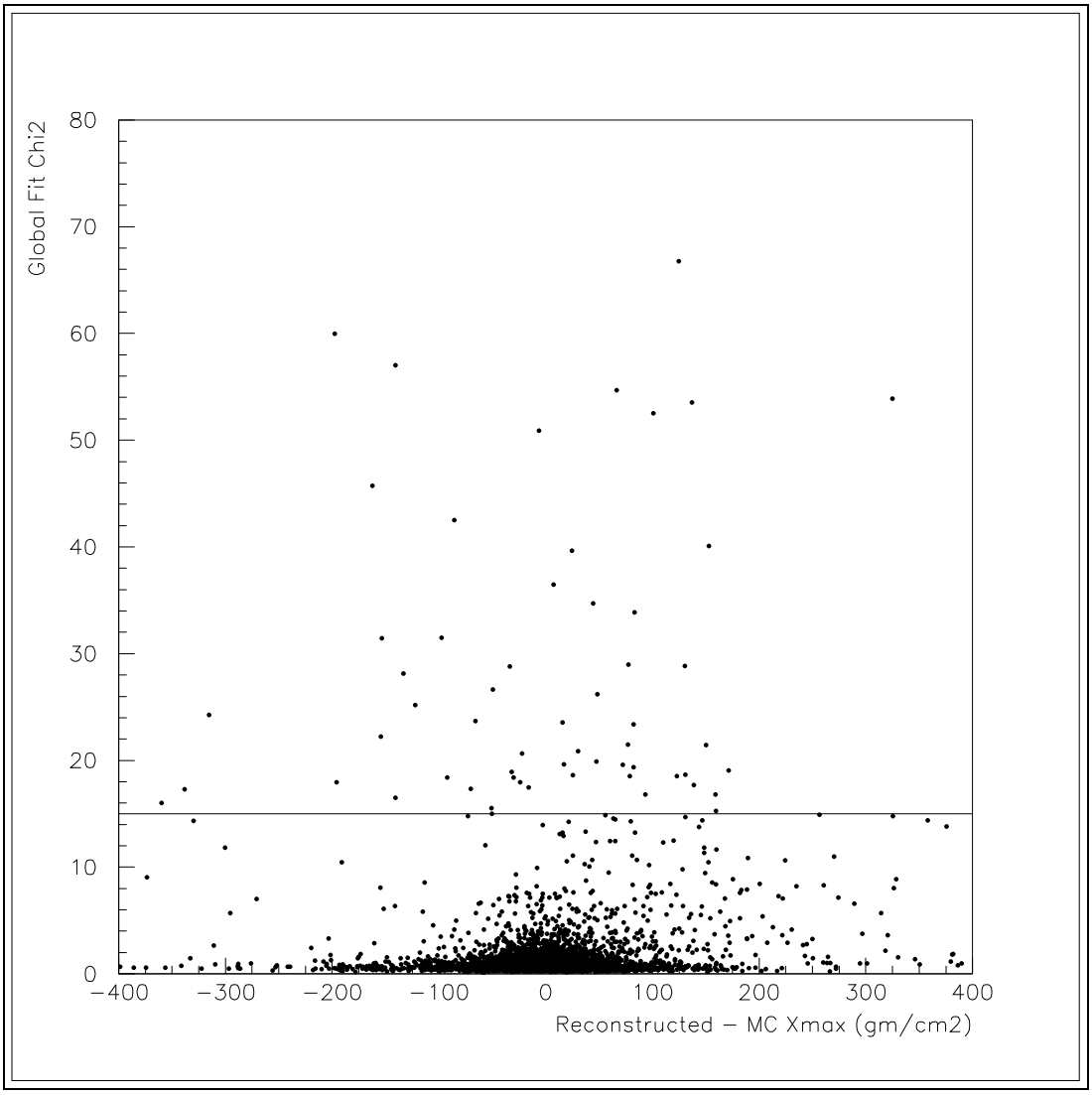

Figure 6.11. Global fit χ^2 cut.

combining to steepen the ER, as shown in Figure 6.17. Because the energy scale is logarithmic and because the atmosperic cuts on the data were harsh (see Section 5.3.1), the uncertainty introduced is small.

The dirty atmosphere illustrates the requirements for a change in ER. Uncertainties in energy do not have a large affect on ER because of the logarithmic energy scale. Any systematic uncertainty in X_{max} which applies over the entire

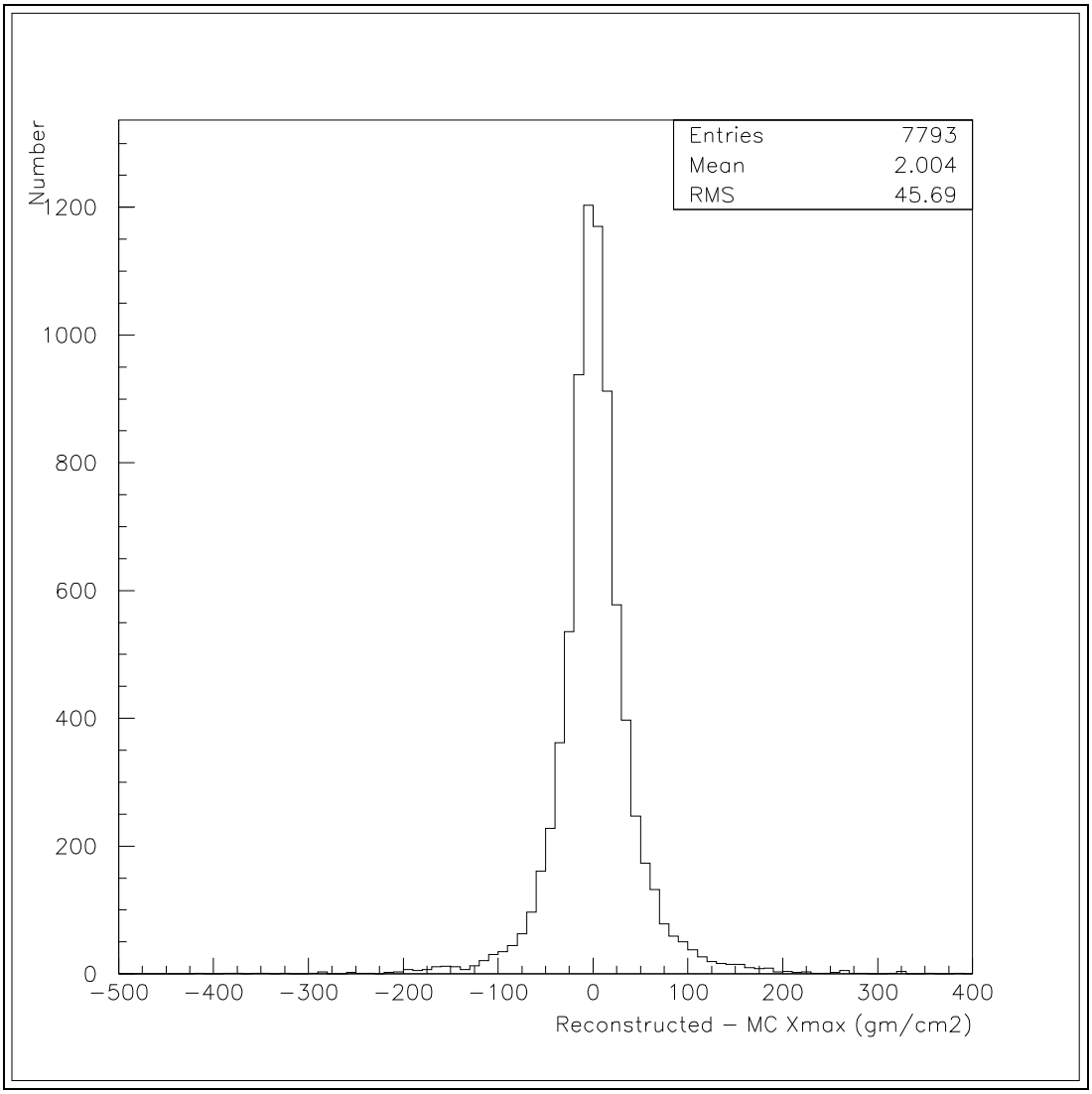

Figure 6.12. Resolution in X_{max} after loose quality cuts.

energy range will change the absolute value of X_{max}, but will not change ER. The intercept of the fit will change, but the slope will not, so the fit merely slides up or down on the X_{max} axis. To affect ER, the systematic uncertainty must shift X_{max} in an energy-dependent way.

The model of the Čerenkov beam could introduce such an energy-dependent uncertainty in X_{max}. To investigate this, the reconstruction code was modified to

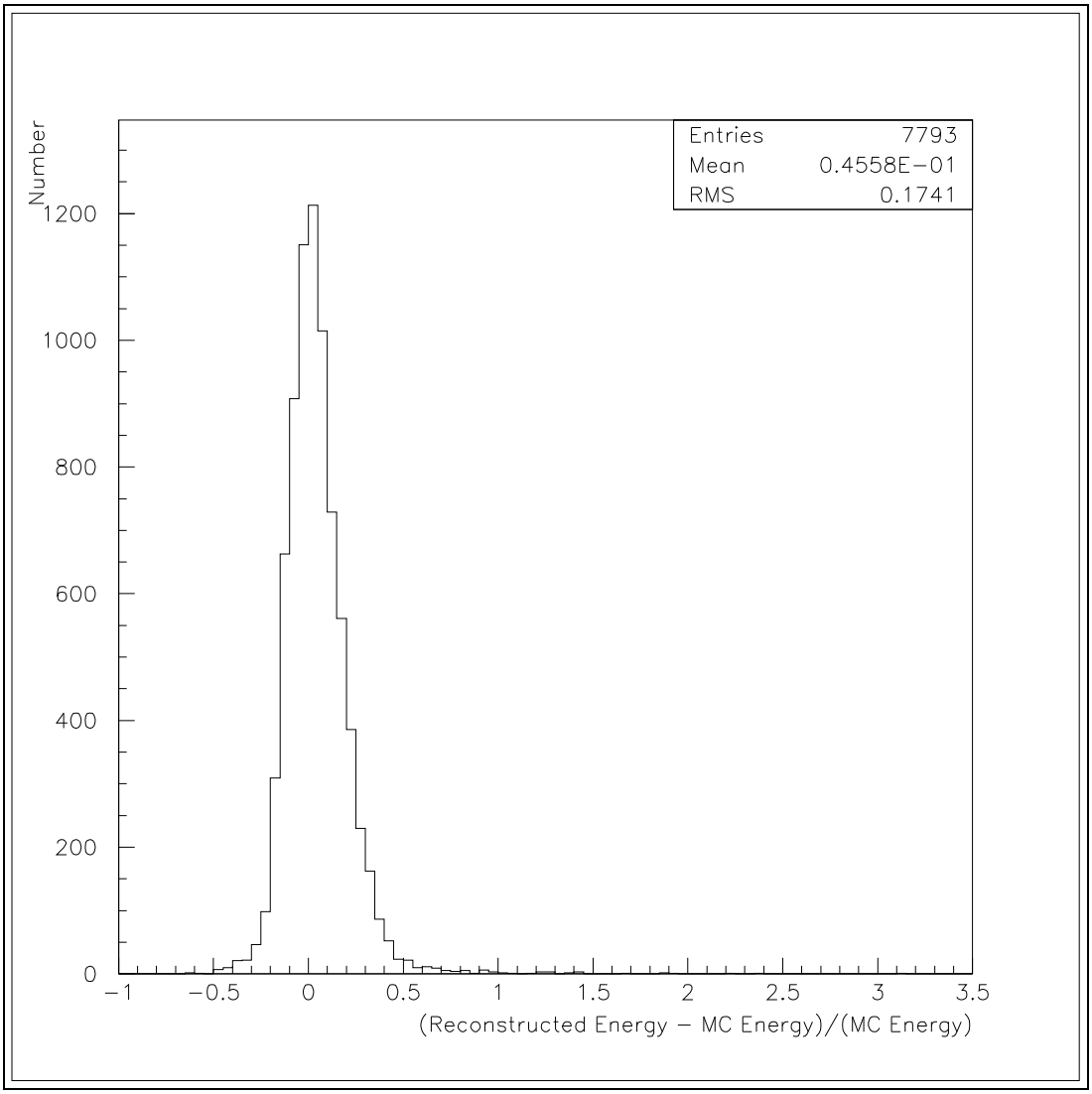

Figure 6.13. Resolution in energy after loose quality cuts.

make the modeled Čerenkov beam 2° wider, and the data were reprocessed. The ER was unchanged.

6.3 X_{max} Distribution Width Result

Figures 6.18–6.21 show the X_{max} distribution width result. The histograms representing the hadronic interaction models in Figures 6.18–6.21 were obtained by

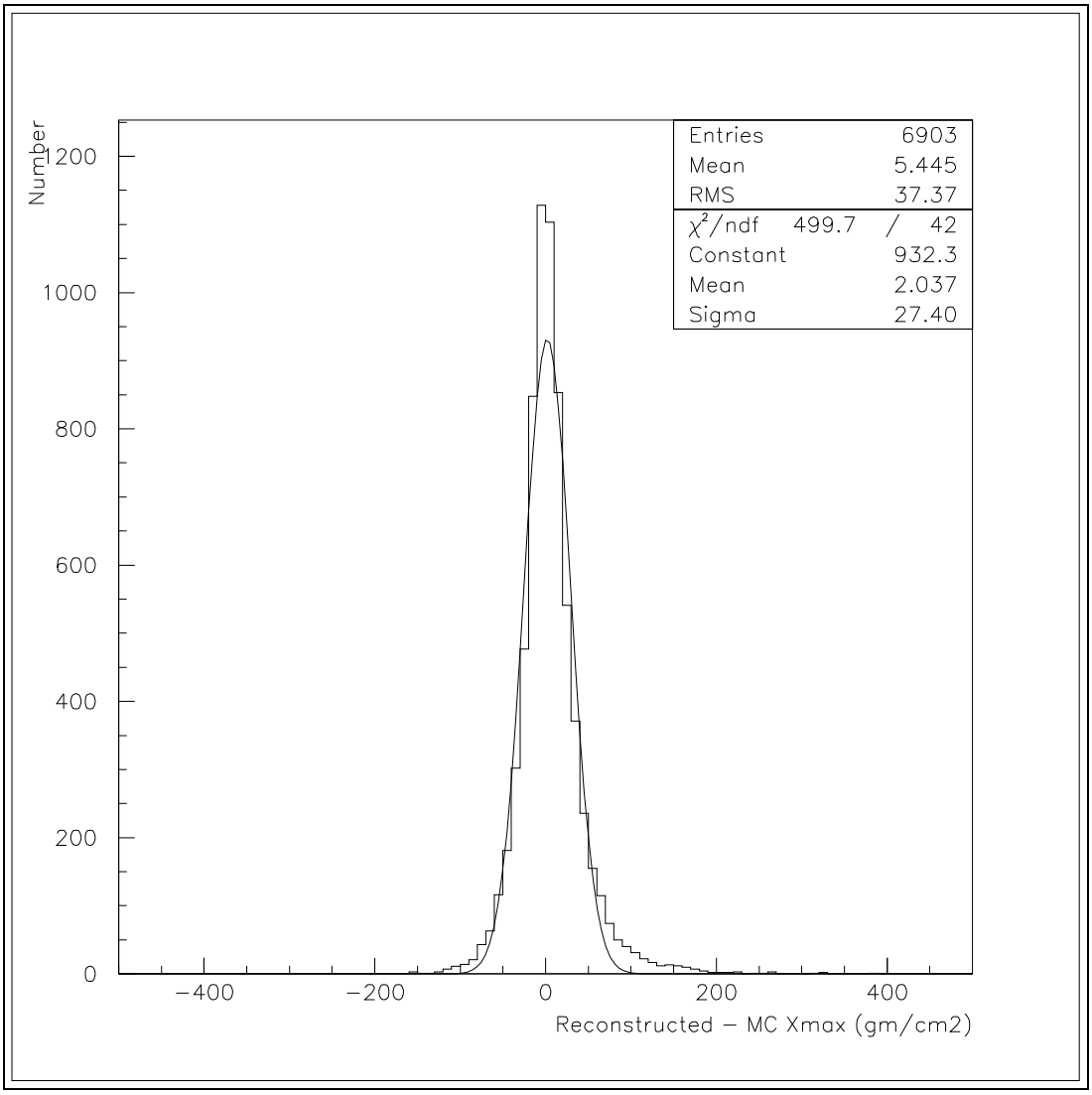

Figure 6.14. Final resolution in X_{max}.

taking over 4500 showers for each model through the complete Monte Carlo and reconstruction routines, subject to the same cuts as the data. Nearly 4000 events of each type survived. The areas of the Monte Carlo histograms are normalized to the area of the data histogram.

For Figure 6.18 and 6.19, the data events were divided into three energy bins selected such that each contained about 1/3 of the events. The width is not changing

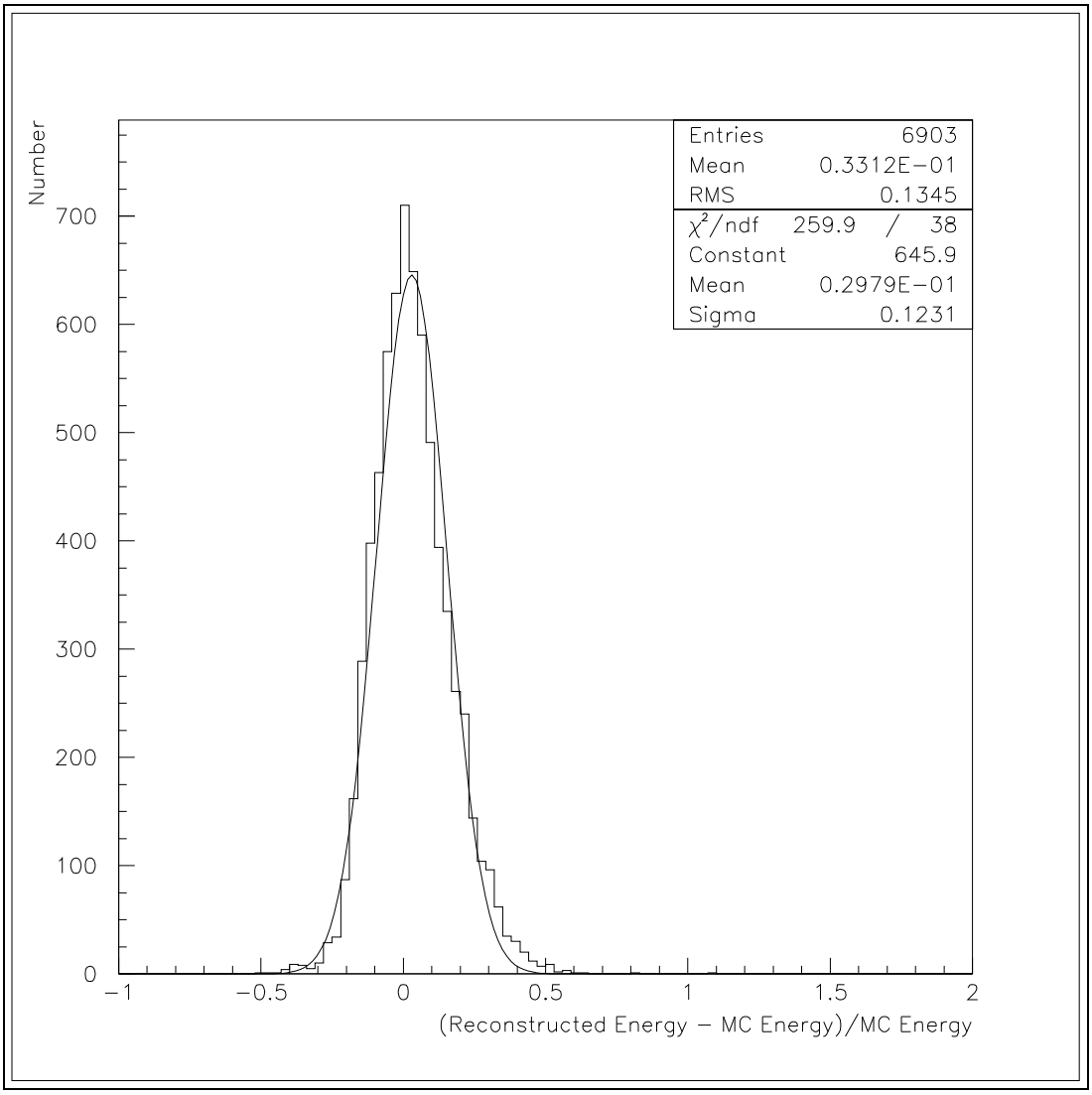

Figure 6.15. Final resolution in energy.

with energy, also indicating that composition is only slowly changing. The width of the data distribution in Figures 6.20 and 6.21 indicates that the composition is predominantly light.

Figure 6.20 shows that the data are consistent with a nearly purely protonic compositon, especially when compared to the QGSJet model. Assuming a simple two-component toy model where the primary flux is some mix of only protons and

Table 6.2. Elongation rate data. Uncertainties are variances of the means.

log(E/eV) Bin	Number of Events	Mean log(E/eV)	Mean X_{max} (gm/cm^2)
17.7-17.8	15	17.76 ± 0.01	689.4 ± 25.6
17.8-17.9	52	17.86 ± 0.01	689.0 ± 9.8
17.9-18.0	83	17.95 ± 0.01	707.2 ± 8.6
18.0-18.1	96	18.05 ± 0.01	718.9 ± 9.2
18.1-18.2	79	18.15 ± 0.01	709.2 ± 7.5
18.2-18.3	85	18.25 ± 0.01	712.6 ± 9.1
18.3-18.4	75	18.35 ± 0.01	731.0 ± 8.3
18.4-18.5	61	18.45 ± 0.01	744.5 ± 8.3
18.5-18.6	35	18.54 ± 0.01	747.0 ± 11.7
18.6-18.7	29	18.65 ± 0.01	734.2 ± 11.2
18.7-18.8	23	18.74 ± 0.01	752.2 ± 14.1
18.8-18.9	24	18.86 ± 0.01	751.6 ± 8.6
18.9-19.0	21	18.94 ± 0.01	757.0 ± 10.8
19.0-19.1	13	19.05 ± 0.01	758.9 ± 18.0
19.1-19.2	14	19.17 ± 0.01	764.4 ± 7.7
19.2-19.3	6	19.26 ± 0.01	781.6 ± 9.8
19.3-19.4	6	19.34 ± 0.01	792.9 ± 22.8
> 19.4	6	19.64 ± 0.06	798.4 ± 15.3

iron nuclei, Figure 6.22 shows how well the model fits the data as a function of per cent proton. The best fits are at 77% protons for QGSJet and 57% for SIBYLL. Figure 6.23 shows the toy models compared to the data.

6.3.1 Systematic Uncertainty in X_{max}

Figure 6.23 suggests that the composition of UHECR is predominantly light. However, systematic errors in the absolute value of X_{max} could artificially move the measured X_{max} values too deep in the atmosphere. The X_{max} values for events with energies above 10^{19} eV are of particular interest. Potential contributors to the systematic uncertainty in X_{max} are biases introduced by reconstruction,

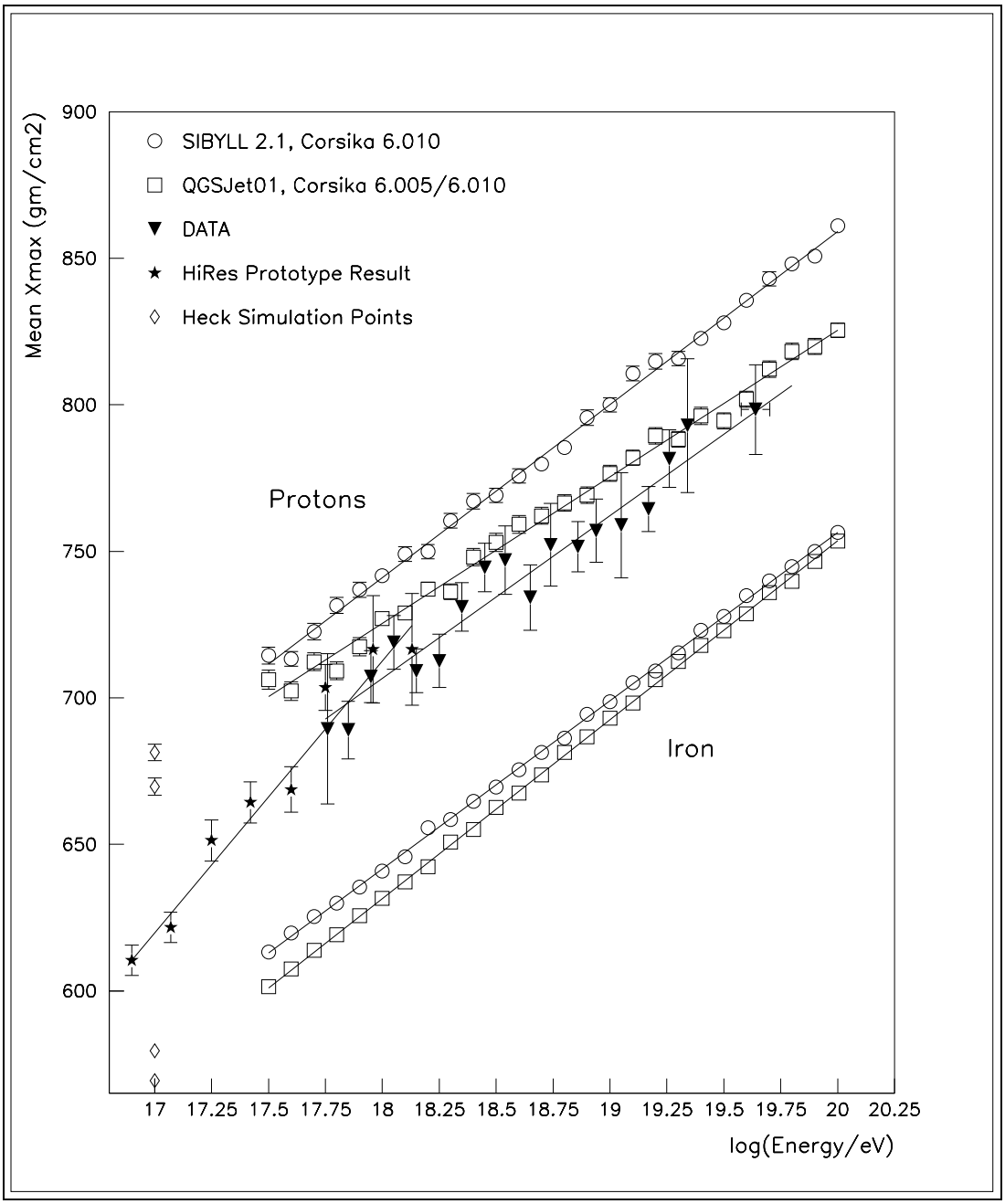

Figure 6.16. Elongation rate result. The predictions for QGSJet and SIBYLL protons and iron are shown for comparison (See Figure 4.6.) The stars show the HiRes Prototype result.

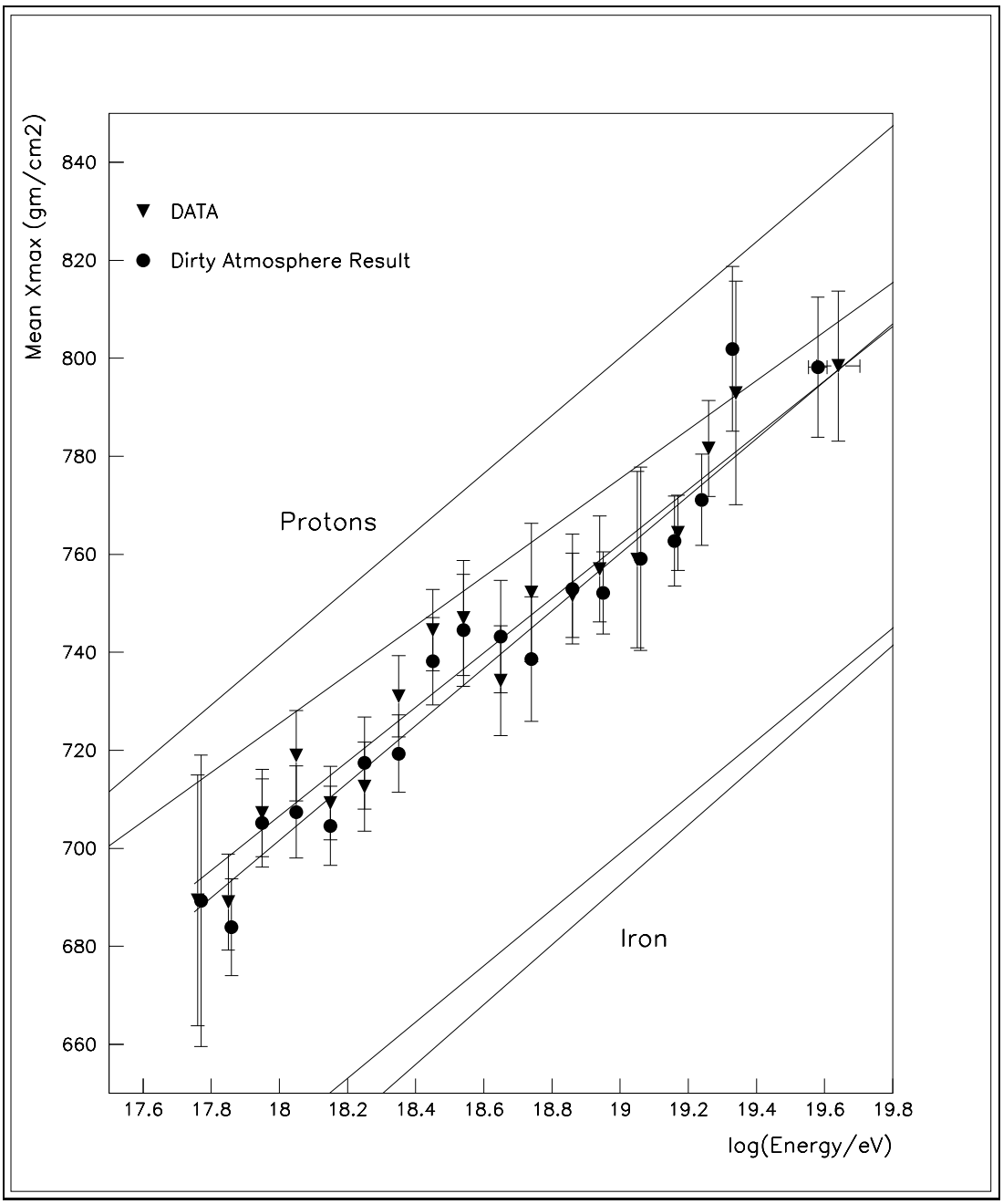

Figure 6.17. Uncertainty in elongation rate. The circles are obtained by reprocessing the data with a dirtier atmoshpere. The x- and y-axes are expanded relative to Figure 4.6 and Figure 6.16 to accentuated the small difference. The upper two and lower two lines are the model predictions from Figure 4.6.

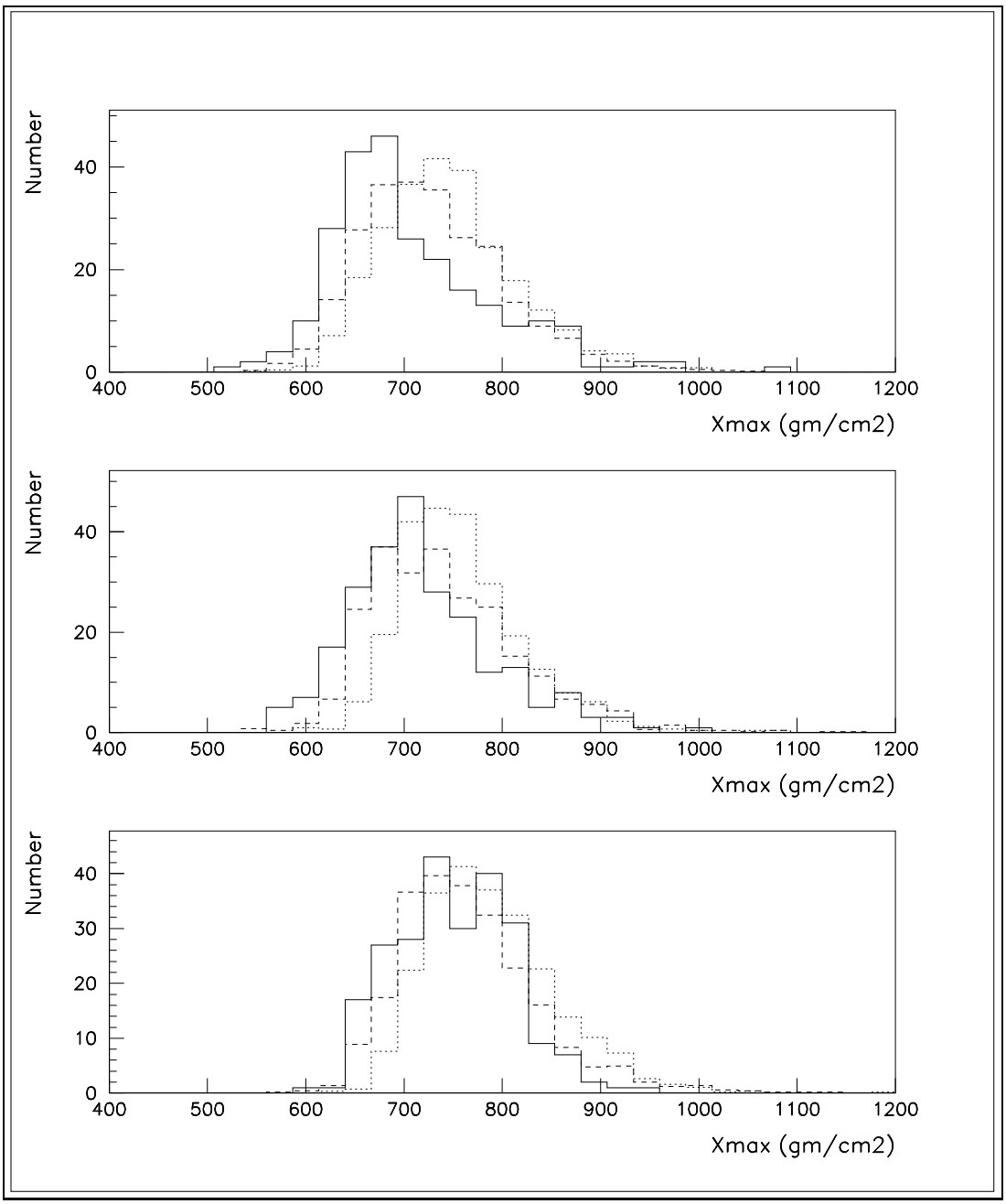

Figure 6.18. X_{max} distribution width result—protons. The top plot is for log(E) less than 18.1, the center plot for 18.1 to 18.4, and the bottom plot for greater than 18.4. In each plot, the solid line is the data, the dashed line is the QGSJet model, and the dotted line is the SIBYLL model. Compare Figures 4.7 and 6.19.

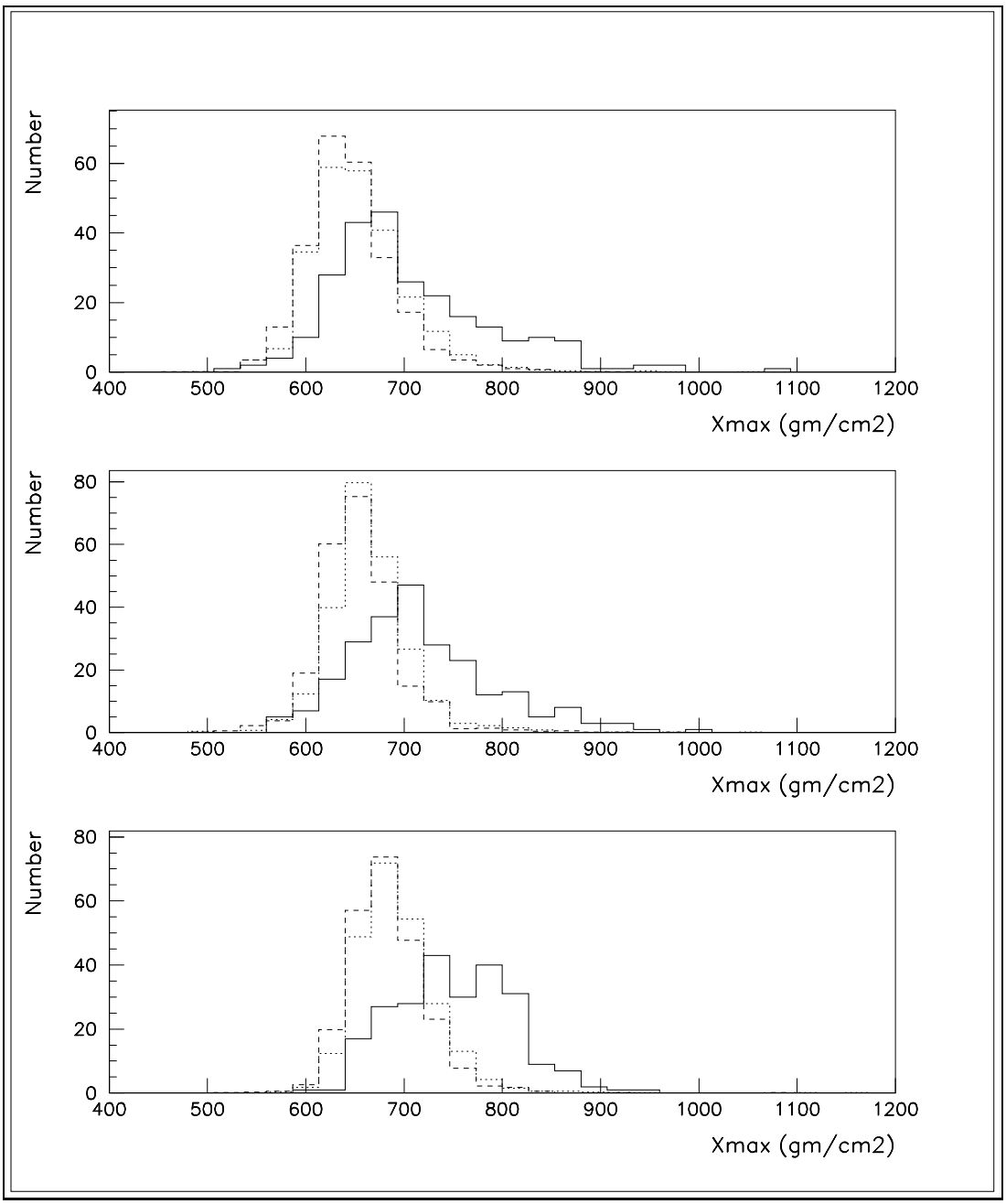

Figure 6.19. X_{max} distribution width result—iron. The top plot is for log(E) less than 18.1, the center plot for 18.1 to 18.4, and the bottom plot for greater than 18.4. In each plot, the solid line is the data, the dashed line is the QGSJet model, and the dotted line is the SIBYLL model. Compare Figures 4.7 and 6.18.

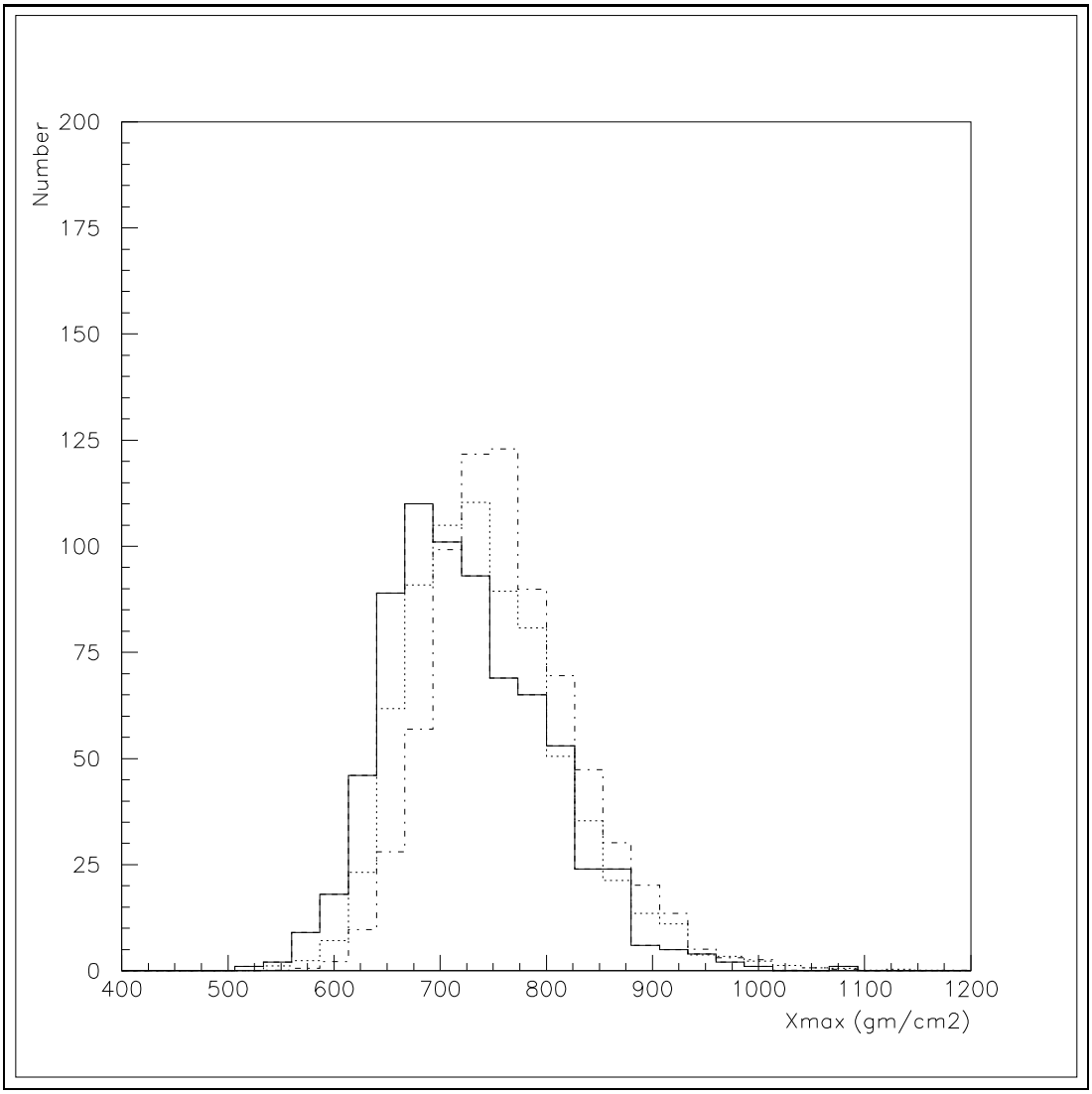

Figure 6.20. All-energy X_{max} distribution width result—protons. The solid line is the data, the dotted line is the QGSJet model, and the dot-dash line is the SIBYLL model. Compare Figures 4.8 and 6.21.

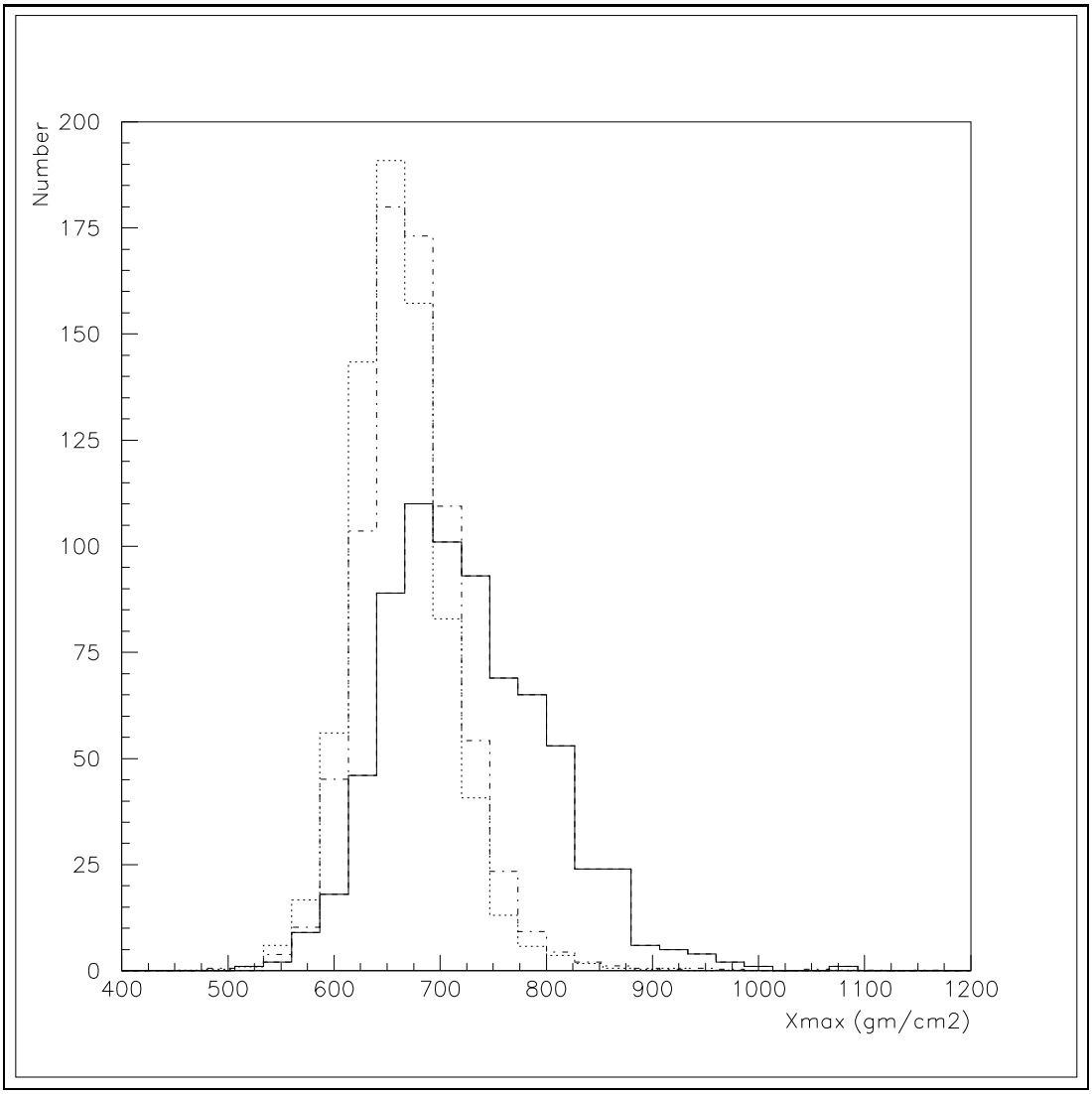

Figure 6.21. All-energy X_{max} distribution width result—iron. The solid line is the data, the dotted line is the QGSJet model, and the dot-dash line is the SIBYLL model. Compare Figures 4.8 and 6.20.

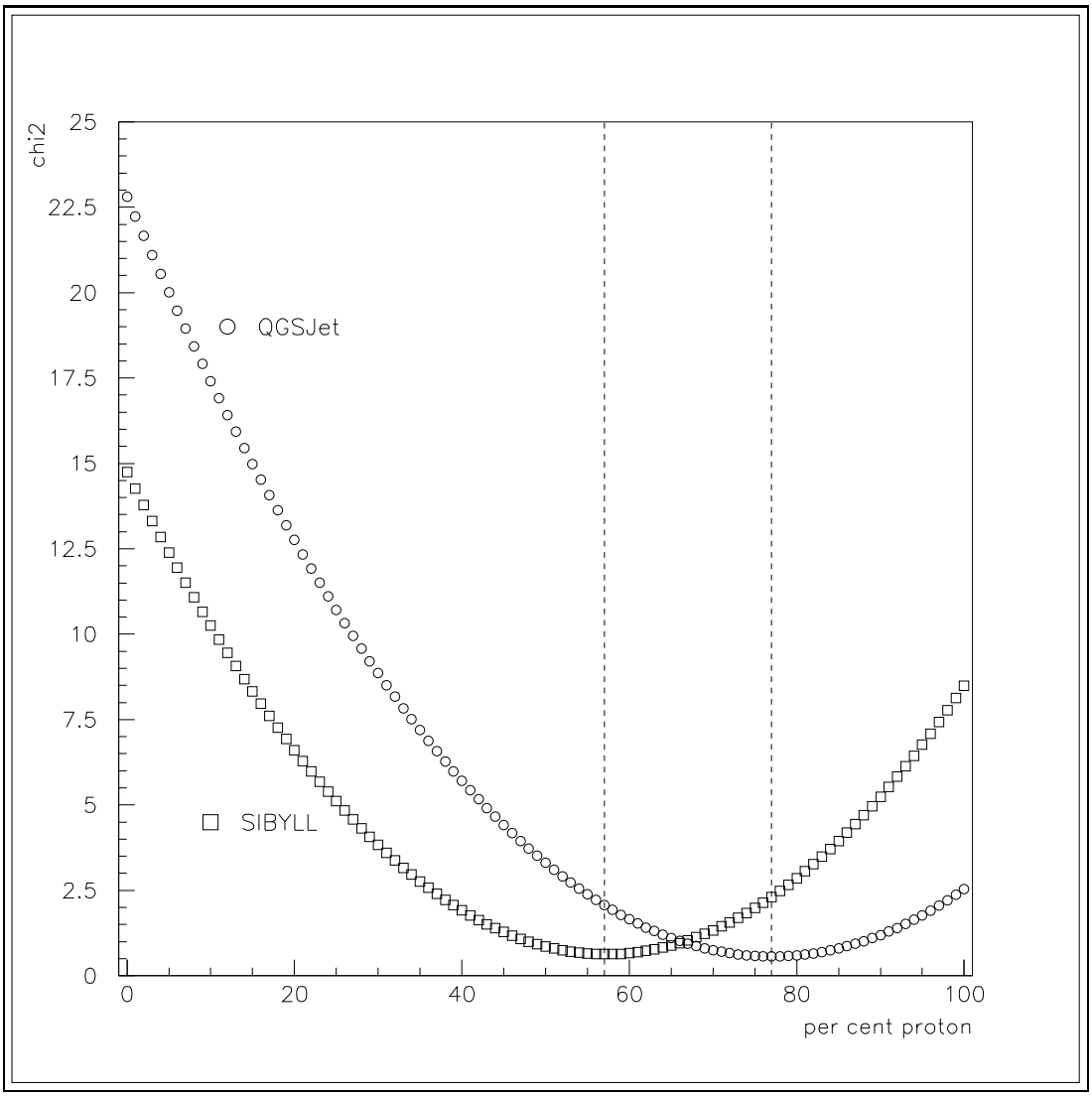

Figure 6.22. Simple two-component composition model fit results. The data points show the χ^2 for a data/model comparison at each per cent proton.

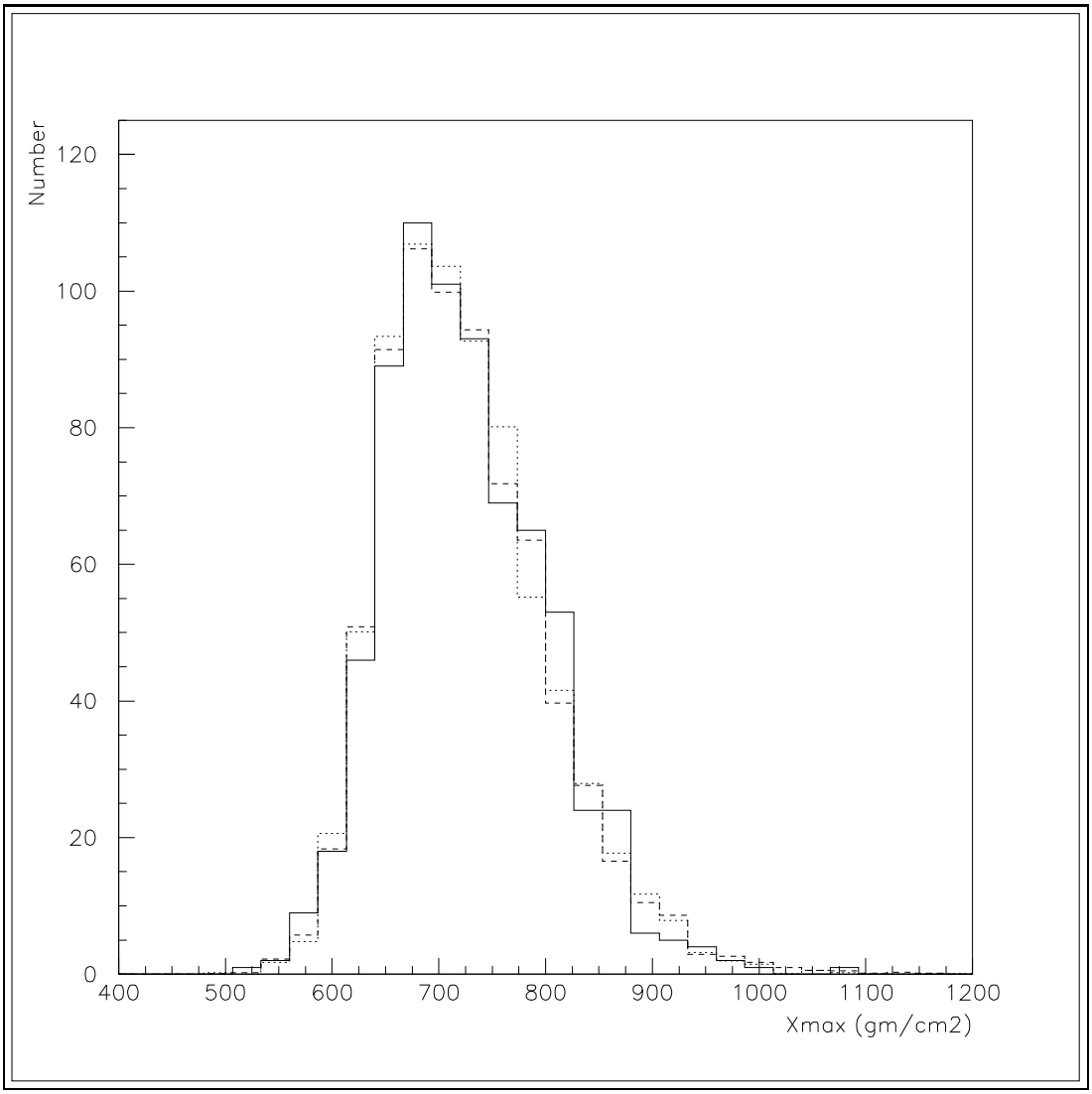

Figure 6.23. Simple two-component composition model. The solid line is the data, the dashed line is the QGSJet model with 77% proton, and the dotted line is SIBYLL with 57% proton.

errors in camera pointing directions, variations of the molecular component of the atmosphere, and incorrect treatments of the Čerenkov beam.

Figure 6.14 shows that the mean of the reconstructed X_{max} distribution is only about 5 gm/cm^2 different from the input value. For the events with energy greater than 10^{19} eV, the mean of the distribution is 3 gm/cm^2.

The camera pointing directions have been measured by observing stars [111, 113]. The largest deviation of true pointing direction from the direction used in reconstruction was 0.3°. The mean R_p for the highest energy events is 18.8 km. Assuming a homogenous atmosphere with the density predicted by the U.S. Standard Atmosphere of 1976 [81] for the altitude of HiRes, an event 20 km away with a zenith angle of 45°, a 0.3° pointing direction error translates into an error of 15 gm/cm^2.

The atmosphere may be different from the U.S. Standard Atmosphere assumed in the reconstruction. The HiRes team at the University of New Mexico studied the variations in the atmosphere as measured by radiosondes launched from the Salt Lake City airport. They showed that in the month of the year which varied most from the standard model, the actual pressure was different from the model by about 8% at most, which would lead to only a 10 gm/cm^2 difference in integrated atmospheric depth [82].

The atmosphere also effects the transmission of the fluorescence photons. Figure 6.17 shows that above 10^{19} eV, even a 50% change in optical depth does not greatly change the mean values of X_{max}. The effects on atmospheric transmission of less than 10% deviation in the molecular atmosphere are negligible.

As explained in Section 6.2.1, the data were reprocessed with a wider Čerenkov beam. The mean difference between the X_{max} obtained from reconstruction with the standard Čerenkov beam width and the X_{max} obtained by using a wider beam is less than 0.3 gm/cm^2 and is deemed negligible.

Table 6.3 summarizes the systematic uncertainties in X_{max} for energies above 10^{19} eV. Adding the individual uncertainties in quadrature gives an overall systematic uncertainty of less than 20 gm/cm^2.

Table 6.3. Systematic uncertainties in X_{max}

Uncertainty	gm/(cm^2)
Pointing Direction	15
Atmospheric Variations	10
Reconstruction Bias	5
Sum in Quadrature	18.7

6.4 Conclusions

The Elongation Rate result is consistent with a slowly changing composition above $10^{17.7}$ eV. The data are also in very good agreement with the HiRes Prototype data in the region where they overlap. The HiRes Prototype result showed a composition tending from heavy to light in the 10^{17} to 10^{18} eV range, but the HiRes data do not continue at the HiRes Prototype Elongation Rate. The good overlap coupled with the change in Elongation Rate are strong evidence for a transition to a predominantly light and slowly changing composition above 10^{18} eV. The widths of the X_{max} distributions in the UHECR regime strengthen this conclusion.

REFERENCES

[1] C. T. R. Wilson, Proc. Roy. Soc., **68**, 151 (1901).

[2] M. S. Longair, *High Energy Astrophysics, Volume 1, 2nd Ed.,* (Cambridge University Press, Cambridge, 1992).

[3] V. Hess, Phys. Z., **13**, 1084 (1912).

[4] W. Kolhorster, Deutsch. Phys. Gesell. Verh., **16**, 719 (1914).

[5] J. Clay, Proc. Roy. Acad. Of Amsterdam, **30**, 1115 (1927).

[6] P. Auger, R. Maze, and T. Grivet-Meyer, C. R. Acad. Sci. (Paris), **206**, 1721 (1938).

[7] P. Auger, *et al.*, Rev. Mod. Phys., **11**, 288 (1939).

[8] A. N. Bunner, *Cosmic Ray Detection by Atmospheric Fluorescence*, PhD Thesis, (Cornell University, Cornell, 1967).

[9] G. Tanahashi, in Workshop on Observing Giant Cosmic Ray Air Showers from $> 10^{20}$ Particle from Space, edited by J. F. Krizmanic, J. F. Ormes, and R. E. Streitmatter (American Institue of Physics, Woodbury, NY, 1998).

[10] J. Linsley, L. Scarsi, and B. Rossi, J. Phys. Soc. Japan, **17** (suppl. A-III), 91 (1962).

[11] H. E. Bergeson, *et al.*, Phys. Rev. Lett., **39**, 847, (1977).

[12] R. M. Baltrusaitis, *et al.*, Nucl. Inst. Meth., Sect. A **240**, 410 (1985).

[13] G. L. Cassiday, Ann. Rev. Nucl. Part. Sci., **35**, 321 (1985).

[14] D. J. Bird, *et al.*, Ap. J., **441**, 144 (1995).

[15] N. Sakaki, *et al.*, in Proceedings of the 27th International Cosmic Ray Conference (ICRC), Hamburg, 2001 (Copernicus Gesellshaft, Hamburg, 2001), Vol. **1**, p. 333.

[16] T. Abu-Zayyad, Nucl. Inst. Meth., Sect. A **450**, 253 (2000).

[17] The Auger Collaboration, *Pierre Auger Project Design Report*, 2nd ed. (1997). Available at http://astroparticle.uchicago.edu/cosmic_ray_spectrum_picture.htm

[18] A. M. Hillas, Ann. Rev. Astron. Astrophys., **22**, 425 (1984).

[19] E. Fermi, *Phys. Rev.*, **75**, 1169 (1949).

[20] M. S. Longair, *High Energy Astrophysics, Volume 2, 2nd Ed. with corrections*, (Cambridge University Press, Cambridge, 1997).

[21] R. J. Prothroe, in Topics in Cosmic Ray Astrophysics, edited by M. A. DuVenois (Nova Science Publishing, New York, 1999).

[22] L. O'C. Drury, Phys. Rep., **46**, 973 (1983).

[23] P. L. Biermann, J. Phys., **G23**, 1 (1997).

[24] P. Bhattacharjee, and G. Sigl, Phys. Rep., **327**, 109 (2000).

[25] D. Fargion, B. Mele, and A. Salis, Ap. J., **517**, 725 (1999).

[26] T. Weiler, Astropart. Phys., **11**, 303 (1999).

[27] A. A. Penzias, and R. W. Wilson, Ap. J., **142**, 419 (1965).

[28] K. Greisen, Phys. Rev. Lett., **16**, 748 (1966).

[29] G. T. Zatsepin, and V. A. Kuz'min, JETP Lett., **4**, 78 (1966).

[30] C. L. Bennet, *et al.*, Astro. J., **464**, L1 (1996).

[31] N. Hayashida, *et al.*, Phys. Rev. Lett., **77**, 1000 (1996).

[32] D. E. Groom, *et al.*, Eur. Phys. J., **15**, 1 (2000).

[33] A. M. Hillas, in Proceedings of the 16th ICRC, Kyoto, 1979 (University of Tokyo, Tokyo, 1979), Vol. **8**, p. 7.

[34] K. M. Simpson, *Studies of Cosmic Ray Composition Using a Hybrid Fluorescence Detector*, PhD Thesis, (University of Adelaide, Adelaide, 2001).

[35] A. M. Hillas, in Proceedings of the 17th ICRC, Paris, 1981 (Centre d'Studes Nuclaires de Saclay, Cedex, France, 1981), Vol. **13**, p. 69.

[36] T. H. Burnett, *et al.*, Phys. Rev. Lett., **51**, 1010 (1983).

[37] A. V. Apanasenko, *et al.*, in Proceedings of the 26th ICRC, Salt Lake City, 1999, (University of Utah, Salt Lake City, 1999), Vol. **3**, p. 163.

[38] A. V. Apanasenko, *et al.*, in Proceedings of the 26th ICRC (Ref. [37]), Vol. **3**, p. 167.

[39] D. J. Bird, *et al.*, Phys. Rev. Lett., **71**, 3401 (1993)

[40] T. Abu-Zayyad, *et al.*, Phys. Rev. Lett., **84**, 4276 (2000).

[41] T. Abu-Zayyad, *et al.*, Ap. J., **557**, 686 (2001).

[42] N. Hayashida, *et al.*, J. Phys., **G21**, 1101, (1995).

[43] B. R. Dawson, R. Meyhandan, and K. M. Simpson, Astropart. Phys., **9**, 331 (1998).

[44] N. Hayashida, *et al.*, in Proceedings of the 26th ICRC (Ref. [37]), Vol. **3**, p. 256.

[45] H. Y. Dai, *et al.*, astro-ph/9806096.

[46] N. Hayashida, *et al.*, in Proceedings of the 26th ICRC (Ref. [37]), Vol. **3**, p. 276.

[47] K. Greisen, Prog. Cosmic Ray Physics, **3**, 1 (1956).

[48] K. Greisen, Ann. Revs. Nuclear Science, **10**, 63 (1960).

[49] T. K. Gaisser, *Cosmic Rays and Particle Physics*, (Cambridge University Press, Cambridge, 1990).

[50] A. N. Cillis and S. J. Sciutto, Nucl. Phys. Proc. Suppl., **97**, 239 (2001).

[51] W. Heitler, *Quantum Theory of Radiation, 2nd Ed.*, (Oxford University Press, Oxford, 1944).

[52] J. Linsley, in Proceedings of the 15th ICRC, Plovdiv, 1977 (Bulgarian Academy of Sciences, Plovdiv, 1977), Vol. **8**, p. 207.

[53] J. Linsley, and A. A. Watson, Phys. Rev. Lett., **46**, 459 (1981).

[54] T. K. Gaisser, T. J. L. McComb, and K. E. Turver, in Proceedings of the 16th ICRC (Ref. [33]), Vol. **9**, p. 275.

[55] J. Linsley, J., in Proceedings of the 15th ICRC (Ref. [52]), Vol. **12**, p. 89.

[56] R. P. Feynman, Phys. Rev. Lett., **23**, 1415 (1969).

[57] P. Sokolsky, P. Sommers, and B. R. Dawson, Phys. Rept., **217 No. 5**, 225 (1992).

[58] K. Kamata, and J. Nishimura, Prog. Theor. Phys. Suppl., **6**, 93 (1958).

[59] K. Greisen, Prog. Elem. Part. Cos. Ray Phys., **3**, 1 (1956).

[60] A. M. Hillas, A.M., Acta Physica Hung, **29 Suppl. 3**, 355 (1970).

[61] A. M. Hillas, *et al.*, in Proceedings of the 12th ICRC, Hobart, 1971 (University of Tasmania, Hobart, Tasmania, 1971), Vol. **3**, p. 1001.

[62] T. C. Weekes, Phys. Rept., **160**, 1 (1988).

[63] F. Kakimoto, *et al.*, Nucl. Inst. Meth., Sect. A **372**, 527 (1996).

[64] C. L. Pryke, Astropart. Phys., **14**, 319 (2001).

[65] T. K. Gaisser and A. M. Hillas, in Proceedings of the 15th ICRC (Ref. [52]), Vol. **8**, p. 353.

[66] X. Zhang, *The Energy Spectrum of Cosmic Rays with Energy Above 1 EeV*, PhD Thesis, (Columbia University, New York, 2001).

[67] T. Abu-Zayyad, *The Energy Spectrum of Ultra High Energy Cosmic Rays*, PhD Thesis, (University of Utah, Salt Lake City, 2000).

[68] M. J. Kidd, *Properties of Extensive Air Showers Around* 10^{17} *eV*, PhD Thesis, (University of Illinois at Urbana-Champaign, Urbana-Champaign, 1997).

[69] C. R. Wilkinson, *The Application of High Precision Timing in the High Resolution Flys Eye Cosmic Ray Detector*, PhD Thesis, (University of Adelaide, Adelaide 1998).

[70] J. W. Elbert, in Proceedings of the Tokyo Workshop on Techniques for the Study of Extremely High Energy Cosmic Rays, Tokyo, 1993, edited by M. Nagano (Institute of Cosmic Ray Research, Tokyo, 1993), p. 232.

[71] J. Boyer, B. Knapp, E. Mannel, and M. Seman, in Proceedings of 26th ICRC (Ref. [37]), Vol. **5**, p. 441.

[72] D. Bird, in Proceedings of the Tokyo Workshop on Techniques for the Study of Extremely High Energy Cosmic Rays, (Ref. [70]), p. 269.

[73] K. Reil, private communication (2002).

[74] B. Jones, *et al.*, Calibrating the HiRes Flys Eye Detector, in Proceedings of the 26th ICRC (Ref. [37]), Vol. **5**, p. 429.

[75] B. Jones, *et al.*, in Proceedings of the 27th ICRC (Ref. [15]), Vol. **1**, p. 641.

[76] K. Reil, *The Energy Spectrum of Ultra High Energy Cosmic Rays Measured by the High Resolution Flys Eye Detectors*, PhD Thesis, (University of Utah, Salt Lake City, 2002).

[77] E. Mannel, private communication (2002).

[78] S. Moore, *Calibration at HiRes-1*, BS Honors Thesis, (University of Utah, Salt Lake City, in preparation).

[79] J. H. V. Girard, *et al.*, Nucl. Inst. Meth., Sect. A **460**, 278 (2000).

[80] G. Archbold, *et al.*, in Proceedings of the 27th ICRC (Ref. [15]), Vol. **1**, p. 623.

[81] *U.S. Standard Atmosphere, 1976* (NOAA, Washington, DC, 1976).

[82] G. Martin, *et al.*, in Proceedings of 26th ICRC (Ref. [37]), Vol. **5**, p. 361.

[83] L. R. Wiencke, *et al.*, Nucl. Inst. Meth., Sect. A **428**, 593 (1999).

[84] M. D. Roberts, *et al.*, in Proceedings of the 27th ICRC (Ref. [15]), Vol. **1**, p. 627.

[85] L. R. Wiencke, *et al.*, in Proceedings of the 27th ICRC (Ref. [15]), Vol. **1**, p. 631.

[86] J. A. J. Matthews, *et al.*, in Proceedings of the 26th ICRC (Ref. [37]), Vol. **5**, p. 412.

[87] M. D. Roberts, *et al.*, in Proceedings of the 27th ICRC (Ref. [15]), Vol. **1**, p. 645.

[88] L. R. Wiencke, *et al.*, in Proceedings of the 27th ICRC (Ref. [15]), Vol. **1**, p. 635.

[89] Y. Fedorova, private communication (2002).

[90] T. K. Gaisser, Nucl. Phys. B. (Proc. Suppl.), **52B**, 10 (1997).

[91] R. S. Fletcher, T. K. Gaisser, P. Lipari, and T. Stanev, Phys. Rev., **D50**, 5710 (1994).

[92] N. N. Kalmykov, S. S. Ostapchenko, and A. I. Pavlov, Nucl. Phys. B. (Proc. Suppl.), **52B**, 17 (1997).

[93] R. Engle, T. K. Gaisser, P. Lipari, and T. Stanev, in Proceedings of the 26th ICRC (Ref. [37]), Vol. **1**, p. 415.

[94] D. Heck, *et al.*, University of Kalsruhe Report No. FZKA-6019, 1998.

[95] K. Werner, Phys. Rep., **232**, 87 (1993).

[96] J. Ranft, Phys. Rev., **D51**, 64 (1995).

[97] H. J. Drescher, M. Hladik, S. S. Ostapchenko, and K. Werner, J. Phys. G: Nucl. Part. Phys., **25**, L91 (1999).

[98] H. J. Drescher, M. Hladik, S. S. Ostapchenko, T. Pierog, and K. Werner, Phys. Rep., **350**, 93 (2001).

[99] S. A. Bass, *et al.*, Prog. Part. Nucl. Phys., **41**, 225 (1998).

[100] M. Bleicher, *et al.*, J. Phys. G: Nucl. Part. Phys., **25**, 1859 (1999).

[101] H. Fesefeldt, Report **PITHA-85/02**, RWTH Aachen (1985).

[102] W. R. Nelson, H. Hirayama, and D. W. O. Rogers, Report **SLAC 265** (1985).

[103] D. Heck, *et al.*, in Proceedings of the 27th ICRC (Ref. [15]), Vol. **1**, p. 233.

[104] D. Heck, D., World Sci. (to be published), astro-ph/0103073.

[105] D. Heck, private communication (2002).

[106] M. Hillas, Nucl. Phys. B. (Proc. Suppl.), **52B**, 29 (1997).

[107] C. Song, C., *Study of Ultra High Energy Cosmic Rays with the High Resolution Flys Eye Prototype Detector*, PhD Thesis, (Columbia University, New York, 2001).

[108] T. Abu-Zayyad, *et al.*, Astropart. Phys., **16**, 1 (2001).

[109] A. Zech, private communication (2002).

[110] Z. Cao, private communication (2002).

[111] P. A. Sadowski, *et al.*, "Geometry and Optics Calibration for Air Fluorescence Detectors Using Starlight," Astropart. Phys. (to be published).

[112] D. R. Bergman, *et al.*, in Proceedings of the 27th ICRC (Ref. [15]), Vol. **1**, p. 639.

[113] D. R. Bergman, W. F. Hanlon, and G. B. Thomson, "HiRes Mirror Positions from GPS Surveying," HiRes Internal Note (1999).

[114] R. Abassi, *et al.*, "Measurement of the Spectrum of UHE Cosmic Rays by the FADC Detector of the HiRes Experiment," Astropart. Phys. (to be published).

[115] D. R. Bergman, private communication (2002).